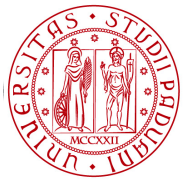

UNIVERSITÀ
DEGLI STUDI
DI PADOVA

Università degli Studi di Padova
CISAS “G. Colombo” Centro Interdipartimentale di Studi e Attività Spaziali

SCUOLA DI DOTTORATO DI RICERCA IN SCIENZE TECNOLOGIE E MISURE SPAZIALI
INDIRIZZO DI ASTRONAUTICA E SCIENZE DA SATELLITE
CICLO XXV

DEVELOPMENT OF ELECTROMAGNETIC CODES TO ANALYZE AND OPTIMIZE SATELLITE PROPULSION SYSTEMS AND COMMUNICATION ANTENNAS

❇

Sviluppo codici elettromagnetici per l’analisi e ottimizzazione di sistemi propulsivi e di telecomunicazione per apparati satellitari

Direttore della Scuola : Ch.mo Prof. GIAMPIERO NALETTO
Coordinatore d’indirizzo: Ch.mo Prof. GIAMPIERO NALETTO
Supervisore :Ch.mo Prof. DANIELE PAVARIN and Dr. MARCO MANENTE
Supervisore esterno:Ch.mo Prof. VITO LANCELLOTTI

Dottorando : DAVIDE MELAZZI

Università degli Studi di Padova

CISAS "G. Colombo" Centro Interdipartimentale di Studi e Attività Spaziali

Scuola di Dottorato di Ricerca in Scienze Tecnologie e Misure Spaziali
Indirizzo di Astronautica e Scienze da Satellite

Ciclo XXV

DEVELOPMENT OF ELECTROMAGNETIC CODES TO ANALYZE AND OPTIMIZE SATELLITE PROPULSION SYSTEMS AND COMMUNICATION ANTENNAS

*

Sviluppo di codici elettromagnetici per l'analisi e ottimizzazione di sistemi propulsivi e di telecomunicazione per apparati satellitari

Direttore della Scuola: Ch.mo Prof. Giampiero Naletto

Coordinatore di Indirizzo: Ch.mo Prof. Giampiero Naletto

Supervisori: Ch.mo Prof. Daniele Pavarin and Dr. Marco Manente

Supervisore esterno: Ch.mo Prof. Vito Lancellotti

Dottorando: Davide Melazzi
<davide.melazzi@studenti.unipd.it>
<davide.melazzi@gmail.com>

Padova, January 2013

To whom it may concern:
Topics discussed in Chap.2, Chap.3, Chap.4, and Chap.5 are to be considered innovative. The aforementioned chapters are related to numerical codes completely developed and validated during the PhD.

A chi vi possa essere interessato:
*Gli argomenti discussi nei Chap.*2*, Chap.*3*, Chap.*4*, e Chap.*5 *devono essere considerati innovativi. I suddetti capitoli sono pertinenti a codici numerici interamente sviluppati e validati nel corso del Dottorato di Ricerca.*

Contents

List of Figures

x

List of Tables

Abstract

Satellite communication systems have demonstrated their essential role providing timely services for disaster management in a variety of distress situations. Their effectiveness requires high mapping and pointing accuracy in terms of displacement capability, and high gain, high bandwidth, directional, and reconfigurable antennas in terms of communication capability. A Helicon plasma thruster, and an enhanced communication system meet the aforementioned requirements. The former is an electric plasma-based propulsion system that provides an high accuracy attitude control, while the latter could be either an optimized state-of-the-art antenna or an innovative concept based on plasma antennas.
In this research work, several computationally efficient codes have been developed to analyze, design and optimize the helicon plasma thruster, and the antenna for an enhanced communication system. The present work progresses starting from the definition of the requisites, and continues to describe the innovative numerical methods: the SPIREs finite-difference frequency-domain electromagnetic solver for magnetized plasma cylinders; the WAVEQM equilibrium condition solver for radiofrequency heated plasmas; the PARTYWAVE particle in cell code for cylindrical geometries, and the Moment Method for antenna design. Their numerical accuracy has been verified, and they have been validated against physical cases.

Gli apparati di comunicazione satellitare hanno dimostrato un ruolo essenziale nel fornire supporto tempestivo nella gestione di situazioni di emergenza. La loro efficacia richiede elevate precisioni di mappatura e di puntamento riferite al controllo d'assetto, mentre richiedono antenne con elevato guadagno, larghezza di banda e riconfigurabili in riferimento alle comunicazioni. Un propulsore elettrico al plasma di tipo Helicon è in grado di soddisfare i requisiti di mappatura e puntamento garantendo un controllo d'assetto di estrema precisione, mentre i requisiti pertinenti al sistema di comunicazione possono essere soddisfatti da una versione ottimizzata delle attuali antenne, o da una antenna innovativa basata sulle antenne al plasma.
In questo lavoro di ricerca sono stati sviluppati diversi codici, computazionalmente efficienti, pensati come strumenti di analisi, progettazione e ottimizzazione per propulsori al plasma Helicon e per sistemi di comunicazione avanzati. Il lavoro presentato in questo documento progredisce dalla definizione dei requisiti fino ad una descrizione dettagliata dei singoli codici: SPIREs un solutore elettromagnetico nel dominio della frequenza per plasmi magnetizzati, WAVEQM un solutore delle condizioni di equilibrio per sorgenti di plasmi in radiofrequenza, il codice particellare PARTYWAVE, e un codice per la progettazione di antenne basato sul Metodo dei Momenti. L'accuratezza numerica dei singoli codici è stata verificata, ed essi sono stati validati con test significativi da un punto di vista fisico.

Introduction

Space systems from their advantage position have demonstrated their capability of providing vital informations and services for disaster management; the huge amount of capabilities provided by communication satellites can be available for timely dissemination of early warning, and real-time coordination of relief operations. Satellite communication capabilities are vital for effective communication, especially in data collection, distress alerting, position location, and co-ordinating relief operations on the ground. In addition, Search and Rescue satellites provide capabilities like position determination facilities which could be useful in a variety of land, sea, and air distress situations. Thereby, in case of emergencies or natural disasters, broadband communication satellites can play a fundamental role, and their combination with navigation satellites can support new services for emergency and rescue teams.
Nevertheless, addressing these monitoring requirements will lead to the development of various advanced satellite communication technologies that will bring a positive feedback on the capability and flexibility of communications, broadcasting and positioning services from the space to multiple users. In this scenario, broadband communication equipment to be applied in case of natural disaster onboard satellites may require:

- high robustness to space environment (i.e plasma environment generated by solar wind or plasma plume of electric thruster)
- high displacement capability (in terms of orbit configuration)
- capability of operating also at low orbit in order to increase the observed areas
- high mapping accuracy
- high pointing accuracy
- high gain, high bandwidth and highly-directional antennas
- high reliability, flexibility and survivability

The aforementioned system drivers are satisfied by:

1. High accuracy attitude control system
   $\Rightarrow$ *The attitude control system can employ an electric propulsion system to provide high pointing and mapping accuracy; a helicon plasma thruster is advised because of its accurate low-thrust high-specific impulse operations capability, and because it*

can work both in pulsed and in continuous mode. This choice allows for an accurate, continuous thrust control against other chemical thrusters; additionally, this electric propulsion system is very efficient in minimizing the satellite mass budget. Regardless other electric propulsion systems, this kind of thruster will provide globally neutral gas at the exhaust, resulting in a weaker electromagnetic perturbation of the environment around the spacecraft.

2. Enhanced communication system
   ⇒ *In order to provide reliable and efficient data transmission, there are two options for the communication system: (i) the optimization of a state-of-the-art antenna, (ii) the development of a brand new antenna concept. In the former, an already existing antenna for space communication can be considered and optimized in order to guarantee the properties mentioned above (e.g. high pointing accuracy, high gain, high bandwith, etc...) and to cope with the space environment disturbances. In the latter, the plasma antenna concept can be considered as the innovative mean to achieve a reconfigurable, reliable and survivable antenna candidate.*

In order to analyze, design and optimize the helicon thruster (that will provide a high accuracy attitude control system) and the antenna for an enhanced communication system, we need numerical tools that must address the following requirements: (i) the electromagnetic wave propagation, (ii) the antenna-plasma coupling mechanism, (iii) the power deposition phenomena inside the plasma, and (iv) the plasma response inside the source of the helicon thruster, (v) the scattering of electromagnetic fields in the presence of a ionized medium.
In this research work we focused on the development and validation of innovative and computationally efficient numerical tools fulfilling the above requirements, and whose description is the main topic of the present document.
For sake of clarity, it is worth recalling that the application of the newly developed computational tools to the design and the efficiency of a helicon space thruster and to the plasma antennas for communication purposes is out of the scope of this work.
In the next chapter, we clarify why the aforementioned requirements are necessary, while in the other chapters we deal with the governing equations, the numerical implementation, and the validation test cases concerning each code developed in this research work.

Chapter 1

Requisites Definition

As far as a space satellite is concerned, the propulsion (for attitude control) and the communication subsystems belong to separate frameworks. However, they share the same requisites in order to address the aforementioned system drivers, meaning that we can develop codes that can work for the helicon plasma thruster as well as for the communication antenna.
In the next sections we will consider the helicon plasma thruster and the communication antenna problems separately, highlighting the main features and still open issues for each one. At the end it will be clear that, whether we are interested in the propulsive figures of merit of the plasma thruster or the efficiency in the signal propagation for communication applications, it always reduces to treating propagation and absorption of electromagnetic waves in a ionized and magnetized medium such as a plasma.

1.1 Helicon Space Plasma Thruster

Several new space systems utilizing plasma propulsion concepts have been proposed thanks to the much higher specific impulse, a huge reduction in the propellant mass of a space mission, and high thrust efficiency achievable. In a plasma propulsion system, the specific impulse is extrinsic depending on the electromagnetic energy deposited into plasma, which is in turn related to the thrust efficiency. In order to study, design and optimize a plasma propulsion system, it is convenient to distinguish two main stages in a plasma thruster, where different physical processes take place: the production stage in the plasma source, and the acceleration stage at the exhaust section of the thruster. In the production stage plasma propulsion uses electric power to ionize the propellant and then impart kinetic energy to the resulting plasma via either energetic electron injection, biased electrodes or electromagnetic irradiation, while in the acceleration stage the plasma is exhausted by means of either electrothermal, electrostatic or electromagnetic processes [1].
Present plasma propulsion devices, such as the Ion Engine (IE) and the Hall Effect Thruster (HET), have proven high efficiencies but exhibited some critical issues such as: lifetimes limited by the erosion of the extracting grids and the ceramic walls, the need of the external cathode for charge compensation, and the low power density due to the uncompensated space charge and to limitations of the magnetic field topology in IEs and in HETs, respec-

tively [2]. Recent advances in plasma-based propulsion systems have led to the development of electromagnetic Radio-Frequency (RF) plasma generation and acceleration systems, called Helicon Plasma Thruster (HPT), derived from high density industrial plasma sources (i.e. helicon sources). The HPT is basically a modified helicon source: it is simple in design, and it is capable of depositing efficiently electromagnetic power thus creating a very dense plasma but without suffering all the drawbacks related to IEs or HETs. As said above, this high efficiency plasma generation can led to high and variable specific impulse and good thrust efficiency, allowing the HPT to compete with other plasma thrusters.
Three main projects are currently using helicon sources for propulsion. The high-power Variable Specific Impulse Magnetoplasma Rocket (VASIMR) [3], [4] couples a first-stage helicon source with a second-stage Ion Cyclotron Resonance Heating (ICRH) for ion heating. The Australian thruster at ANU aims at developing a medium-power helicon thruster. The European project HPH.COM (Helicon Plasma Hydrazine COmbined Micro) aims at developing a space plasma thruster based on helicon plasma sources working in the radiofrequency regime at low power (<100W of RF power), coupled with a secondary propellant stage for higher thrust levels. The low-power HPH.COM plasma thruster employing high efficiency RF sources is currently under development [5], [6], [7] for application to mini satellite for attitude and position control. The target applications are small satellites operating with available propulsion power in the range of 50W, the expected thruster propulsion performance is below <1.5mN of thrust and a specific impulse above >1200s.
The HPH.COM thruster can be considered an electrical propulsion system where the plasma source is a helicon plasma source. As shown in Fig. 1.1, the main components of HPH.COM helicon thruster are: a gas feeding system, an RF antenna, and magnetic coils. The feeding system injects a neutral gas into a cylindrical vessel, wrapped by a radiofrequency antenna system working in the MHz range, ionizing the neutral gas and heating the plasma. The magnetic coils provide the quasi-axial magnetic field that allows for the propagation of helicon waves and the confinement of plasma inside the cylindrical source. Unlike a helicon plasma source for industrial application, the magnetic field lines at the exhaust section have to become divergent providing a "magnetic" nozzle effect on the magnetized plasma; the name "magnetic" nozzle is due to the resemblances between the axial expansion of the plasma in it and of a hot gas in a solid nozzle. The structure of the thruster does not need any electrode, neutralizer, or acceleration grid thus allowing for low development costs and high reliability.

1.1.1 The Helicon plasma source - A review

Helicon sources are able to sustain a steady-state magnetized plasma at low pressure, through the propagation and absorption of radiofrequency (RF) electromagnetic waves in the range $\omega_{ci} \ll \omega_{lh} \ll \omega \ll \omega_{ce}$, where ω_{ci} and ω_{ce} are the ion and electron cyclotron angular frequencies, and ω_{lh} is the lower-hybrid frequency. Throughout the last decades, helicon plasma sources have been recognized to be much more efficient rather than capacitive and inductive sources in generating dense plasmas [8],[9],[10],[11]. Plasma densities up to 10^{19} m^{-3} can be reached, using moderate magnetostatic fields below <0.1 T, and with RF antennas of simple geometry, like single-loop, double-loops, Nagoya type III, etc. Helicons are currently of considerable interest for a large variety of applications including

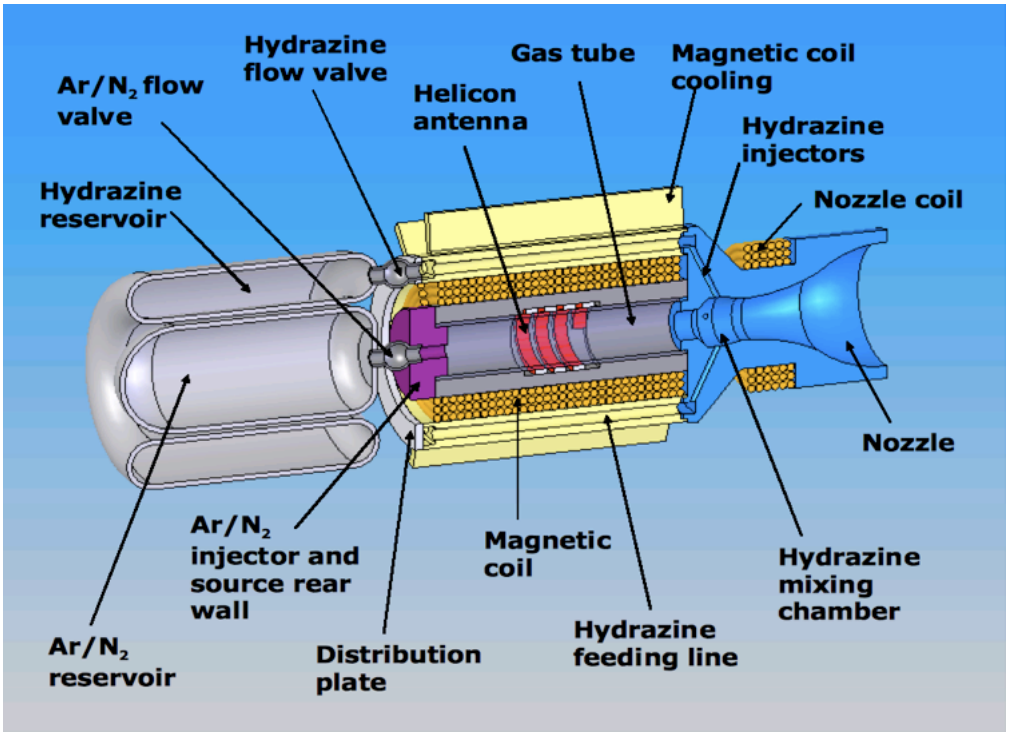

Figure 1.1: Overview of the helicon plasma thruster in HPH.COM project.

semiconductor manufacturing, spacecraft propulsion, material surface modification, material processing, basic and applied laboratory research. Helicon plasma sources have also been considered as a viable source of high-energy ions in mini-magnetospheric plasma propulsion devices, to inflate a magnetic field around a spacecraft resulting in acceleration due to solar wind pressure [12]. Moreover, thanks to their high efficiency and to the production of high density plasma, they have been considered for plasma propulsion on spacecrafts.
The physics of wave propagation and power deposition in a helicon discharge has been previously studied by many theoretical and experimental works, but many questions regarding their fundamental physics are still open. The first calculations were done by Klozenberg *et al.* [13] and by Boswell [14] for a uniform helicon source. They derived the dispersion relation of a single-mode whistler-like helicon branch in a cylindrical plasma of uniform density bounded by vacuum. Chen [11] studied the wave pattern in more detail and provided some evidence that Landau damping combined with particle trapping might be a decisive factor in accelerating a considerable portion of the electrons up to and above ionization energies of the neutral gas. Fischer *et al.* [15] numerically produced a quantitative description of the helicon wave coupling problem and examined, by means of an eigenmodes representation of the electromagnetic fields coupled to a plasma column inside an ideally conducting cavity, the role of the electron Landau damping as a potential candidate for the effective wave absorption in helicon wave devices. Kamenski and Borg [16] developed a radial plasma kinetic code, employing a finite element discretization of RF fields in terms of electromagnetic potentials and including not only the parallel electron dynamics but

also the collisional dissipation, providing a better understanding of the antenna-plasma coupling for different antenna configurations. Furthermore, in order to get more insight in the helicon wave properties in a nonuniform plasma, several authors [17],[18] focused on how the wave dispersion can be affected by the plasma inhomogeneities, studying the helicon wave dispersion isolated from the problem of wave coupling and excitation. Kramer [19] investigated the role of the density gradient for the helicon wave propagation and for the damping of different helicon modes, providing evidence that the density gradient effect is decisive for the formation of helicon discharges. To investigate density profile effects of helicon plasmas, Mouzouris and Scharer [20] developed the ANTENA2 simulation code, an improved version of the original ANTENA code [21] where electromagnetic fields are expanded into waveguide modes that are Transverse Electric (TE) and Transverse Magnetic (TM), founding out that electron heating profiles are strongly dependent on the plasma profiles; Cho and Kwak [22] extended the previous results computing power absorption profiles using a numerical integration approach for radially nonuniform helicon plasmas with finite axial lengths. Later on, after several attempts to observe kinetic effects related to Landau damping Chen pointed out that all experimental results could be explained by collisional theory alone [23]. Chen and Arnush assembled these various results and extended them in order to achieve a single and coherent formulation of the helicon theory [24],[25],[26]. Two coupled modes, the helicon (H) and the Trivelpiece-Gould (TG) mode, are involved in the helicon regime. The dynamics of these modes and how they couple with the cylinder geometry affect the energy absorption. In the uniform density case the H-waves penetrate to the center of the plasma and they are very weakly damped by collisions throughout the body of the plasma, being an unlikely channel for RF absorption. Near the boundary of the plasma cylinder H-waves are mode converted into short wavelengths TG waves, and they are rapidly damped with power deposition. For a nonuniform plasma with a more realistic density profile, coupling between the H and TG waves occurs throughout the plasma volume giving a more uniform heating. The theory was confirmed also by other groups [27],[28], leading to understand the main role of the TG mode in enhancing the power deposition near the walls [29], also considering the macroscopic transport of the involved plasma species. Afterwards it has been shown theoretically [30] and later confirmed numerically [31] that the radial density gradient pertinent to helicon plasma sources has a profound effect on the structure of electromagnetic waves that drive the discharge. The density gradient creates a "wave-guide" for Radially Localized Helicon (RLH) modes. These modes do not exist in a uniform plasma, because they are analogous to surface waves, with the density gradient playing the role of a surface. These modes have a dispersion relation that scales differently compared to the conventional helicon wave, explaining the unusually low operational frequency of helicon sources for the typical source parameters. It has been clearly demonstrated [31] that the RLH waves play a major role in power deposition in helicon plasma sources, and it has also been shown [32] that the RLH wave damping rate is anomalously enhanced. Moreover, RLH waves and conventional helicon waves can efficiently couple by axial non-uniformities, as demonstrated in [33], and by an earlier experimental work [34] showing a clear evidence of an RLH eigenmode excitation in a helicon discharge.

1.1.2 Requisites definition for the Helicon plasma source

In this work we refer to the low power HPH.COM thruster because it has been specifically conceived for attitude and position control applications; however, there are no limitations to make codes running in high power regimes.
In particular, the HPT can be divided in two coupled stages: the plasma source (also known as *production stage*) and the divergent magnetic nozzle (also known as *acceleration stage*). In these two stages different physical processes take place: in the former we have the wave-plasma interaction and the internal plasma dynamics, whereas in the latter we have the supersonic plasma acceleration and the plasma detachment from the magnetic nozzle. The codes presented here have been specifically conceived to study, analyze and optimize the plasma source, and considering that the propulsive performance are related to the electromagnetic energy deposited into plasma (i.e. plasma electrical resistance), these codes are supposed to provide the following informations:

- electromagnetic wave propagation and power deposition phenomena in a magnetized plasma
- antenna - plasma coupling mechanism
- identification of geometry and plasma discharge parameters that maximize plasma resistance
- detailed plasma response (considering plasma as a dielectric, as a charged-species fluid, as an ensemble of charged particles interacting in an electromagnetic field, forced by an external antenna)

1.2 Enhanced communication system

As far as the communication system is concerned, two options can be considered: (i) the optimization of a state-of-the-art antenna, (ii) the development of a brand new antenna concept. In the first case, an already existing antenna for space communication can be optimized to guarantee the system drivers mentioned above (e.g. high pointing accuracy, high gain, high bandwith) and to cope with the space environment disturbances. In the second case, we consider the innovative plasma antenna as the mean to achieve a reconfigurable, reliable and survivable candidate.

1.2.1 The Plasma Antenna - A review

Physically, an antenna is an arrangement of one or more conductors; in transmission, an alternating current is created in the conductor elements by applying a voltage at the antenna terminals, thus causing the electromagnetic fields to radiate. In reception, an electromagnetic field from another source induces an alternating current in the conductor elements and a corresponding voltage at the antenna terminals.
A plasma antenna is a RF antenna using plasma elements instead of metal conductors [35]; such antennas are constructed from insulating tubes filled with low pressure gases. Plasma is created by applying RF power to the discharge tubes; when it is on, plasma is an electrical

conductor, and it can provide the conducting medium for electromagnetic radiation. The fact that the emitting element is formed just over the interval needed for the emission of an eletromagnetic pulse is an important advantage of plasma antennas; in the passive state such a device does not exhibit electric conductivity. It is worth recalling that plasma radiating elements provide a number of potential *advantages* over conventional metal elements for antenna design as they permit electrical, rather than mechanical control of their characteristics, including the following:

1. plasma antennas are free from mechanical parts, making them ideally suited for a wide range of communications and sensing applications
2. plasma antennas revert to a dielectric tube when they are de-energized making them difficult to be detected by radar
3. even when it is energized, plasma is transparent to the transmission above the plasma frequency
4. plasma antennas can be energized only for a very short time as communication takes place thus minimizing signal degradation
5. plasma antennas can focus high-frequency radio waves that would dissipate quickly if beamed by conventional arrays
6. plasma antennas can be rapidly reconfigured in terms of radiation pattern and transmission frequency thanks to an accurate tuning of plasma characteristics
7. the effective length of the plasma antenna can be changed by controlling the applied RF power, allowing rapid reconfiguration of the resonant length of the antenna for different transmitting frequencies
8. plasma antenna arrays can be reconfigured so unused antennas will not couple unwanted power signals into nearby receivers (if any), thus allowing their use in situations that require different antennas for several communication systems to be in close proximity, and simplifying the layout of on-board communication systems

Unfortunately, they come with *limitations* like:

1. plasma antennas are expensive
2. plasma antennas are hard to manufacture

The proposal to use plasma as the conductor in a radio frequency antenna is not new [36]-[37]. Recently, there has been a resurgence of interest in plasma antennas stemming from the possibility of producing structures of low radar cross section [38]; furthermore, the aforementioned advantages give additional motivations for the investigation of plasma antennas. In early experiments, the plasma has either been produced by means of electrodes at opposite ends of the plasma columns or ionization by laser beam. Moisan *et al.* have proposed that a plasma column could be driven directly from one end by excitation of a plasma surface wave [36].

Specifically, in the last case the antenna consisted of a dielectric tube filled with neutral gas (tipically Argon), and a copper collar providing an intense electric field sufficient to ionize the gas, and to drive the resulting surface wave along the interface between the plasma and the dielectric tube, igniting the plasma along the column; a second coupling collar is mounted, and it is used to apply the communication signal.
The plasma is actually powered by two different frequencies simultaneously: a drive frequency and a signal frequency so that it might be used for both transmission (both frequencies switched on) or reception (only the drive frequency switched on). Recent experiments have demonstrated that such antennas can be efficient, and generate low noise so as to be useful for high-frequency (HF) ($3 - 30$ MHz) and very high-frequency (VHF) ($30 - 300$ MHz) communications [39], [40].
Radiation patterns of plasma antennas have been calculated assuming that the plasma is uniformly distributed inside the discharge tube [40]. Starting from the global model developed for a plasma source sustained by a surface wave [41], [42], it has been demonstrated: (i) the length of the plasma column increases as the square root of the applied RF power, (ii) the conductivity profile along the column is essentially linear, and (iii) the importance of the method used for coupling the transmission signal into the antenna [43].
From these results it should be possible to preliminarily design an antenna with an electrically controllable length, allowing rapid reconfiguration for different transmission frequencies. In order to reproduce accurately the plasma response a self consistent kinetic model of the plasma antenna has been developed [44], describing how plasma parameters affect antenna efficiency and radiation pattern.

1.2.2 Requisites definition for the communication antenna

The codes presented here have been specifically conceived to study, analyze and optimize antennas for communication in space. These codes have to address the following requisites:

1. detailed current distribution over an arbitrarely-shaped antenna surface radiating in free space

2. detailed current distribution over an arbitrarely-shaped antenna surface radiating in the nearby of a ionized medium

3. identification of the best antenna configuration in terms of radiation pattern

Chapter 2

SPIREs: A Finite-Difference Frequency-Domain electromagnetic solver for inhomogeneous magnetized plasma cylinders

2.1 Introduction

We present SPIREs (plaSma Padova Inhomogeneous Radial Electromagnetic solver), a Finite-Difference Frequency-Domain (FDFD) electromagnetic solver in one dimension for the rapid calculation of the electromagnetic fields and the deposited power of a helicon plasma source and a large variety of cylindrical plasma problems. The two Maxwell wave equations have been discretized using a staggered Yee mesh along the radial direction of the cylinder, and Fourier transformed along the other two dimensions and in time. Fields are forced by an antenna placed at a given distance from the plasma. The plasma can be inhomogeneous, finite-temperature, collisional, magnetized and multi-species. Finite-temperature Maxwellian effects, comprising Landau and cyclotron damping, have been included by means of the plasma Z dispersion function. Finite Larmor radius effects have been neglected. Radial variations of the plasma parameters are taken into account, thus extending the range of applications to a large variety of inhomogenous plasma systems. The method proved to be fast and reliable, with accuracy depending on the spatial grid size. Two physical examples are reported for the benchmarking: fields in a forced vacuum waveguide with the antenna inside, and forced plasma oscillations in the helicon radiofrequency (RF) range. In the last section, electrical impedance results show what parameters are most effective in depositing power inside a magnetized plasma cylinder.

2.2 Governing equations

A plasma cylinder of radius r_a is surrounded by an antenna placed at radius r_b, and enclosed inside a conducting tube of radius r_c. Fig. 2.1 shows an axial section of the geometry. The cylindrical symmetry of the system suggests the use of cylindrical coordinates (r, θ, z). A

magnetostatic field $\boldsymbol{B_0}$ is directed along the z axis, $\boldsymbol{B_0} = B_0\hat{\boldsymbol{z}}$, perpendicular to the (r, θ) plane.

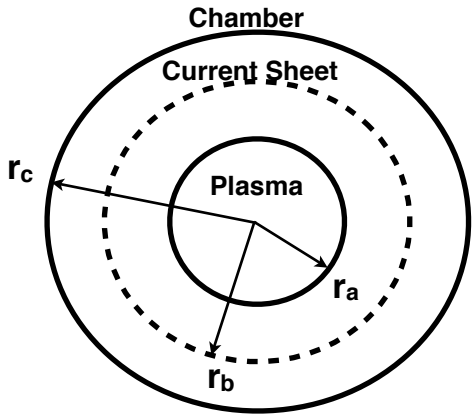

Figure 2.1: Geometry in the (r, θ)-plane of the plasma system treated by SPIREs, where r_a radius of the plasma column, r_b radius of the antenna current sheet, r_c radius of the conductive chamber. The z axis points outward, perpendicular to the (r, θ) plane.

Quantities along θ and z directions are Fourier transformed in the corresponding spectral modes, m (azimuthal) and k_z (axial) respectively. Only integer azimuthal modes $m = 0, \pm 1, \pm 2, ...$ are propagative. Wave quantities vary as $\exp[i\,(m\theta + k_z z - \omega t)]$, where m is the azimuthal mode, k_z is the parallel wave number and ω is the angular frequency of the wave (Appendix A). Physical quantities can then be restored in spatial coordinates by anti-Fourier transforming:

$$F\,(r, \theta, z) = \frac{1}{2\pi} \int_{-\infty}^{+\infty} dk_z \sum_{m=-\infty}^{+\infty} F\,(r, m, k_z)\, e^{i(m\theta + k_z z)} \tag{2.1}$$

The wave propagation of electromagnetic fields inside the system is regulated by the two wave Maxwell equations [45], the Faraday and Ampere-Maxwell laws, plus the constitutive relations of the materials,

$$\nabla \times \boldsymbol{E} = i\omega t \boldsymbol{B} \tag{2.2}$$

$$\nabla \times \boldsymbol{H} = -i\omega t \boldsymbol{D} + \boldsymbol{J} \tag{2.3}$$

$$\boldsymbol{D} = \boldsymbol{\epsilon} \boldsymbol{E} \tag{2.4}$$

$$\boldsymbol{B} = \boldsymbol{\mu} \boldsymbol{H} \tag{2.5}$$

The fields $\boldsymbol{E}$ and $\boldsymbol{B}$ are related to the electric displacement $\boldsymbol{D}$ and the magnetic field $\boldsymbol{H}$ through the low frequency constitutive relations Eqs. 2.4 and 2.5, by means of the dielectric tensor $\boldsymbol{\epsilon}$ and the magnetic permeability tensor $\boldsymbol{\mu}$. Fields are forced by the oscillating volume current source $\boldsymbol{J}$. As far as a perfectly conductive antenna in the thin wire approximation is concerned, the forcing current term can be treated with negligible extension along the radial dimension,

$$\boldsymbol{J_\theta}\,(\boldsymbol{r}) = I_0 \delta\,(r - r_b)\,\hat{\boldsymbol{\theta}} \tag{2.6}$$

where I_0 is a surface current density, in A/m, and $\hat{\boldsymbol{\theta}}$ is the unit vector in the azimuthal direction. This current distribution at $r = r_b$ is represented by an infinite set of current sheets [21], each one supporting an infinitesimally thin surface current and being harmonic functions with respect to time and space as $\exp[i\,(m\theta + k_z z - \omega t)]$. Furthermore, assuming the antenna current density to be solenoidal (i.e. electrostatic fields shielded by the plasma), only the azimuthal current density are to be estimated since the axial component is determined from the continuity equation as follows:

$$J_z\,(m, k_z, \omega) = -\frac{m}{r_b k_z} J_\theta\,(m, k_z, \omega) \tag{2.7}$$

Thanks to the current-sheet model of the antenna, we are capable of simulating several antenna configurations. Figure 2.2 shows the common types of radiofrequency antennas used for Inductively Coupled Plasma sources (ICPs) and helicon sources: (a) single loop, (b) Nagoya Type III, (c) fractional helix, (d) integral t-turn helix; all of them are easily treated by the current-sheet model by using the opportune spatial spectra obtained from their spatial Fourier transforms (Appendix B). The perfectly conductive boundary conditions at

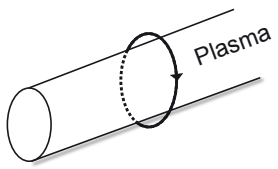

(a) Single Loop.

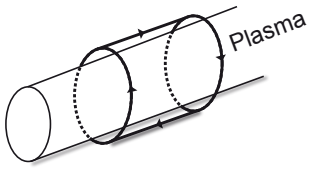

(b) Nagoya Type III.

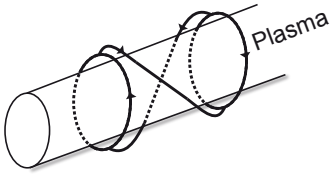

(c) Fractional helix.

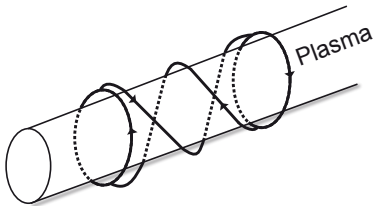

(d) Integral t-turn helix.

Figure 2.2: Most common antenna configurations for helicon plasma source.

$r = r_c$ require that the tangential components of $\boldsymbol{E}$ vanish at the chamber surface:

$$E_\theta\,(r = r_c) = E_z\,(r = r_c) = 0 \tag{2.8}$$

The constitutive equations Eqs. 2.4–2.5 provide a good linear approximation for fields of small amplitude. In vacuum the tensors $\boldsymbol{\epsilon}$ and $\boldsymbol{\mu}$ are simply diagonal, with components equal to vacuum permittivity ϵ_0 and vacuum permeability μ_0. The electrical response of a magnetized plasma can be reduced to a non-diagonal tensor $\boldsymbol{\epsilon}$ with five non-zero

elements [46]:

$$\boldsymbol{\epsilon} = \epsilon_0 \begin{bmatrix} S & -iD & 0 \\ iD & S & 0 \\ 0 & 0 & P \end{bmatrix} \tag{2.9}$$

where

$$S = 1 + \sum_{\alpha} \frac{\omega_{p\alpha}^2}{2\omega \left|k_z\right| v_\alpha} \left[Z\left(\zeta_{-1}^{\alpha}\right) + Z\left(\zeta_{+1}^{\alpha}\right) \right] \tag{2.10}$$

$$D = \sum_{\alpha} \frac{\omega_{p\alpha}^2}{2\omega \left|k_z\right| v_\alpha} \left[Z\left(\zeta_{-1}^{\alpha}\right) - Z\left(\zeta_{+1}^{\alpha}\right) \right] \tag{2.11}$$

$$P = 1 - \sum_{\alpha} \frac{\omega_{p\alpha}^2 Z'\left(\zeta_0^{\alpha}\right)}{k_z^2 v_\alpha^2 + i\nu_\alpha \left|k_z\right| v_\alpha Z\left(\zeta_0^{\alpha}\right)} \tag{2.12}$$

and $\omega_{p\alpha} \equiv \sqrt{n_\alpha q_\alpha^2 / \epsilon_0 m_\alpha}$ is the plasma frequency, $\omega_{c\alpha} \equiv \epsilon_\alpha q_\alpha B_0 / m_\alpha$ is the gyrofrequency, $v_\alpha \equiv \sqrt{2T_\alpha / m_\alpha}$ is the particle thermal velocity, ν_α is the collision frequency. The function Z is the plasma dispersion function, tabulated by Fried and Conte [47],

$$Z\left(\zeta\right) = \frac{1}{\sqrt{\pi}} \int_{-\infty}^{+\infty} \frac{e^{-z^2}}{z - \zeta} dz\,, \quad \mathrm{Im}\,\zeta > 0 \tag{2.13}$$

with derivative equal to $Z' = dZ/d\zeta = -2[1 + \zeta Z(\zeta)]$. The argument $\zeta_{0,\pm1}^{\alpha}$ used in Eq. 2.12 is defined as:

$$\zeta_n^{\alpha} = \frac{\omega + i\nu_\alpha + n\omega_{c\alpha}}{k_z v_\alpha} \tag{2.14}$$

where the integer number n is the number of the cyclotron harmonics. Only the first harmonics $n = 0, \pm 1$ fall within the assumptions of validity, and give reasonable results. The tensor $\boldsymbol{\epsilon}$ has been assumed to be a function of radius, so that radial variation of plasma density, magnetic field, electron temperature, and neutral pressure can be taken into account. The superscript α in Eqs. 2.10, 2.11 and 2.12 is the index of the plasma species, for example $\alpha = 1, 2$ to indicate a two-species plasma of electrons and ions. Multiple-ionized species can be taken into account too, by simply adding them in the evaluation of S, D, P. In the numerical tests presented in the following sections, we will assume that the plasma ions are singly charged, hence $q_i = -q_e = |e|$. Collisional processes are taken into account in the tensor $\boldsymbol{\epsilon}$ using a Krook lumped model [46] in the motion equation, leading to the expressions of Eqs. 2.10, 2.11, 2.12. Equations 2.9–2.14 represent a reasonable approximation of the electrical behavior of a magnetized plasma. They loose of validity when non-linear effects of wave-particle interaction become relevant. In fact, the assumptions made in the derivation of the plasma tensor of Eq. 2.9 are that the Larmor radius ρ_L is small compared to the scale length of the wave field variation L_E (typically the wavelength), and that the wave frequency ω is not too close to the harmonics of the particle gyro-frequency for $|n| \geq 2$.

2.3 Finite difference solution

By means of Finite-Difference (FD) techniques, Maxwell equations Eqs. 2.2–2.5 have been discretized into a set of linear algebraic equations along the radial coordinate, reducing them to a linear system of the general form $\boldsymbol{Ax} = \boldsymbol{b}$. A constant radial step size Δr has been used along the radius, starting at the axis and ending at the chamber wall $0 < r < r_c$. In order to achieve a second-order accuracy on the spatial discretization error, a one-dimensional staggered mesh of Yee type has been used, avoiding spurious solutions [48]. Figure 2.3 shows the staggered grid along the radius, where the grid G_A is at "integer" points r_j, and grid G_B is at "half-integer" points $r_{j-1/2}$, with $j = 1, ..., N$. Using the shorthand notation

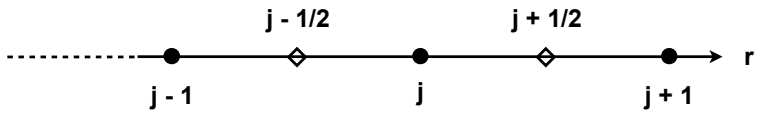

Figure 2.3: Computational grid along the radius, made of two staggered grids: grid G_A (full circles), grid G_B (empty diamonds).

$r_j = j\Delta r$ and $f_j = f(r_j)$, the derivative terms appearing in the Maxwell equations are approximated by the following discrete schemes in cylindrical coordinates:

$$\begin{aligned}
\left.\frac{\partial E_z}{\partial r}\right|_{r=j-1/2\Delta r} &= \frac{(E_z)_j - (E_z)_{j-1}}{\Delta r} \\
\left.\frac{1}{r}\frac{\partial}{\partial r}(rE_\theta)\right|_{r=j-1/2\Delta r} &= \frac{1}{r_{j-1/2}}\frac{(rE_\theta)_j - (rE_\theta)_{j-1}}{\Delta r} \\
\left.\frac{\partial}{\partial r}(cB_z)\right|_{r=j\Delta r} &= \frac{(cB_z)_{j+1/2} - (cB_z)_{j-1/2}}{\Delta r} \\
\left.\frac{1}{r}\frac{\partial}{\partial r}(rcB_\theta)\right|_{r=j-1/2\Delta r} &= \frac{1}{r_j}\frac{(rcB_\theta)_{j+1/2} - (rcB_\theta)_{j-1/2}}{\Delta r}
\end{aligned} \tag{2.15}$$

Substituting the discretized Eqs. 2.15 into the six Maxwell Eqs. 2.2 and 2.3, it results:

$$
\begin{aligned}
&\frac{1}{2}\left(-iDr\right)_{j-1/2}\left(E_\theta\right)_{j-1}+\left(SrE_r\right)_{j-1/2}-\frac{k_z}{k_0}\left(rcB_\theta\right)_{j-1/2}+\frac{m}{k_0}\left(cB_z\right)_{j-1/2}+\\
&\quad+\frac{1}{2}\left(-iDr\right)_{j-1/2}\left(E_\theta\right)_{j}=-i\frac{\left(rJ_r\right)_{j-1/2}}{\epsilon_0\omega}\\
&\quad i\frac{r_{j-1/2}}{k_0\Delta r}\left(E_z\right)_{j-1}-\frac{k_z}{k_0}\left(rE_r\right)_{j-1/2}+\left(rcB_\theta\right)_{j-1/2}-i\frac{r_{j-1/2}}{k_0\Delta r}\left(E_z\right)_{j}=0\\
&-i\frac{1}{k_0\Delta r}\left(rE_\theta\right)_{j-1}+\frac{m}{k_0}\left(E_r\right)_{j-1/2}+\left(rcB_z\right)_{j-1/2}+i\frac{1}{k_0\Delta r}\left(rE_\theta\right)_{j}=0\\
&\quad\left(rcB_r\right)_{j}+\frac{k_z}{k_0}\left(rE_\theta\right)_{j}-\frac{m}{k_0}\left(E_z\right)_{j}=0\\
&-\frac{1}{2}\left(-iDr\right)_{j}\left(E_r\right)_{j-1/2}-i\frac{r_j}{k_0\Delta r}\left(cB_z\right)_{j-1/2}+\frac{k_z}{k_0}\left(rcB_r\right)_{j}+\left(SrE_\theta\right)_{j}+\\
&-\frac{1}{2}\left(-iDr\right)_{j}\left(E_r\right)_{j+1/2}+i\frac{r_j}{k_0\Delta r}\left(cB_z\right)_{j+1/2}=0\\
&\quad i\frac{1}{k_0\Delta r}\left(rcB_\theta\right)_{j-1/2}-\frac{m}{k_0}\left(cB_r\right)_{j}+\left(PrE_z\right)_{j}-i\frac{1}{k_0\Delta r}\left(rcB_\theta\right)_{j+1/2}=-i\frac{\left(rJ_z\right)_{j}}{\epsilon_0\omega}
\end{aligned}
\tag{2.16}
$$

where the first three equations are valid for $j = 2, \ldots, N$, and the last three for $j = 1, \ldots, N-1$. Equations 2.16 can be written as a linear system with three unknowns on radial grid point $j - 1/2$ and three unknowns on radial grid point j,

$$
\boldsymbol{x} = \begin{bmatrix}
\left(E_r\right)_{j-1/2}\\
\left(cB_\theta\right)_{j-1/2}\\
\left(cB_z\right)_{j-1/2}\\
\left(cB_r\right)_{j}\\
\left(E_\theta\right)_{j}\\
\left(E_z\right)_{j}
\end{bmatrix}
\tag{2.17}
$$

In Eqs. 2.16 and 2.17 the magnetic induction $\boldsymbol{B}$ has been normalized by multiplying it by the speed of light c, in order to have all the unknowns roughly of the same order of magnitude and with the same units of V/m.

The boundary conditions of Eq. 2.8 at the conducting boundary $r = r_c$ become two conditions on the last point of the grid:

$$
\left(E_\theta\right)_N = \left(E_z\right)_N = 0 \tag{2.18}
$$

At the symmetry axis at $r = 0$ we need the following three special equations for the

components $(E_r)_{1/2}$, $(cB_\theta)_{1/2}$ and $(cB_z)_{1/2}$:

$$(SrE_r)_{1/2} - \frac{k_z}{k_0}(rcB_\theta)_{1/2} + \frac{m}{k_z}(cB_z)_{1/2} + \frac{3}{2}(-iDr)_{1/2}(E_\theta)_1 \tag{2.19}$$
$$-\frac{1}{2}(-iDr)_{1/2}(E_\theta)_2 = -i\frac{(rJ_r)_{1/2}}{\epsilon_0\omega}$$

$$-\frac{k_z}{k_0}(rE_r)_{1/2} + (rcB_\theta)_{1/2} + i\frac{1}{k_0}(E_z)_1 - i\frac{3}{2k_0}(E_z)_2 + i\frac{1}{2k_0}(E_\theta)_3 = 0 \tag{2.20}$$

$$\frac{m}{k_0}(E_r)_{1/2} + (rcB_z)_{1/2} - i\frac{2}{k_0}(E_\theta)_1 + i\frac{6}{k_0}(E_\theta)_2 - i\frac{3}{k_0}(E_\theta)_3 = 0 \tag{2.21}$$

The six unknowns per grid point are then stored in a one-dimensional array to get the coefficient matrix $\boldsymbol{A}$, which is large, sparse, not-symmetric and with non-zero elements in complex domain. Figure 2.4 shows the structure of the matrix $\boldsymbol{A}$ for a trivial mesh of $N = 5$ radial points. The red stars represent the locations of the matrix with non-zero elements, the other zero elements are left empty. The figure also shows how the structure of the matrix is modified by the physical medium where electromagnetic propagation occurs. Figure 2.4(a) shows a case with vacuum on all the domain, and Figure 2.4(b) a case with a plasma-filled waveguide. When the plasma is present, the dielectric tensor $\boldsymbol{\epsilon}$ of Eq. 2.9 is non-diagonal and non-symmetric, thus modifying the structure of the non-zero coefficients of the matrix. The column vector $\boldsymbol{b}$ of the system is made by the forcing terms $J_{r,\theta,z}$ of the

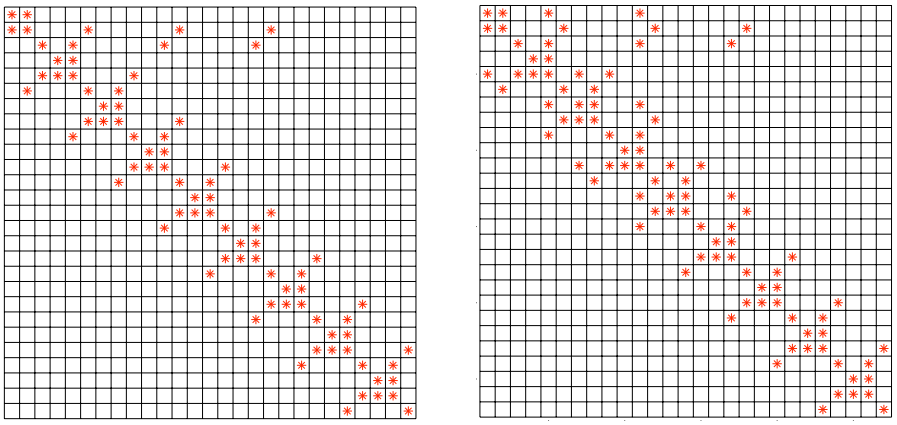

(a) (b)

Figure 2.4: Structure of the system matrix in (a) vacuum and (b) plasma simulation.

antenna current distribution. In the thin-wire approximation Eq. 2.6, the negligible radial extension constrains the current at the location $r = r_b$ by means of the Dirac delta. This is numerically modeled by means of a "tent" function with $1/\Delta r$ dependence, where Δr is the radial discretization step:

$$\delta(r - r_b) = \begin{cases} \frac{r - r_b + \Delta r}{\Delta r^2} & \text{for } r_b - \Delta r < r < r_b \\ \\ \frac{r_b + \Delta r - r}{\Delta r^2} & \text{for } r_b < r < r_b + \Delta r \end{cases} \tag{2.22}$$

2.4 Numerical solution

The linear system has been implemented in the C program called SPIREs, using the MUltifrontal Massively Parallel Solver (MUMPS)[49] library for the resolution of the system. MUMPS can solve general linear systems in complex domain with a direct method based on either the LU or LDL^T factorization. MUMPS has been chosen because of its well-known ability to treat square sparse matrices with complex data type, to exploit parallel CPUs, and for its fast execution speed. As an example of typical computational times, Table 2.1 shows the CPU time required by SPIREs for the solution of a test problem of a plasma-filled waveguide against different mesh refinements. The sequential (non-parallel) version of MUMPS has been used for this benchmark, calculations are done on a 2.0 GHz machine. As showed in Fig. 2.5, the C implementation is made up of several blocks, each

N radial nodes	time [s]
10^1	7.5×10^{-3}
10^2	1.6×10^{-2}
10^3	1.9×10^{-1}
10^4	2.0
10^5	$2.1 \times 10^{+1}$

Table 2.1: Computational time vs. mesh size for a wave propagation problem in a plasma-filled waveguide, as calculated using the sequential version of MUMPS on a 2.0 GHz machine.

one taking care of a particular task, as summarized briefly in the following list:

1. **Input**: all input quantities related to the geometry, antenna type, and plasma parameters are specified in the input file.

2. **Initialize**: the input file is read by the parser, and the informations gathered are used to allocate the necessary amount of memory to run efficiently the code. All electromagnetic quantities necessary to build the linear system are evaluated.

3. **Solve**: the linear system is analized, factorized and solved by MUMPS library.

4. **Output**: electromagnetic fields, plasma current densities and power deposition profiles are evaluated at each radial node and redirected to properly formatted output files.

2.5 Numerical Accuracy

The finite difference scheme presented in paragraph 2.3 is affected by three main sources of error on the solutions: (1) round-off error, (2) discretization error, and (3) discrete-sampling of the spectrum. The first is related to the finite-arithmetic of computers, the second to the finite difference approach, and the third is physical, since it affects the correct reconstruction of the electromagnetic wave variation from its spectral components. The method is not constrained by the Levy-Courant stability condition between spatial and temporal discretization, because stationary fields are solved in frequency domain. The

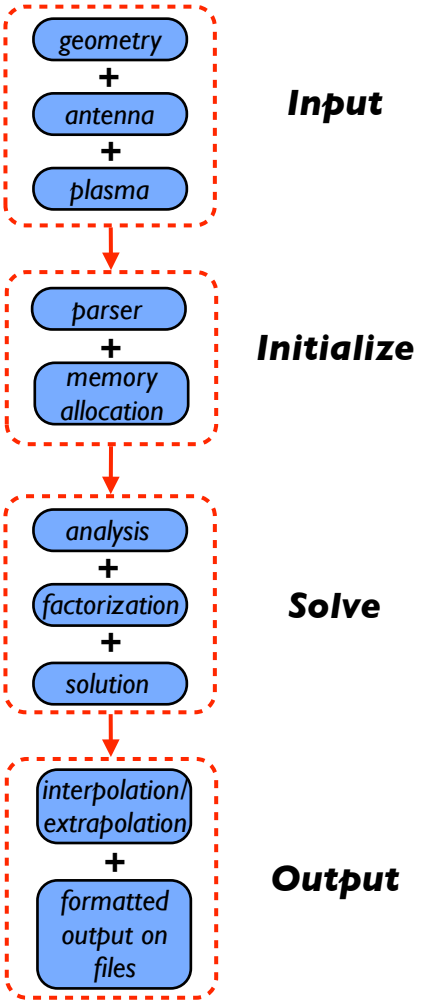

Figure 2.5: Numerical scheme implemented in SPIREs.

round-off error has been reduced simply by using double precision floating-point data format at 64-bit. In this paragraph we will focus on a detailed characterization of the discretization error of SPIREs. We will analyze the discrete-sampling error in the next paragraph, since it depends on the physical problem, validating SPIREs against two different physical situations, with vacuum and with plasma respectively. However, as a general fact, the discrete-sampling error forces the radial step size Δr to be smaller than the shortest spatial wavelength determined by the physical problem, in order to satisfy the Nyquist-Shannon sampling criterion. The discretization error has been quantitatively analyzed thanks to a sensitivity analysis of Δr against a reference analytical case in vacuum. The staggered Yee mesh has been expressly used to achieve a second order accuracy $O(\Delta r^2)$ on the solution. Consequently we expect a linear function of Δr with a slope $s = 2$ in a log-log plot. Figure 2.6 shows the log-log plot of the discretization error $\Delta\epsilon$ as a function of Δr, on two arbitrary components of the fields, Im (B_r) Fig. 2.6(a), and Im (E_θ) Fig. 2.6(b). The total number of nodes N spans from $N = 10^1$ to $N = 10^4$. The calculated solution has

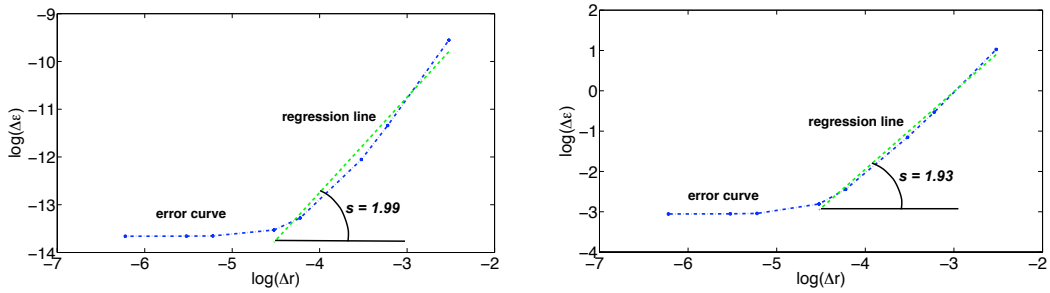

(a) Im (B_r). (b) Im (E_θ).

Figure 2.6: Discretization error $\Delta\epsilon$ as a function of the step size Δr of the radial grid, on two arbitrary components of the fields (a) imaginary component of the radial magnetic field Im (B_r), (b) imaginary component of the azimuthal electric field Im (E_θ). The expected slope s of the second order $O(\Delta r^2)$ Yee discretization in a log-log plot is $s = 2$.

a convergent asymptotic behavior toward the analytical solution, with slopes $s \approx 2$. More interesting, this analysis highlighted also the lower threshold in the number of radial nodes used, necessary to sample correctly the electromagnetic wave. When Δr is reduced below a threshold, the spatial discretization error becomes asymptotically independent of the radial discretization for finer resolutions. More relevant for plasma applications, a second

Test Label	n_0 $[\mathrm{m}^{-3}]$	B_0 [mT]
Small	10^{16}	6
Medium	5×10^{17}	40
Large	10^{19}	100

Table 2.2: Plasma parameters: uniform plasma density n_0 (flat density profile) and confinement magnetic field B_0 (DC confinement magnetic field).

test of mesh sensitivity has been conducted with a collisionless cold uniform plasma-filled waveguide. We investigated the response of SPIREs on a wide range of plasma parameters. The three cases have been selected in a range relevant for helicon and plasma processing applications, spanning from low-density low-magnetic-field (the "small" case, with plasma density 10^{16} m^{-3} and magnetic field $B_0 = 6$ mT), up to high-density high-magnetic-field (the "large" case, with plasma density 10^{19} m^{-3} and magnetic field $B_0 = 100$ mT). Plasma parameters have been reported in Table 2.2. Each case has been tested on meshes with an increasing number of nodes, from $N = 10^2$ to $N = 10^4$ radial nodes. The forcing antenna is placed on the plasma surface at $r_b = r_a$. Figure 2.7 shows the "small" case. The convergence on profiles is reached easily with $N = 10^3$ radial nodes, since profiles are smooth in this case. Figures 2.8 and 2.9, as expected, exhibit modes with shorter spatial wavelengths, that slow down the numerical convergence. However, even in the "Large" case of Fig. 2.9 SPIREs is able to converge toward the correct profile, showing in this case the coupled modes Helicon and Trivelpiece-Gould. In the next paragraph, a quantitative evaluation of the dispersion relation in the helicon range is obtained, showing a perfect quantitative agreement of SPIREs results with the Chen-Arnush generalized theory [25],

[26] of helicon waves. Furthermore, the asymptotic convergence of SPIREs proves that there are no method-related singularities in all the helicon range, as other methods have encountered in the past [26] in the high-density high-magnetic-field regime of helicons.

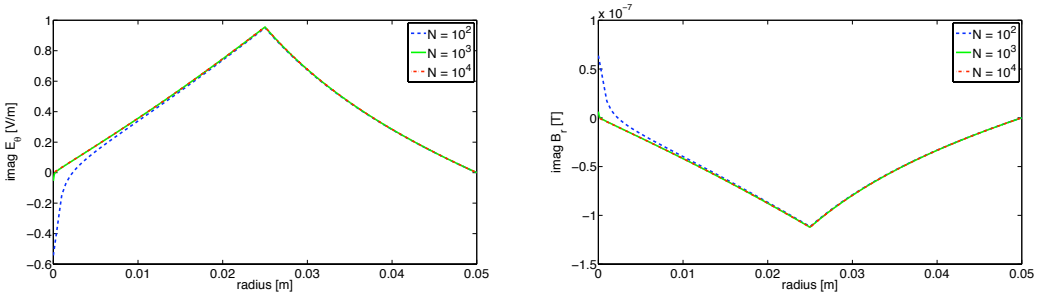

(a) (b)

Figure 2.7: Convergence on profiles at "Small" plasma parameters of (a) azimuthal Im (E_θ) and (b) radial Im (B_r).

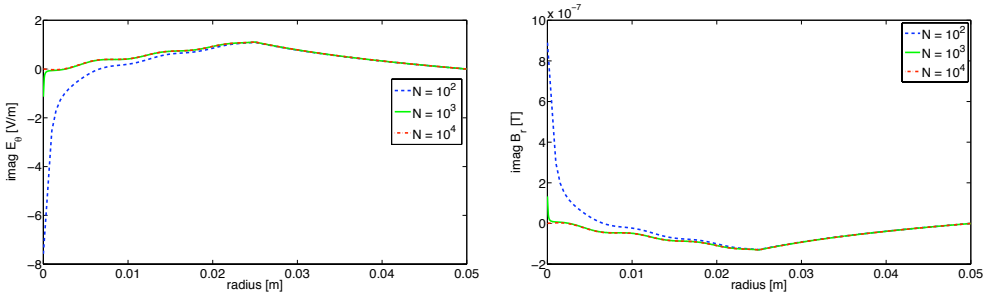

(a) (b)

Figure 2.8: Convergence on profiles at "Medium" plasma parameters of (a) azimuthal Im (E_θ) and (b) radial Im (B_r).

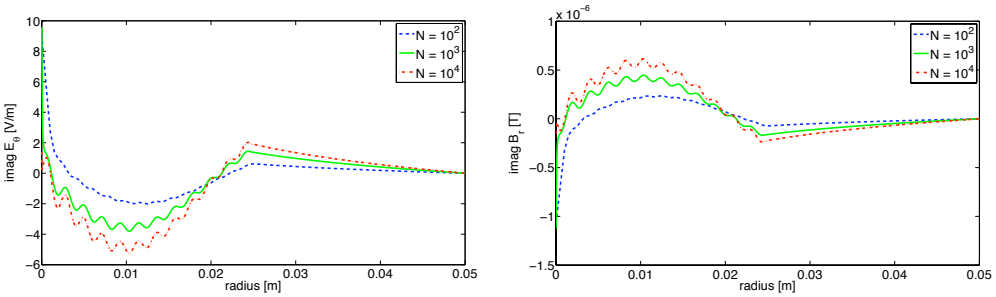

(a) (b)

Figure 2.9: Convergence on profiles at "Large" plasma parameters of (a) azimuthal Im (E_θ) and (b) radial Im (B_r).

2.6 Accuracy on physical cases

In order to provide evidence that the code can produce results that can be fruitfully compared with experimental data, we benchmarked the code firstly against analytical solutions of a forced waveguide in vacuum, and then against forced propagation of plasma waves in a uniform plasma cylinder at radiofrequency regime of helicons, where the correct dispersion relation of Helicon and Trivelpiece-Gould modes has been obtained [24]. Finally, we performed a quantitative comparison between the radial power absorption profiles and the plasma resistances produced by SPIREs and the HELIC code by Donald Arnush for different inhomogeneous plasmas.

2.6.1 Forced vacuum waveguide

With reference to Fig. 2.1, a circularly-shaped waveguide in vacuum and with perfectly conductive walls at $r = r_c$, uniform and unbounded along the axial direction, has been considered. An antenna placed at $r_b = r_a$ excites a current density along the azimuthal direction. The $\exp[i\,(m\theta + k_z z - \omega t)]$ dependence of fields and sources is implied and suppressed. The vacuum electromagnetic fields can be expanded into TM and TE waveguide modes, both in the inner ($0 < r < r_a$) and outer ($r_a < r < r_c$) regions. The axial field components satisfy Helmholtz's equations for TM and TE respectively:

$$\begin{cases} \left(\nabla_t^2 + k_t^2\right) E_z &= 0 \\ \left(\nabla_t^2 + k_t^2\right) H_z &= 0 \end{cases} \tag{2.23}$$

which is a system of differential equations in cylindrical coordinates, where $\nabla_t^2 = \frac{1}{r}\frac{\partial}{\partial r}\left(\frac{\partial}{\partial r}\right) + \frac{1}{r^2}\frac{\partial^2}{\partial \theta^2}$ and $k_t^2 = \mu\epsilon\omega^2 - k_z^2$. The transversal components of the TE and TM modes are:

$$\begin{aligned} \boldsymbol{E_t}\,(r) &= \frac{i}{k_t^2}\left[k_z \nabla_t E_z - \mu\omega \hat{\boldsymbol{z}} \times \nabla_t H_t\right] \\ \boldsymbol{H_t}\,(r) &= \frac{i}{k_t^2}\left[\mu k_z \nabla_t H_z + \mu\epsilon\omega \hat{\boldsymbol{z}} \times \nabla_t E_t\right] \end{aligned} \tag{2.24}$$

where $\nabla_t = \frac{\partial}{\partial r}\hat{\boldsymbol{r}} + \frac{1}{r}\frac{\partial}{\partial \theta}\hat{\boldsymbol{\theta}} = \frac{\partial}{\partial r}\hat{\boldsymbol{r}} + i\frac{m}{r}\hat{\boldsymbol{\theta}}$, and $\hat{\boldsymbol{r}}$ and $\hat{\boldsymbol{\theta}}$ are the unit vectors along the radial and azimuthal directions, respectively. The analytical solutions of the TM component are in the form:

$$\begin{cases} E_{z,\text{inner}} &= A_1 J_m\,(k_t r) \\ E_{z,\text{outer}} &= B_1 J_m\,(k_t r) + C_1 Y_m\,(k_t r) \end{cases} \tag{2.25}$$

Similarly the solutions of the TE component are:

$$\begin{cases} H_{z,\text{inner}} &= A_2 J_m\,(k_t r) \\ H_{z,\text{outer}} &= B_2 J_m\,(k_t r) + C_2 Y_m\,(k_t r) \end{cases} \tag{2.26}$$

where J_m and Y_m are the Bessel functions of the first and second kind, respectively. The six unknown constants $A_{1,2}$, $B_{1,2}$, $C_{1,2}$ are obtained imposing the boundary conditions. At the conducting boundary $r = r_c$, the tangential components of the electric field vanish,

$$E_{\theta,r_c} = E_{z,r_c} = 0 \tag{2.27}$$

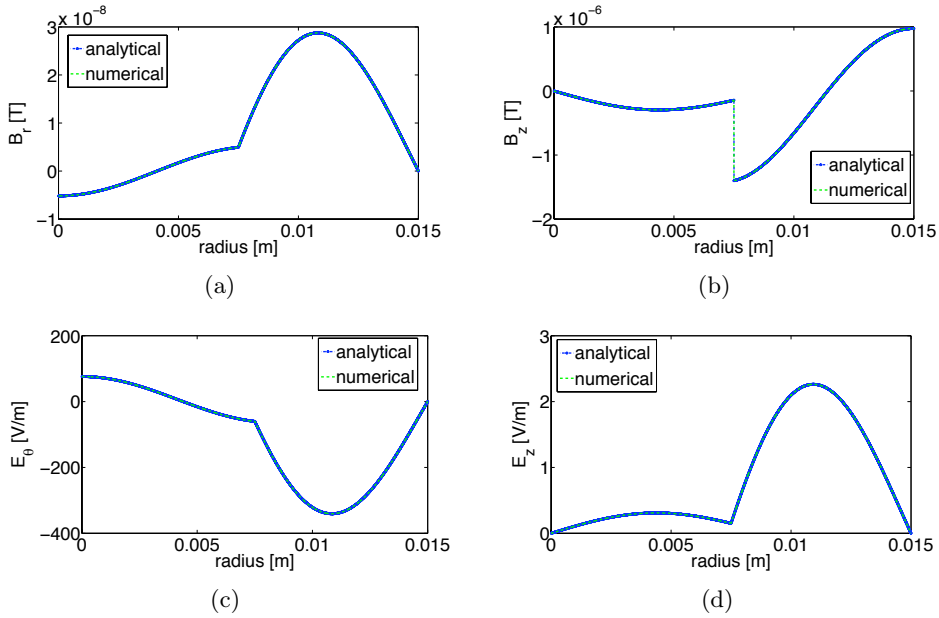

Figure 2.10: Comparison between analytical and numerical solutions of field components (a) radial $\mathrm{Im}(B_r)$, (b) axial $\mathrm{Re}(B_z)$, (c) azimuthal $\mathrm{Im}(E_\theta)$, and (d) axial $\mathrm{Im}(E_z)$, in a forced vacuum waveguide for the following parameters: $r_a = r_b = 7.5 \cdot 10^{-3}$ m , $r_c = 1.5 \cdot 10^{-2}$ m, $f = 20.0 \cdot 10^9$ Hz , $m = 1$, $k_z = 10.0$, $J_\theta = 1.0$ A/m.

across the antenna current $r = r_b$, the tangential components of the electric field and the azimuthal component of magnetic field are continuous,

$$E_{\theta,r_a^-} = E_{\theta,r_a^+} \quad , \quad E_{z,r_a^-} = E_{z,r_a^+} \quad , \quad H_{\theta,r_a^-} = H_{\theta,r_a^+} \tag{2.28}$$

and finally, according to Ampere's law, across the current distribution the axial component of magnetic field is discontinuous of a quantity equal to J_θ:

$$H_{z,r_a^-} - H_{z,r_a^+} = J_\theta \tag{2.29}$$

From the conditions of Eq. 2.27–2.29 substituted in Eq. 2.25–2.26, we obtain a 6×6 non-homogeneous algebraic system in the six unknowns constants $A_{1,2}$, $B_{1,2}$, $C_{1,2}$ whose non-zero elements are complex functions of medium properties and of Bessel functions [50]. The analytical solution has been compared with the solution calculated by SPIREs. Figure 2.10 shows the comparison between the analytical solution and the calculated one. Using a mesh of $N = 10^5$ radial nodes the percent error between the two solutions is less than $< 0.01\%$.

2.6.2 Forced plasma-filled waveguide

SPIREs has been used to study the propagation of electromagnetic plasma waves inside a magnetized plasma column of radius r_a at frequencies in the megahertz range. The propagation is forced by an axisymmetric antenna $m = 0$, at the frequency $f = 13.56$ MHz commonly used in industrial plasma sources. In this range of frequencies two coupled plasma waves can propagate inside the magnetized plasma column, namely the Helicon and Trivelpiece-Gould (TG) waves [24]. The first wave has a long transverse wavelength λ_1, the second a short one λ_2. The values of the two wavelengths $\lambda_{1,2}$ is expressed by the dispersion relation [24]:

$$\lambda_{\perp_{1,2}}\left(n_{\parallel}\right) = 2\pi \left[n_{\parallel}^2 \frac{\omega_{ce}^2}{4c^2} \left(1 \mp \sqrt{1 - 4\frac{\omega_{pe}^2}{\omega_{ce}^2}\frac{1}{n_{\parallel}^2}} \right)^2 - n_{\parallel}^2 \frac{\omega^2}{c^2} \right]^{-1/2} \tag{2.30}$$

where $\lambda_{\perp_{1,2}}$ is the transverse wavelength of the Helicon and TG modes respectively, ω_{pe} is the plasma frequency, ω_{ce} is the electron cyclotron frequency, $\omega = 2\pi f$ is the antenna angular frequency, c is the speed of light, and $n_{\parallel}$ is the parallel wave number, defined as $n_{\parallel} = k_z/k_0$, where $k_0 = \omega/c$ is the vacuum wave number. Figure 2.11 shows the analytical curve of Eq. 2.30 calculated for axial magnetic field $B_0 = 25$ mT and electron density $n_0 = 10^{18}$ m^{-3}. The figure shows that for a given $n_{\parallel}$, the two perpendicular modes $\lambda_{1,2}$ concurs at the same time. The same numerical case has then been simulated using SPIREs, spanning in the range of parallel wave numbers $n_{\parallel} = 30, 40, ..., 90$. The radius r_a of the plasma column was selected at each case such as to sample the longer helicon wave at least in ten periods. The propagating fields in the plasma are forced by the antenna current placed at radius $r_b = r_a$, and enclosed inside a cylinder of radius $r_c = 2r_a$. From the numerical side, the presence of the plasma modifies the structure of the resolutive coefficient matrix of SPIREs, as already anticipated and showed in Fig. 2.4(b). An example of field solution is given in Fig. 2.9, where the two coupled modes are evident: in that case the short TG wavelength appears with at least 10 periods, the long helicon wavelength appears only with half a period. The numerical values of the two transverse modes $\lambda_{1,2}$ are then obtained from the fields of SPIREs by means of an FFT procedure. The FFT radial spectrum exhibited always two distinct peaks, corresponding to the two values of λ_1 and λ_2. Figure 2.11 shows the values extracted from the SPIREs solution after the FFT, marked with black points. Both the H and the TG branches are overlapped to the theoretical curve with percent error less than $< 1\%$. Figure 2.12 illustrates the electromagnetic Poynting flux for the magnetized plasma column with the same plasma parameters of Fig. 2.11. The complex power is transmitted from the antenna to the plasma, where the electromagnetic waves deposit their energy. The Poynting flux is negative there, meaning that the flux is incoming into the dissipative plasma column. A stationary electromagnetic wave is established in the external vacuum region comprised between the plasma and the conductive boundary, with a zero Poynting flux. The gradient of the flux is maximum at the plasma-vacuum transition.

In order to make an independent benchmarking of our code with another existing code, we have performed a quantitative comparison between SPIREs and HELIC [26], evaluating the radial profiles of power deposition and the value of plasma resistance for different density profiles of collisional magnetized plasma cylinders. The density profiles have been

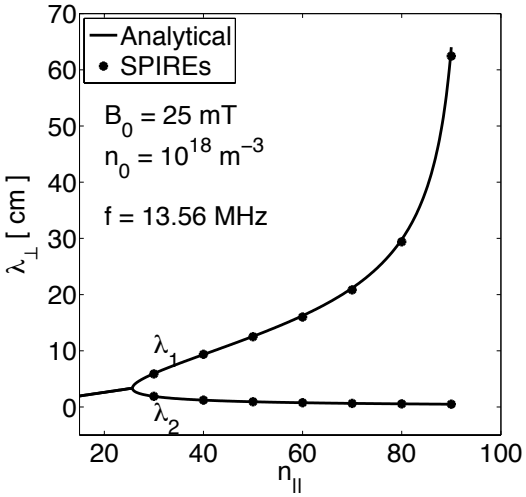

Figure 2.11: Analytical vs. calculated dispersion relation in the Helicon–TG radiofrequency regime; the plot shows the two radial wavelengths λ_1 (Helicon) and λ_2 (Trivelpiece-Gould) of the perpendicular modes as a function of the parallel wave number $n_{\|}$.

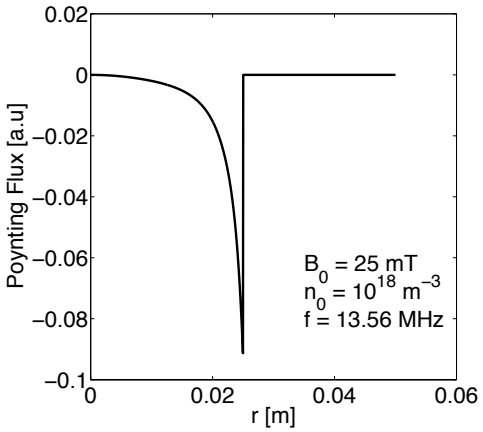

Figure 2.12: Radial Poynting flux for a uniform magnetized plasma column.

parametrized as follows:

$$n(s,t,r) = n_{r=0}\left[1-\left(\frac{r}{w}\right)^{s}\right]^{t} \quad , \quad w = \frac{r_a}{\left[1-f_a^{1/t}\right]^{1/s}} \tag{2.31}$$

where f_a is the relative density n/n_0 at $r = r_a$. Density profiles corresponding to $n\,(2,1,r)$ and $n\,(10,1,r)$ have been considered as a benchmark, as reported in Fig. 2.13(a) and Fig. 2.13(b). The two figures Fig. 2.13(c) and Fig. 2.13(d) show the radial profiles of power absorption as evaluated by SPIREs and by HELIC. The curves are overlapped better than 1% over all the radial domain, and the plasma resistances agree with a percent error less than $< 1\%$.

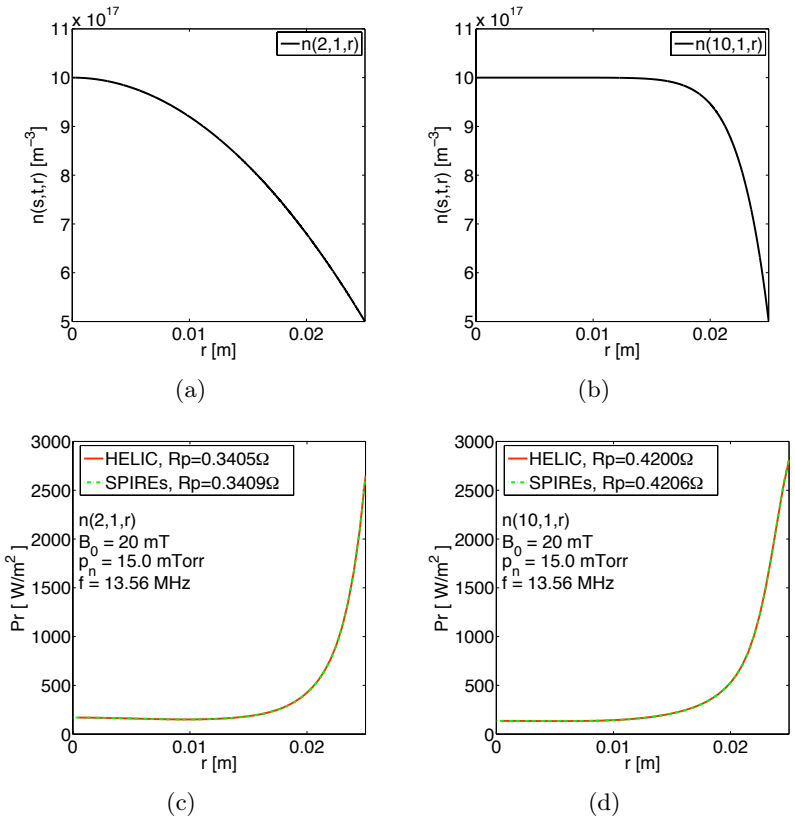

Figure 2.13: Comparison of SPIREs vs. HELIC for two cases of inhomogeneous magnetized plasmas: (a) first density profile $n\,(2,1,r)$, (b) second density profile $n\,(10,1,r)$, (c) radial profile of power deposition for $n\,(2,1,r)$, and (d) radial profile of power deposition for $n\,(10,1,r)$. The value of the plasma resistance Rp has been reported in the legend, as obtained from each code. Parameters are: $r_a = r_b = 2.5 \cdot 10^{-2}$ m, $r_c = 5.0 \cdot 10^{-2}$ m, $f = 13.56 \cdot 10^6$ Hz , $B_0 = 20$ mT, $m = 0$, $J_\theta = 1.0$ A/m and neutral pressure $p_n = 15.0$ mTorr.

2.7 Results and discussion

Recalling that the propulsive figures of merit (i.e. the specific impulse and the thrust efficiency) are strictly related to the power deposition inside the plasma source, the influence of all the discharge parameters on the deposited power will be assessed in this section. For a given configuration, the trends allow to find the maximum load conditions, corresponding to the maximum power coupling between the antenna and the plasma load.
When source geometry (in terms of r_a, r_b, r_c), antenna type, working frequency, and plasma characteristics (in terms of gas type, neutral pressure, confinement magnetic field, plasma density) are given, Eq. 2.30 gives all the wave modes (m, k_z) that can propagate inside the plasma column. The power deposition due to collisional or collisionless damping and for all the accessible propagative modes can be evaluated by

$$P = \frac{1}{2}\int_{V_{plasma}} \boldsymbol{E}^* \cdot \boldsymbol{J_{plasma}} dV = \frac{|I_0^2|}{2}\left(R_p + iX_p\right) \tag{2.32}$$

where P is the complex electrical impedance, $\boldsymbol{E^*}$ is the conjugate electric field inside the plasma, $\boldsymbol{J_{plasma}}$ is the plasma current density, I_0 is the antenna current, R_p and X_p are the electrical resistance and reactance, respectively. The actual power coupled by the antenna is the electrical resistance R_p per unit axial length in Ω/m since uniform plasma sources along the axial direction will be considered.

2.7.1 Difference between $m = 0$ and $m = +1$ modes

Three different homogeneous magnetized plasma sources with $r_a = 1.0 \cdot 10^{-2}$ m, $r_a = 2.5 \cdot 10^{-2}$ m, $r_a = 5.0 \cdot 10^{-2}$ m, are given. Consider the wave polarization $m = 0$ excited by a single loop antenna, whereas the mode $m = +1$ excited by a Nagoya Type III with an axial length $L = 0.1$ m. The electrical resistance is plotted in Figs. 2.14,2.15 as function of the plasma for two different working frequency, $f = 13.56$ MHz and $f = 27.12$ MHz, respectively.
Considering the plasma resistance R_p showed in Fig. 2.14 in the $m = 0$ excitation case, a maximum load condition can be identified for each working frequency and B_0 magnetic field. In the low magnetic field configurations showed in Figs. 2.14 (a),(d), a maximum plasma resistance can be easily identified whereas in the higher confinement magnetic field configurations showed in Figs. 2.14 (b),(c),(e),(f), a plateau develops for a given density value, which depends on the specific B_0 considered, and gets higher for decreasing values of the plasma radius.
As a rule of thumb, the plasma resistance gets higher for higher working frequency, given a source geometry and confinement magnetic field. Similar considerations can be done for the $m = +1$ case showed in Fig. 2.15, where the aforementioned rule works as well. Differently than the $m = 0$ case, in Fig. 2.15 there is a drop in the plasma resistance instead of a plateau as soon as a certain density value is reached; given the geometry, this value is higher for lower working frequency while it gets higher as soon as the confinement magnetic field increases.

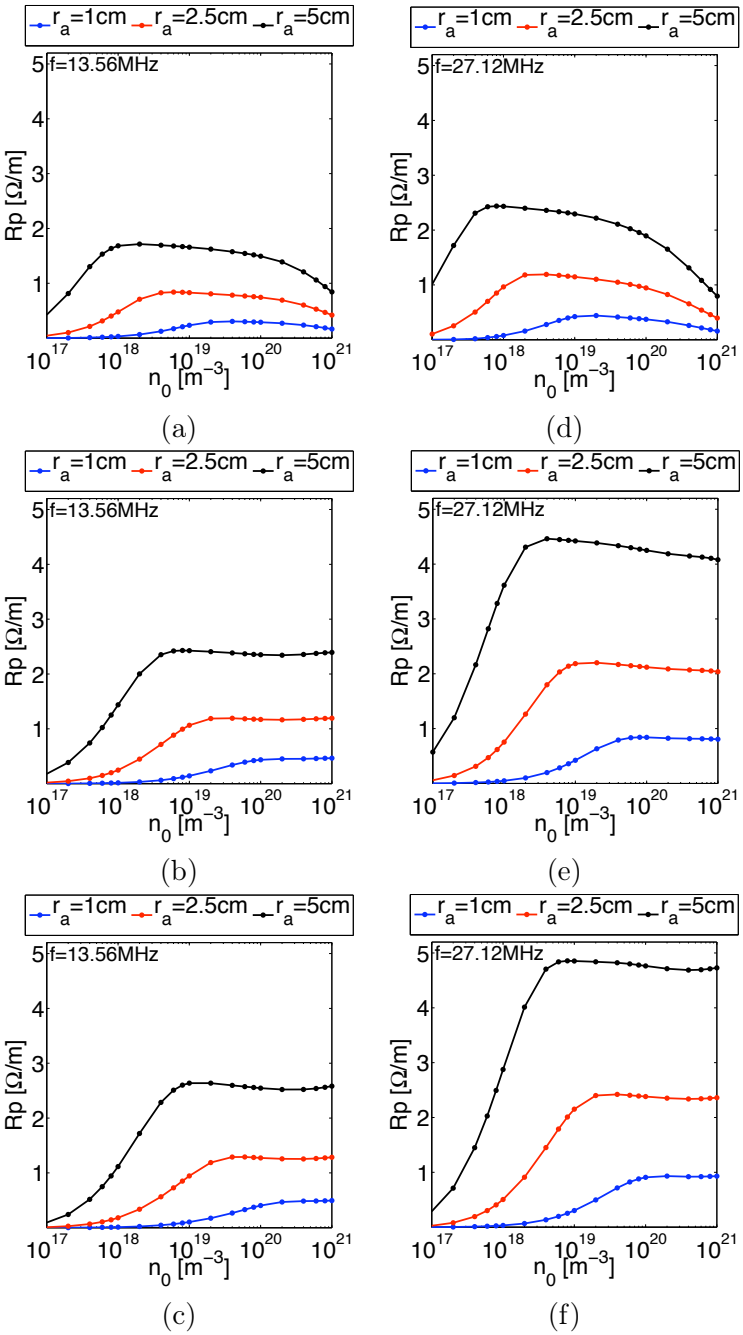

Figure 2.14: Electrical resistance as a function of the plasma density for three ($r_a = 1.0 \cdot 10^{-2}$ m, $r_a = 2.5 \cdot 10^{-2}$ m, $r_a = 5.0 \cdot 10^{-2}$ m) homogeneous magnetized plasma sources : (a),(d) $B_0 = 0.01$ T, (b),(e) $B_0 = 0.05$ T, (c),(f) $B_0 = 0.1$ T at $f = 13.56$ MHz and $f = 27.12$ MHz, respectively. Parameters are: $m = 0$ single loop antenna, $J_\theta = 1.0$ A/m and neutral pressure $p_n = 15.0$ mTorr.

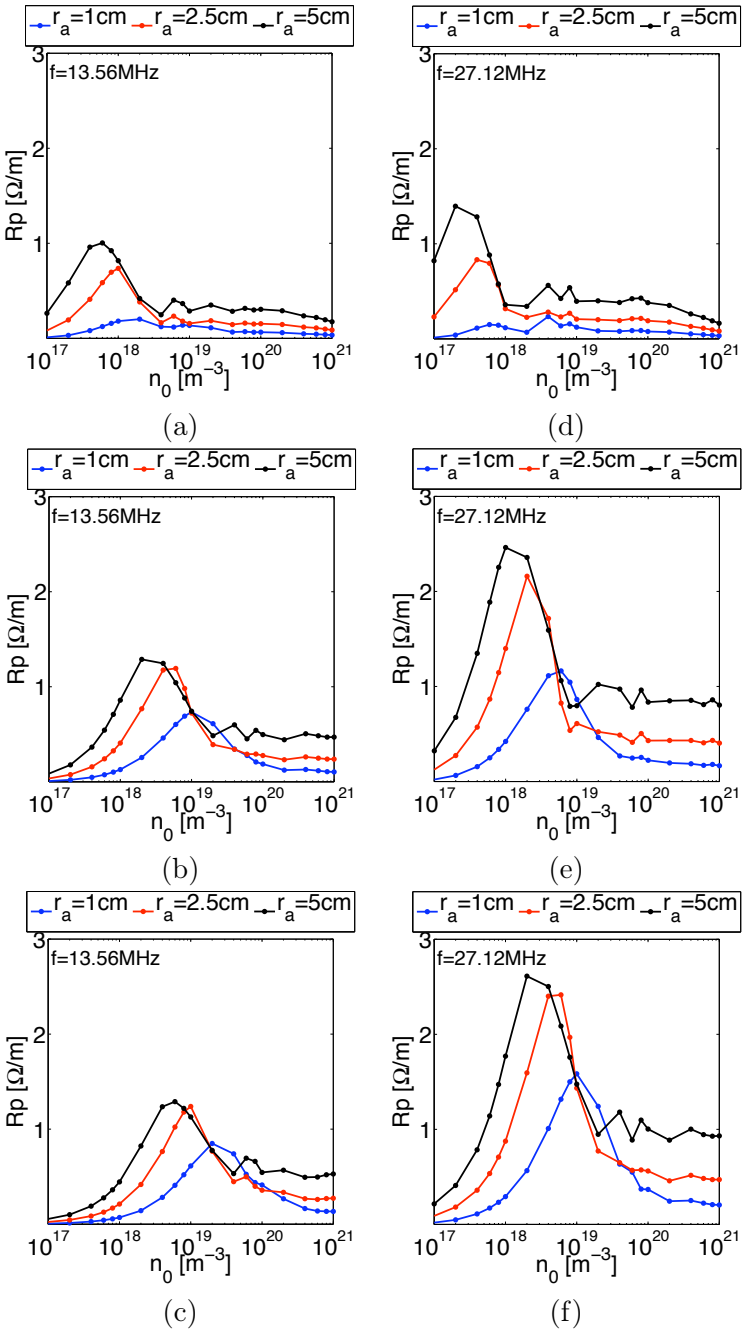

Figure 2.15: Electrical resistance as a function of the plasma density for three ($r_a = 1.0 \cdot 10^{-2}$ m, $r_a = 2.5 \cdot 10^{-2}$ m, $r_a = 5.0 \cdot 10^{-2}$ m) homogeneous magnetized plasma sources : (a),(d) $B_0 = 0.01$ T, (b),(e) $B_0 = 0.05$ T, (c),(f) $B_0 = 0.1$ T at $f = 13.56$ MHz and $f = 27.12$ MHz, respectively. Parameters are: $m = +1$ Nagoya Type III antenna with $L = 0.1$ m, $J_\theta = 1.0$ A/m and neutral pressure $p_n = 15.0$ mTorr.

2.7.2 Influence of the plasma density profile

The importance of density gradient along the radial direction is now considered. With reference to Eq. 2.31, with a plasma source of $r_a = 0.025$ m, plasma density at the core $n_{r=0} = 1 \cdot 10^{18}$ m^{-3}, and $fa = 0.5$, the influence of three density profiles - usually found in experimental set-ups - $(2, 1, r)$, $(10, 1, r)$, and $(2, 10, r)$ will be analised. The results in

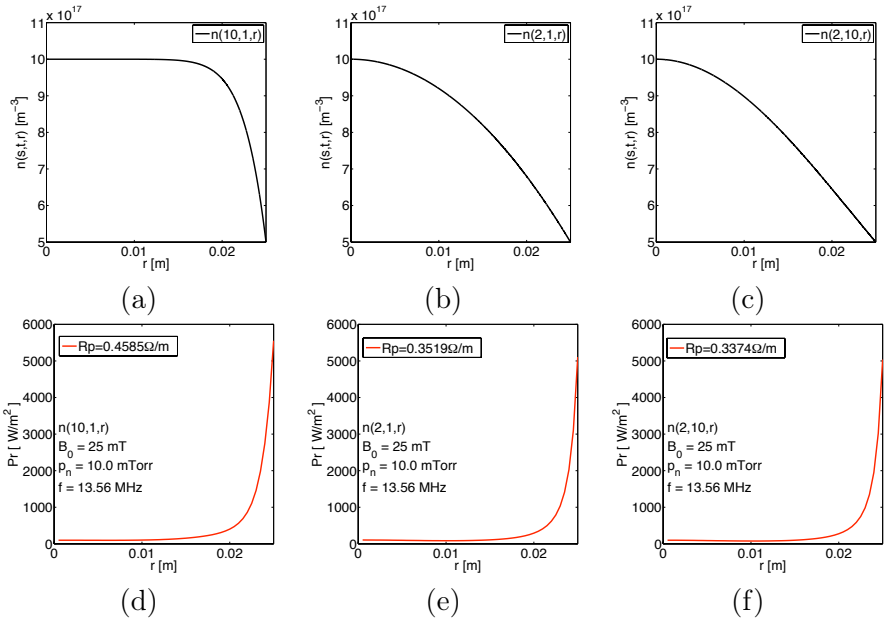

Figure 2.16: Comparison of radially inhomogeneous magnetized plasmas: (a) first density profile $n\,(10, 1, r)$, (b) second density profile $n\,(2, 1, r)$, (c) third density profile $n\,(2, 10, r)$, (d) radial profile of power deposition for $n\,(10, 1, r)$, (e) radial profile of power deposition for $n\,(2, 1, r)$, and (f) radial profile of power deposition for $n\,(2, 10, r)$. The value of the plasma resistance Rp has been reported in the legend. Parameters are: $r_a = r_b = 2.5 \cdot 10^{-2}$ m, $r_c = 5.0 \cdot 10^{-2}$ m, $f = 13.56 \cdot 10^6$ Hz , $B_0 = 25$ mT, $m = 0$, $J_\theta = 1.0$ A/m and neutral pressure $p_n = 10.0$ mTorr. The resistance for a uniform plasma density with $n = 10^{18}$ m^{-3} is $R_p = 0.5485\Omega/m$.

Fig. 2.16 show that the radial power deposition has the same behavior along the radial coordinate r independently of the density profile considered; the deposition of RF poweer occurs mainly at the edge of the plasma cylinder, where an electrostatic-like mode is rapidly damped by collisional processes, whereas a smaller contribution also comes from the Laundau damping of the wave due to wave-particle interactions, but it is usually negligible for cold plasmas at few electronvolts of electron temperature. Notice that each profile deposits as much more power inside the plasma as soon as it gets closer to the uniform plasma density profile, proving that the experimental set-up has to tend to this configuration in order to maximize the power coupling between antenna and plasma.

2.7.3 Plasma impedance - a parametric analysis

The influence of the confinement magnetic field, the working frequency, and the plasma discharge radius has been assessed. The plasma density ranges from 10^{18} to 10^{19} particles/m^3, the magnetic field is below $B < 0.15$ T, the working frequency ranges from 1 to 15 MHz, and the plasma cylinders have radius < 5 cm. The electrical impedance per unit length of the plasma is reported for each case in Fig. 2.17. For a given geometry, the trends allow

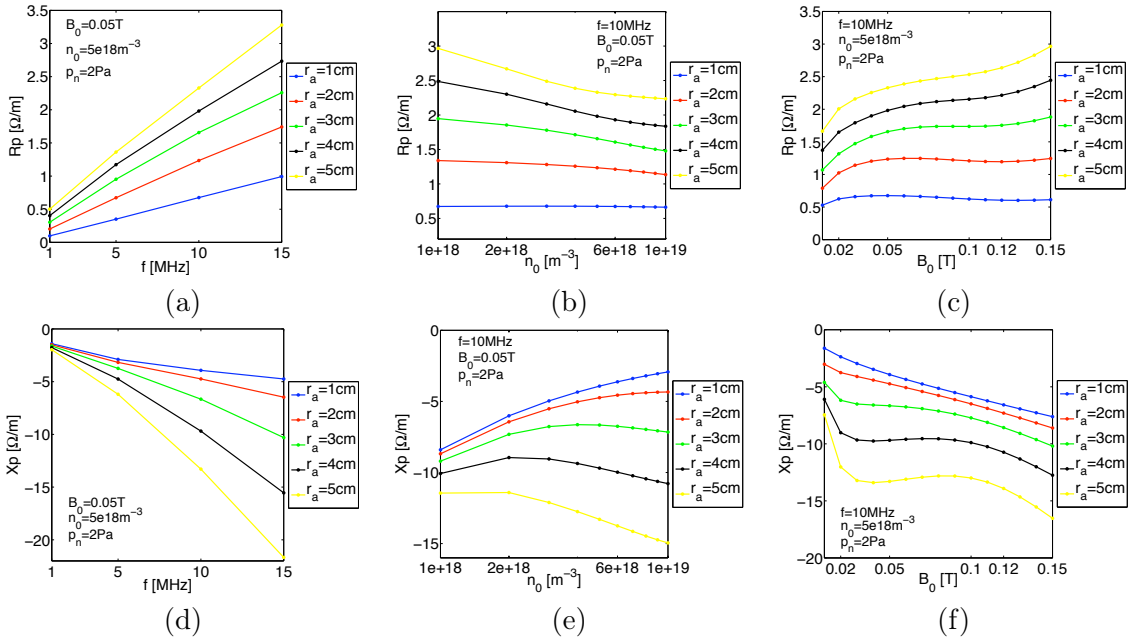

Figure 2.17: Electrical impedance as a function of the plasma parameters for five ($r_a = 1.0 \cdot 10^{-2}$ m, $r_a = 2.0 \cdot 10^{-2}$ m, $r_a = 3.0 \cdot 10^{-2}$ m, $r_a = 4.0 \cdot 10^{-2}$ m, $r_a = 5.0 \cdot 10^{-2}$ m) homogeneous magnetized plasma sources : (a),(d) $B_0 = 0.05$ T, $n_0 = 5 \cdot 10^{18}$ m^{-3}, $p_n = 15.0$ mTorr, (b),(e) $B_0 = 0.05$ T, $f = 10$ MHz, $p_n = 15.0$ mTorr, (c),(f) $f = 10$ MHz, $n_0 = 5 \cdot 10^{18}$ m^{-3}, $p_n = 15.0$ mTorr. Parameters are: $m = 0$ single loop antenna, $J_\theta = 1.0$ A/m.

to find the maximum load conditions (i.e maximum R_p), corresponding to the maximum power coupling between the antenna and the plasma load.

2.8 Conclusions

A one-dimensional Finite-Difference Frequency-Domain electromagnetic solver called SPIREs has been developed and used to study the wave propagation and power deposition phenomena in plasma of cylindrical shape. The Maxwell wave equations have been discretized along the radius of the plasma cylinder, and Fourier transformed along the other two dimensions and in time. The plasma has been represented by a dielectric tensor, which has been assumed to be radius-dependent. The radial dependence allows the treatment of inhomogeneous plasma profiles, with variations on plasma density, magnetic field, temperature, and collisional factor. The plasma can be multi-species, each species can be single-

or multiple-ionized. Governing equations have been discretized on a staggered Yee mesh in complex domain, and the problem has been reduced to the solution of a linear system with a single matrix inversion, accomplished by means of MUMPS library, exploiting fast execution speeds and parallel computation capabilities.
The sensitivity analysis on the step size of the grid proved a second order accuracy on the solution, and a convergent asymptotic behavior has been observed whenever the radial discretization goes below a given threshold, depending on the electromagnetic wavelength to be sampled.
The code has been validated in vacuum and in plasma against two analytical cases: the electromagnetic fields in a forced vacuum waveguide, and the forced plasma oscillation in the helicon radiofrequency regime. In both cases the percent error between the analytical and the numerical solutions was always less than $< 1\%$. The code has been benchmarked in inhomogeneous plasma against existing results produced by well established method such as HELIC [26]: the percent errors between the two numerical codes for the radial power deposition profile and plasma resistance are both less than 1%.
Once verified and validated, SPIREs has run an extensive simulation campaign to assess the influence of plasma parameters (e.g. discharge radius, plasma density, confinement magnetic field) on wave propagation, and power deposition phenomena. Most notably, the power deposition increased for larger discharge radius, higher confinement magnetic fields, and when the antenna excited even azimuthal mode number ($m = 0$) at higher frequency ($f = 27.12$ MHz). This parametric analysis can be fruitfully employed in the study, design and optimization of helicon source for space plasma thruster, and plasma antenna concepts. Moreover, as far as a helicon source for space plasma thruster is concerned, SPIREs can be used both as a tool that provides the electrical impedance for the preliminary design of the plasma source, and as an optimization tool to identify the best set of source parameters to maximize the power deposition - and so the propulsive figures of merit - considering the mass and power budgets allocated for the space thruster. Considering the plasma antenna, SPIREs can act a fundamental role in the preliminary evaluation of plasma conductivity, then used for the determination of the antenna radiation pattern.

Chapter 3

WAVEQM: Equilibrium Conditions Solver for radiofrequency heated plasma cylinders

3.1 Introduction

The equilibrium conditions of radiofrequency heated plasma cylinders have been calculated by solving the two coupled problems of the electromagnetic power deposition and the macroscopic transport of charged and neutral species. The electromagnetic power deposition along the radius of the cylinder has been solved by SPIREs code, providing the input source terms for the transport problem. The continuity and momentum equations of a single-ionized cold plasma, together with energy conservation, have been solved along the same radial direction by means of EQM code [51]. SPIREs and EQM codes have been coupled in WAVEQM code by means of an iterative procedure. The method allows the prediction of the profiles of plasma density, power deposition, electron temperature and neutral density in RF heated plasma cylinders. Numerical accuracy has been verified against typical conditions encountered in low-pressure helicon discharges, where the plasma is magnetized with an external field directed along the axis of the cylinder.

3.2 Methodology

A common way to obtain a cold weakly-ionized plasma is to excite a low-pressure gas (from 10^{-1} to 10^{1} Pa) contained in a cylinder with a radiofrequency antenna in the MHz range wrapped around the cylinder. The method is experimentally simple and reliable, and it is nowdays one of the most widespread technique for making a plasma source. A stable quiescent plasma at low density (10^{16}-10^{18} particles/m^3) can be obtained with these kind of sources. The addition of a magnetostatic field, with the magnetic induction vector directed preferably along the axis of the cylinder, allows (under the opportune conditions of wave frequency, field intensity and plasma density) the propagation of bounded plasma waves, capable of enhancing the RF coupling and increase the plasma density up to the rage of 10^{19} particles/m^3. This condition, typical of helicon experiments, is what we want

to analyze with WAVEQM model.
In order to evaluate the equilibrium, two coupled problems have been iteratively solved up to the convergence on the profiles, (i) the solution of the plasma-wave coupling problem, and (ii) the solution of the macroscopic transport of plasma and neutral species. For the solution of the first problem, the electromagnetic fields have been solved by SPIREs code; specifically, the anisotropic behavior of the magnetized plasma column is modeled using the classical Stix dielectric tensor(Eq. 2.9), comprising the extra-diagonal terms and thermal effects (Eq. 2.13). The electromagnetic wave launched by the antenna propagates into the plasma and is absorbed by the anisotropic medium; past studies [24], [25], [26] have demonstrated that the propagation of the electromagnetic waves into the plasma can excite two coupled plasma modes, usually referred as Helicon mode (fast wave), and Trivelpiece-Gould mode (slow wave), with different transverse wavelengths expressed by the dispersion relation in Eq. 2.30. These propagative modes couple RF power, which has been evaluated by integrating the electrical work, $\boldsymbol{E}^* \cdot \boldsymbol{J_{plasma}}$, done by the electric field $\boldsymbol{E}$ on the plasma currents $\boldsymbol{J_{plasma}}$, the integration being done over the volume V_{plasma} of propagation, as given by Eq. 2.32. The calculated RF power deposited into the plasma is then used as an input in the problem of the macroscopic transport (i.e. how the plasma reconfigures itself under the forcing action of the RF fields).
This second problem has been solved using a theory recently proposed for the evaluation of the equilibrium conditions of plasma cylinders of finite-length [51], which is based on the short-circuit effect originally proposed by Simon [52]. It is worth noticing that the theory developed in [51] has recently received an independent verification from dedicated two-dimensional Particle-in-Cell simulations [53], confirming the violation of the classical ambipolar cross-field transport due to the short circuiting of electrons at the axial boundaries of finite-extension cylinders. This theory has been implemented in the EQM code [51].
In EQM code, the local input power given at each radial location by the RF propagation is used by the plasma to overcome particle and inelastic losses. The particle losses are given by the convective fluxes of particles, and the inelastic losses come from the details of the atomic physics of the particular gas, and consists mostly of radiative losses. The coupling with the boundaries plays an important role in the final macroscopic configuration of the discharge, since electrons are short circuited at the end walls of the cylinder, where the magnetic lines intersect the walls.
The two codes SPIREs and EQM have been iterated together until convergence on the profiles, as schematized in Fig. 3.1. This approach allows the evaluation of all the relevant quantities commonly measured for the characterization of a plasma discharge, i.e. the value of the oscillating electric and magnetic fields, the profiles of plasma density, power deposition, electron temperature and neutral density.

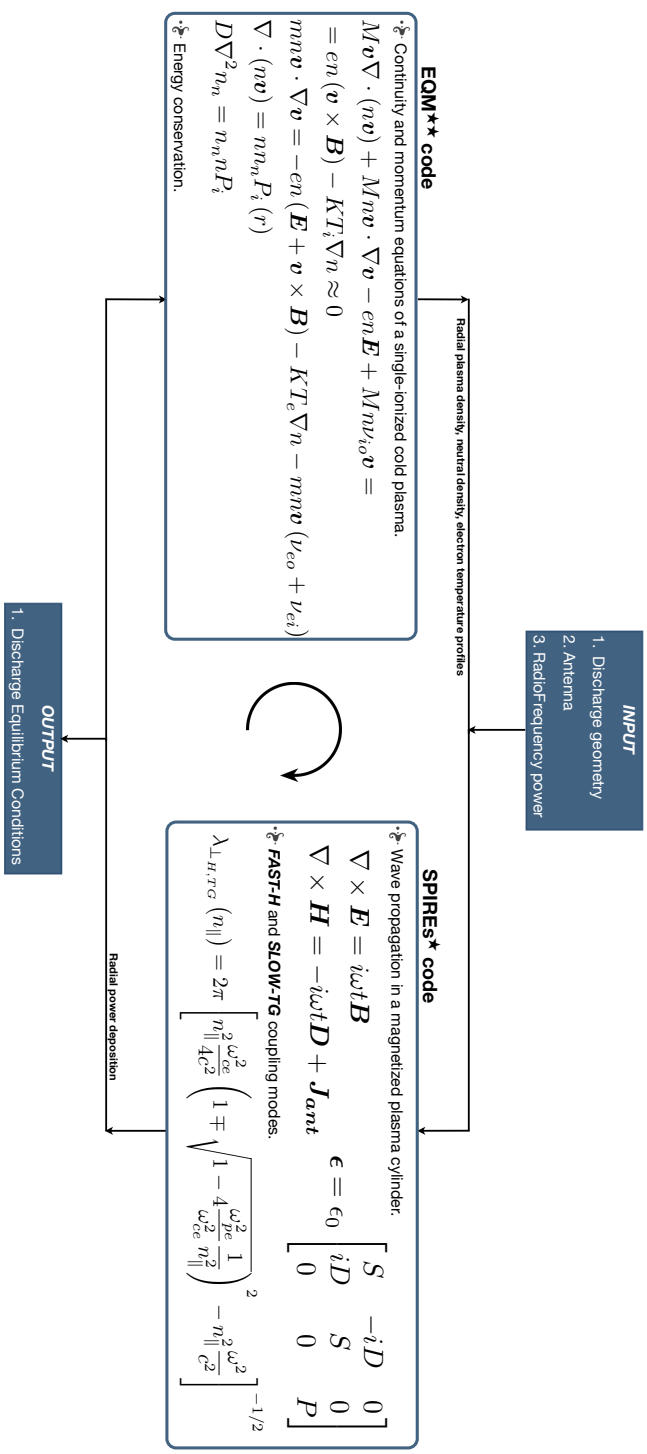

Figure 3.1: Governing equations and iterative strategy implemented in WAVEQM code.

3.3 Accuracy on physical case

The method has been used to evaluate the radial profiles at equilibrium of a cylindrical helicon discharge at low pressure. Convergence is usually obtained after few iterations, thus no particular treatment of the numerical convergence is necessary. As shown in Fig. 3.2, a cylindrical helicon discharge of Argon inside a dielectric tube of 5 cm of internal diameter has been considered, with assumed gas pressure of 18 mTorr (2.4 Pa), and a magneto-static field of 0.02 T along the axis of the cylinder. No particular treatment of the numerical convergence is thus necessary. As far as the above plasma discharge is concerned, the radial

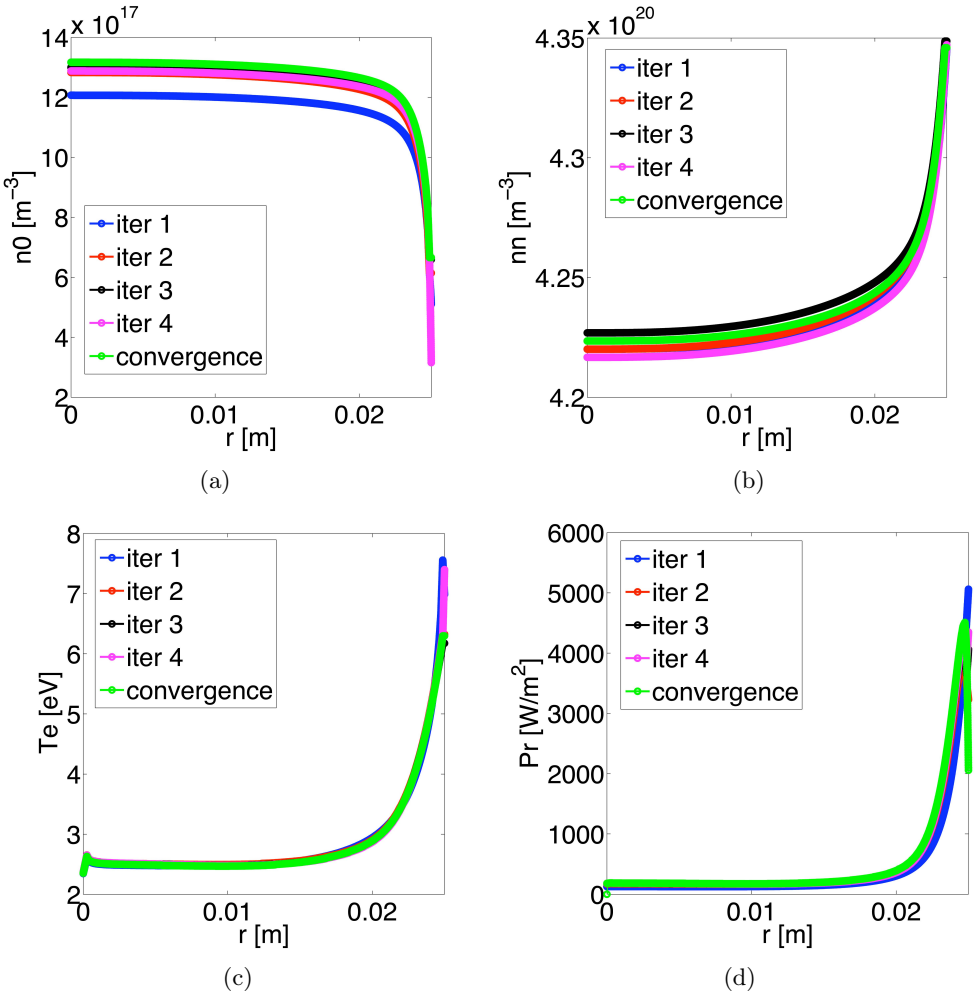

Figure 3.2: Convergence of the profiles: (a) plasma density, (b) neutral density, (c) electron temperature, (d) deposited power obtained from WAVEQM code, for a $P = 500$ W of RF input power in a magnetized positive column of $r_a = 0.025$ m of Argon plasma sustained by an $m = 0$ RF antenna. Gas pressure before the discharge $p_n = 18$ mTorr, antenna frequency 13.56 MHz, axial magnetostatic field 0.02 T.

profiles at equilibrium has been evaluated for three RF input power: $P = 250$ W, $P = 500$ W, $P = 750$ W. The numerical results have been reported in Fig. 3.3, where the radial

profiles at equilibrium for a $m = 0$ antenna, made with an axis-symmetric coil wrapped around the discharge tube, have been reported. The origin of the radial coordinate is placed at the axis of the cylinder. Fig. 3.3 shows (a) module of the RF electric field, (b) module of the RF magnetic field, (c) deposited power, (d) plasma density, (e) electron temperature, (f) density of the neutral gas, all at equilibrium and for the three power levels mentioned above. The amplitude of the fields is shown here per Ampere of current flowing on the antenna, at the location $z = 0$ at the antenna center. The calculation shows that the plasma density increases for an increasing RF power. Furthermore, the density profile is peaked at the center even if the power deposition occurs mostly near the edge of the cylinder. The electron temperature remains approximatively constant vs. the power. Electron temperature increases only at the edge of the discharge, where the field intensity is larger and where the specific power P_r is higher. The neutral gas is depleted at the center of the discharge, in agreement with experimental observations, and it is accumulated at the side of the cylinder where neutrals recombines. The deposition of RF power occurs

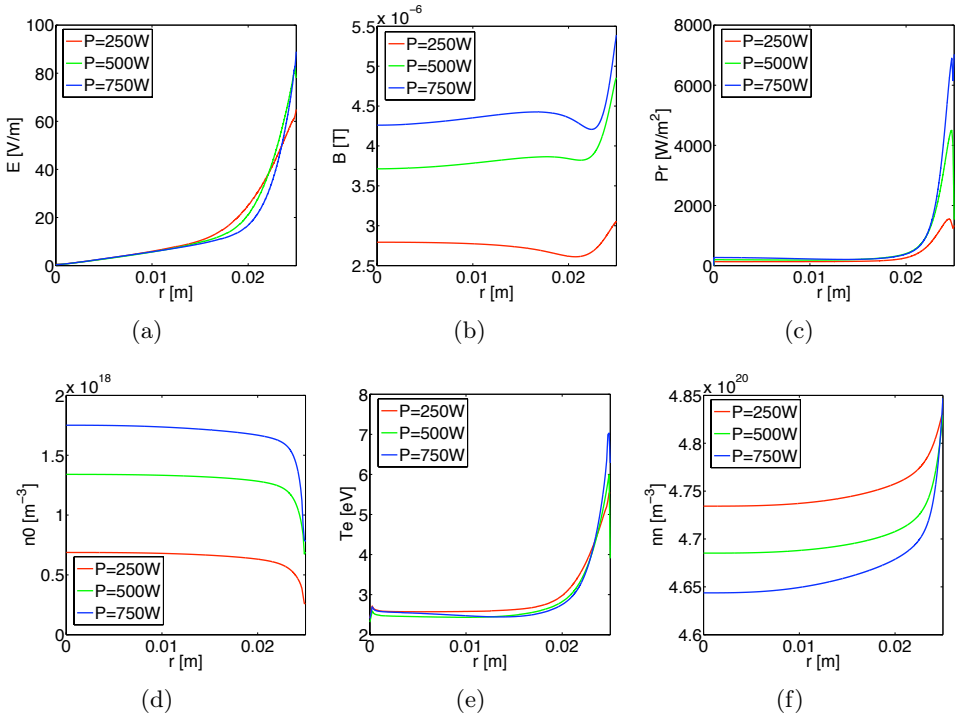

Figure 3.3: Radial profiles at equilibrium of a magnetized positive column of Argon plasma sustained by an $m = 0$ RF antenna. Gas pressure before the discharge $p_n = 18$ mTorr, antenna frequency 13.56 MHz, axial magneto-static field 0.02 T. (a) module of the RF electric field, (b) module of the RF magnetic field, (c) deposited RF power, (d) plasma density, (e) electron temperature, (f) density of the neutral gas.

mainly at the edge of the plasma cylinder, where the TG slow mode is rapidly damped by collisional processes. The power deposition calculations allowed the identification of most important physical processes concurring to the damping of the RF wave. It has been found that in this sources the damping of the electromagnetic wave into the plasma occurs

by collisional processes of electrons with charged species, and with neutrals. A smaller contribution also comes from the Landau damping of the RF wave due to wave-particle interaction, accounted by means of the Z plasma dispersion function [47] into the dielectric tensor. The Landau term is usually negligible for cold plasmas at electron temperatures of few electronvolts, whereas it becomes relevant only after that the electron temperature is increased (hot case). In Argon discharges, and all high-Z gases, most of the RF power is used to counteract the inelastic losses. This condition holds until the atom is completely ionized (4.426 keV for Ar^{+18}). At a given pressure, an increase of RF power involves a small increase of the electron temperature, since the power is mostly expended in the generation of new plasma particles, with a resulting increase of plasma density.

3.4 Conclusions

We have presented WAVEQM code, and numerical calculations of the equilibrium conditions of a magnetized plasma cylinder heated by means of a RF antenna.
The method allows the evaluation of all the relevant quantities commonly measured for the characterization of a plasma discharge: the value of the oscillating electric and magnetic fields, the profiles of plasma density, power deposition, electron temperature and neutral density. In order to evaluate the equilibrium conditions, two coupled problems have been iteratively solved up to the convergence on the aforementioned profiles, (1) the solution of the plasma-wave coupling, and (2) the solution of the macroscopic transport of charged and neutral species.
For the solution of the first problem, the electromagnetic fields have been solved using the already validated and presented code SPIREs. The solution of plasma and neutral profiles (problem 2) has been done using a theory recently proposed for the evaluation of the equilibrium conditions of plasma cylinders of finite-length, and implemented in the EQM code [51].
We have shown an example of numerical calculations after the convergence between the two problems for different RF power inputs. Most notably, the convergence criteria has been satisfied in just a few iterations.
The method allowed the evaluation of absolute values of plasma density and electron temperature, quantities that usually have to be measured from the particular experiment. Additionally, the method identified important physical processes occuring in the damping of the electromagnetic waves propagating inside a helicon plasma source, recognizing in the damping of the slow mode wave by means of collisional processes the responsible of edge peaked power deposition profiles. Moreover, the method recognized that an increase in the input RF power leads to an increase of plasma density, while the neutral gas is depleted at the center of the discharge, and the electron temperature remains approximately the same, as expected by experimental results. WAVEQM is thus relevant for a number of applications, ranging from semiconductor processing to RF plasma thrusters for spacecrafts. Satisfaction of convergence criteria is not computationally demanding, suggesting the use of this approach as an efficient numerical tool for preliminary design and optimization of magnetized plasma sources.
The aforementioned properties make the presented approach a valuable investigation tool

for the analysis of coupled electromagnetic/fluid phenomena in magnetized plasma sources (e.g. radial profiles at equilibrium for different RF input power), and a support in the comprehension of plasma source experiments.

Chapter 4

PARTYWAVE: A Hybrid Time-Domain Frequency-Domain PIC code for plasma cylinders

4.1 Introduction

We present PARTYWAVE (PARTicle code hYbrid coupled to electromagnetic WAVE solver), an iterative method based upon two codes working in a hybrid time-frequency loop; the former code called PARTicle code (PART) is a Time-Domain (TD) 3D Particle-In-Cell (PIC) code, while the latter is a Frequency-Domain (FD) electromagnetic solver, named SPIREs and previously presented. This method solves Maxwell wave equations and plasma current density equation for full wave fields by means of an iterative approach, which assures convergence on electromagnetic fields through a multidimensional Broyden scheme applied to plasma current density components.
The PIC code is meant to provide the kinetic plasma response. In particular, it follows in a uniform and structured cylindrical mesh and in time domain charged particle orbits confined by a magneto-static field, and forced by RF electromagnetic fields. Volume-Weighting Cloud-In-Cell (AW-CIC) model has been used to gather charge and current density informations on the mesh nodes in order to achieve a self-consistent particle simulation, and to get the current term, necessary to force the wave propagation. The current density is sampled in time and on each node of the 3D structured mesh, then it is partially Fourier transformed in time and along the azimuthal and axial directions. The Fourier transform provides a radial depending plasma current density to be used along with the antenna current as forcing terms for the wave solution. In order to take into account an additional confinement effect due to a radial electrostatic field, arising from different particles gyroradius, Poisson equation has been solved along the radial direction.
SPIREs solves for the frequency-domain wave propagation in vacuum forced by the antenna and plasma current densities. Unlike the full wave approach implemented in SPIREs, we want to directly calculate the plasma current density with a PIC code in order to take into account kinetic effects such as: finite gyroradius effects, finite temperaure effects, non-Maxwellian particle distributions, resonant particle orbits and nonlocal conductivity.

4.2 PART code

PART is a three dimensional electromagnetic PIC code, as described into detail by Birdsall and Langdon [54]. The PIC method couples the kinetic description of charged particles (i.e. plasma) with a grid based representation of the electric field. The continuous domain is a finite length cylinder; it has been discretized into a volumetric structured mesh by defining a spatial grid of nodes, allowing a fast and easy particles tracking inside the simulation domain. The problem is inherently cylindrical so cylindrical coordinates will be used.
Since the number of real plasma particles is extremely large, the PIC method introduces the concept of *macro particle* or *computational particle*, which is a collection of actual particles whose positions are close enough to feel the same electromagnetic force; the number of physical particles contained in each computational particle is called *particle weight* (p_w). In a PIC code charged particles are subjected to the Lorentz force, acting as an external force; the dynamic of a computational particle can be thought as the motion of a group of p_w-charged particles subjected to the same electromagnetic force, and so its dynamic is governed by the single particle parameters. From now on, the term *particle* will be used to describe the *computational particle*.
The external fields acting on the particles are made up of two different contributions: (i) the RF fields scattered by the antenna in vacuum (computed by SPIREs), and (ii) the self-consistent irrotational electric field due to the charged particles distribution.

4.2.1 Particle loading

First and foremost we need to assign suitable initial conditions to the particles at the beginning of the simulation, meaning that each particle i needs to be placed in the six-dimensional space $(\boldsymbol{v}, \boldsymbol{x})_i$ at $t = 0$. The placement involves starting with a prescribed density in space $n_0(\boldsymbol{x})$ and in velocity $f_0(\boldsymbol{v})$, and generating the corrisponding particle position and velocity $(\boldsymbol{v}, \boldsymbol{x})$.
The particles should have a uniform density distribution and a Maxwellian speed distribution, which can be created by means of a random number generator giving a random number for each dimension of the six-dimensional space and for each particle; unfortunately, random generators are not so random in computer simulations. This problem is partially solved by Quasi-Random numbers generators, which are deterministic sequences for numbers which mantain a low discrepancy[1]. Hammersley and Halton sequences are the most used sequences for Quasi-random numbers [55]. The Hammersley sequence provides better performances in terms of discrepancy but it is dependant on the total number of particles (i.e. the numbers to generate), so we leaned towards the Halton one. The Halton sequence uses a different prime number base for each sequence of random numbers; this means that in our case - the six-dimensional case - we should consider six different prime bases to generate random numbers for each dimension.
However, correlation problems have been reported between Halton numbers from higher dimensions, and the scrambled version of Halton sequence [56] has been implemented in order to mitigate this issue.
After the generation of the uniform six-dimensional space by means of the scrambled Halton

[1] Low discrepancy means that we are close to uniformity.

sequence, the last three dimensions have been remapped into the cylindrical coordinate system in order to initialize particle positions. In particular, the radial extension of the cylinder comes with the simulated plasma discharge radius, while the axial extension depends upon the simulated axial mode number (k_z). The last condition allows an axial periodicity that is necessary to cope with SPIREs spectral representation. The particles fill uniformly the cylindrical volume as showed in Fig. 4.1.

In order to load a Maxwellian velocity distribution, the uniform numbers from the first three

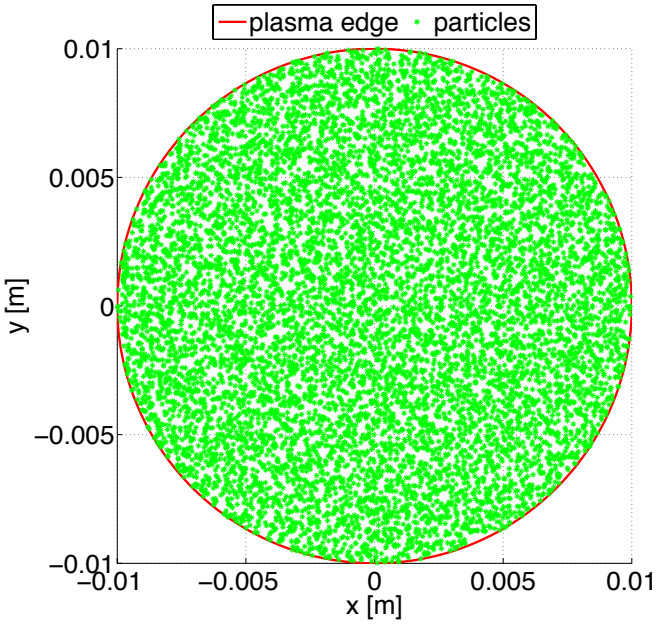

Figure 4.1: Initial particle positions in a (r, θ)-plane section a the plasma cylinder of 0.02 m diameter.

dimension of the Halton sequence have been processed by a Gaussian number generator, then normalized on the root mean square of the total velocity (in three dimensions):

$$v_{th,\alpha} = \sqrt{\langle v^2 \rangle} = \sqrt{\frac{3kT_\alpha}{m_\alpha}} \tag{4.1}$$

where k is the Boltzman constant, T_α and m_α are the temperature and the mass of the α charged species considered. Loading verifications have been reported in Figs. 4.2 and 4.3. Consider that if an electron exited the domain radially, it would be considered lost; if it was an ion, an ion-electron pair would be loaded with a uniform density distribution and a Maxwellian speed distribution, because we assumed a plasma source rate to be the same as ions loss rate. If a particle exited the domain axially, it would be injected on the axial opposite side with the same velocity, in order to achieve the aforementioned axial periodicity.

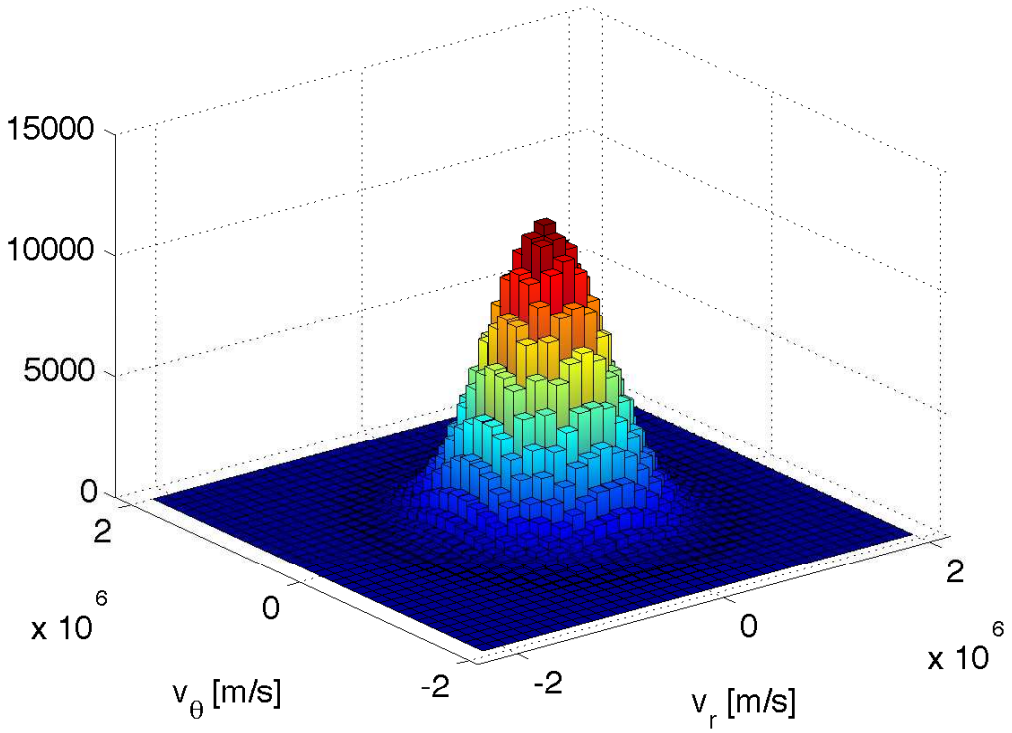

Figure 4.2: Initial distribution for the electrons velocity vector in the (v_r, v_θ) space after the loading of a $T = 3$ eV plasma.

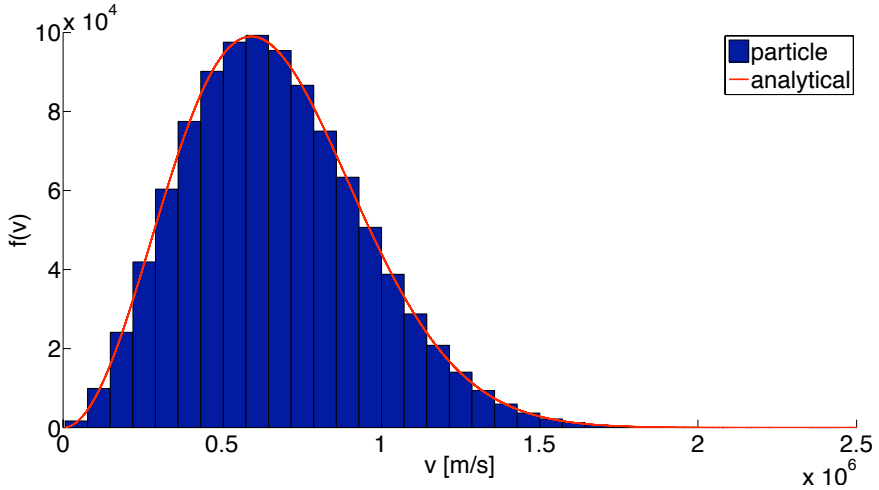

Figure 4.3: Initial distribution for the electrons speed after the loading of a $T = 3$ eV plasma. The red curve is a Maxwellian speed distribution for a $T = 3$ eV electron species.

4.2.2 Integration of the equation of motion

The particles' motion is governed by Newton-Lorentz equation:

$$m\frac{d^2\boldsymbol{x}}{dt^2} = q\left(\boldsymbol{E} + \boldsymbol{v} \times \boldsymbol{B}\right) \tag{4.2}$$

where $\boldsymbol{E}$ is the electric field, $\boldsymbol{B}$ is the magnetic field; $\boldsymbol{x}$, and $\boldsymbol{v}$ are the particle position and velocity, respectively. The electric and magnetic fields are to be calculated at the particle position; hence, using a spatial grid, we have to interpolate $\boldsymbol{E}$ and $\boldsymbol{B}$ from the grid to the particle. Note that the field interpolation is related to the way we compute particle quantities (e.g. charge density) on the grid points [54], and it is to be treated carefully in order to avoid nonphysical effects; this aspect will be addressed in the next paragraph.
Eq. 4.2 is commonly integrated using the second-order accurate centered difference scheme, often referred as the *leapfrog sheme* [54]; among different techniques, it is stable and time-reversible, which is important because it guarantees conservation of energy that can be essential in situations where we are interested in long-term small changes in the properties of a nearly periodic orbit. Moreover the leapfrog scheme has the additional merits of requiring few operations and minimal storage, making it necessary for many particles simulations [57]. Particle position and velocity values are advanced sequentially in time, starting from initial conditions, with the temporal staggered scheme shown in Fig. 4.4, and the computer will advance both $\boldsymbol{v}$ and $\boldsymbol{x}$ even though velocities are known at the half time steps while the positions are known at the full time steps. In our case the physical problem is inherently

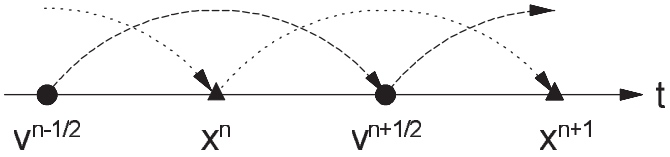

Figure 4.4: Schematic of the leapfrog scheme.

cylindrical, and the particle's positions and velocities are stored in cylindrical coordinates. At each time step for each particle $\cos\theta$ and $\sin\theta$ are stored, in addition to their radial and axial positions; this approach allows leapfrog methods used in cartesian coordinates to be extended to cylindrical geometries, avoiding singularities that can be found if pushing particle velocities and positions in cylindrical coordinates. However, in a usual leapfrog method, the velocities are known at the half time steps whereas the positions at the full time steps; this is a problem since $\cos\theta$ and $\sin\theta$ are used to transform the velocities from cylindrical to cartesian coordinates and they are known at the full time steps while the velocities are known at the half time steps. Therefore, we decided to use the *Syncopated Leapfrog* [58] that preserves second order accuracy (in both the push and the coordinate transformations), while requiring only a single field interpolation for each push. Given $\boldsymbol{x}^n_{cyl}$

and $\boldsymbol{v}_{cyl}^{n}$, $\boldsymbol{x}_{cyl}^{n+1}$ and $\boldsymbol{v}_{cyl}^{n+1}$ are calculated in the following manner:

$$\boldsymbol{v}_{car}^{n} = F\left(\boldsymbol{v}_{car}^{n}, \sin\theta^{n}, \cos\theta^{n}\right);\ \boldsymbol{x}_{car}^{n} = F\left(\boldsymbol{x}_{car}^{n}, \sin\theta^{n}, \cos\theta^{n}\right) \tag{4.3}$$

$$\boldsymbol{x}_{car}^{n+1/2} = \boldsymbol{x}_{car}^{n} + 1/2\Delta t \boldsymbol{v}_{car}^{n} \tag{4.4}$$

$$\boldsymbol{x}_{cyl}^{n+1/2} = G\left(\boldsymbol{x}_{car}^{n+1/2}\ , \sin\theta^{n+1/2}, \cos\theta^{n+1/2}\right) \tag{4.5}$$

$$\boldsymbol{E}_{cyl}^{n+1/2} = I_E\left(\boldsymbol{x}_{cyl}^{n+1/2}\right),\ \boldsymbol{B}_{cyl}^{n+1/2} = I_B\left(\boldsymbol{x}_{cyl}^{n+1/2}\right) \tag{4.6}$$

$$\boldsymbol{E}_{car}^{n+1/2} = F\left(\boldsymbol{E}_{cyl}^{n+1/2}, \sin\theta^{n+1/2}, \cos\theta^{n+1/2}\right) \tag{4.7}$$

$$\boldsymbol{B}_{car}^{n+1/2} = F\left(\boldsymbol{B}_{cyl}^{n+1/2}, \sin\theta^{n+1/2}, \cos\theta^{n+1/2}\right) \tag{4.8}$$

$$\boldsymbol{v}_{car}^{n+1/2} = \boldsymbol{v}_{car}^{n} + \frac{q\Delta t}{2m}\boldsymbol{E}_{car}^{n+1/2} \tag{4.9}$$

$$\boldsymbol{v}_{car}^{n+1/2'} = \boldsymbol{v}_{car}^{n+1/2} + \boldsymbol{v}_{car}^{n+1/2,Boris} \times \frac{q\Delta t}{2m}\boldsymbol{B}_{car}^{n+1/2} \tag{4.10}$$

$$\boldsymbol{v}_{car}^{n+1} = \boldsymbol{v}_{car}^{n+1/2'} + \frac{q\Delta t}{2m}\boldsymbol{E}_{car}^{n+1/2} \tag{4.11}$$

$$\boldsymbol{x}_{car}^{n+1} = \boldsymbol{x}_{car}^{n+1/2} + 1/2\Delta t \boldsymbol{v}_{car}^{n+1} \tag{4.12}$$

$$\boldsymbol{x}_{cyl}^{n+1} = G\left(\boldsymbol{x}_{car}^{n+1}, \sin\theta^{n+1}, \cos\theta^{n+1}\right);\ \boldsymbol{v}_{cyl}^{n+1} = G\left(\boldsymbol{v}_{car}^{n+1}, \sin\theta^{n+1}, \cos\theta^{n+1}\right) \tag{4.13}$$

Here F and G are the forward and reverse coordinate transformations and I_E and I_B represent the cylindrical interpolation scheme; the velocity $\boldsymbol{v}_{car}^{n+1/2,Boris}$ referes to the convenient rotation in vector form described by Boris [59]. When particles have been advanced in time, their final positions are checked against domain boundaries.

4.2.3 Fields and particle weighting

After the particles have been advanced in time, their motion, which reflects a current and charge densities, needs to be apportioned to the simulation grid. This provides the means by which the EM fields are affected by the motion of the free charges in the system.
It is necessary to accumulate all source terms (i.e charge and current densities) on the discrete grid points from the continuous particle positions and to calculate the force at the particle from the fields on the grid points; these calculations are called *weighting*, which implies interpolation among the grid points nearest to the particle position, and it is desirable to use the same weighting in both density and force calculations in order to avoid nonphysical self-forces.
In three dimensions, there are eight weights associated with the eight nodes (corners) of the right-hexahedral cell, as shown in Fig. 4.5(a). These weights have several important properties: (i) their sum is always one, (ii) as the particle approaches any one of the eight grid nodes, the weight associated with that node approaches one. The methods to evaluate these weights include nearest grid point, linear, quadratic and so on [54], [60]. The choice of the method for this allocation is always a trade-off between the factors of accuracy, numerical discretization noise, and computational efficiency [54]. The method employed in PART is the cloud-in-cell scheme [60], and the charge and current from a particle is distributed over the grid points in the cell where the particle is contained.

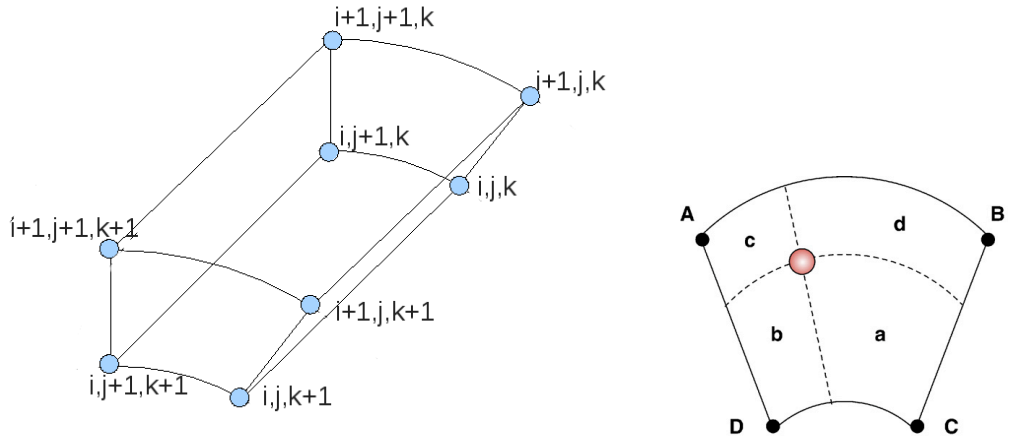

(a) (b)

Figure 4.5: Schematic of an element of the structured cylindrical mesh. (a) 3D schematic where the three values (i, j, k) specify the indexes of the considered mesh node along the radial, azimuthal and axial directions, respectively. (b) 2D schematic illustrating the weighting scheme; weights are assigned to the grid points **A-D** according to the areas **a-d**

As far as charge and current densities are concerned, a volume weighting method is used to determine what fraction of a particle is apportioned to a given grid point, as illustrated in Fig. 4.5(b). The picture shows a 2D area weighting for ease of visualization, but it can be easily extended to 3D by means of extrusion of the cartoon. In this scheme, the position of the points **A-D** is determined, then the areas **a-d** are evaluated; considering a particle of charge q_p, the charge assigned to the grid node **A** is given by the expression:

$$q_{p,A} = q_p \frac{a}{a+b+c+d} \tag{4.14}$$

and the same procedure is used for grid nodes **B**, **C** and **D**. In the 3D case, when the particle charge has been weighted to the surrounding eight nodes, the charge density on each node is computed as the ratio between the weighted charge of the node considered and the volume of the cell centered on the same node. The same can be inferred about the current density weighting. In cylindrical coordinates, systematic errors occur in weighting charge and current densities on the axis and at the outer edge [61],[62], leading to errors in the electromagnetic forces evaluated at these points. As suggested in [63] and [64], we used a general method for computing charge and current density source terms for Maxwell's wave equations from particles weighted to the structured cylindrical mesh; this method applies the same weighting scheme to both the particle and the volume element in order to obtain a density which eliminates the systematic errors in cylindrical coordinates. That is

$$n_{i,j,k} = \frac{\int w(r,\theta,z)\, W_{i,j,k}(r,\theta,z)\, dV}{\int W_{i,j,k}(r,\theta,z)\, dV} \tag{4.15}$$

where $W(r,\theta,z)_{i,j,k}$ is the weighting scheme which weights particles to the node identified by indexes (i, j, k), and $w(r,\theta,z)$ is the particle quantity (either charge or current) to

be weighted. Note that this method computes the exact density quantities in the limit $N/C \gg 1$, where N is the number of particles and C is the number of cells, as pictured in Fig. 4.6, where a radially uniform $J_{p,z} = 0.0799978$ A/m^2 is expected for a plasma cylinder of radius $r_a = 0.05$ m.

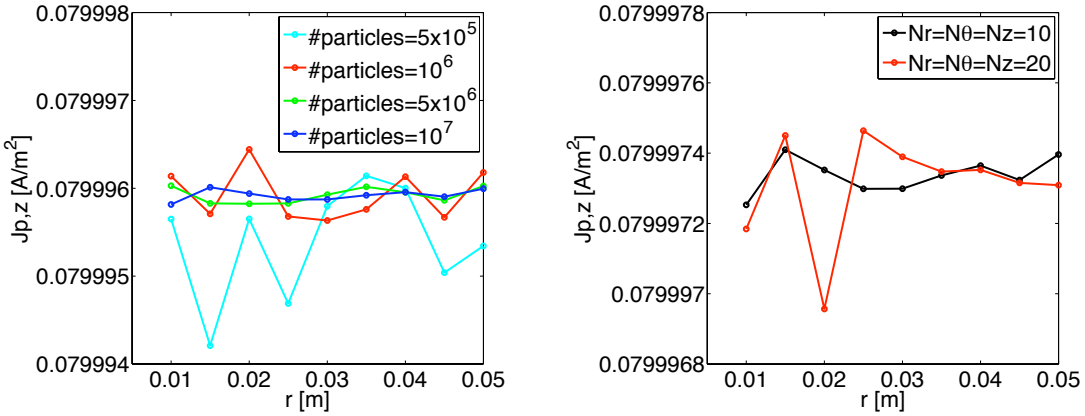

(a) (b)

Figure 4.6: Plasma current density weighting in a cylindrical source of radius $r_a = 0.05$ m for a plasma with uniform density $n_0 = 5 \cdot 10^{17}$ m^{-3} where the expected theoretical plasma current density is $J_{p,z} = 0.0799978$ A/m^2. (a) Radial density profile for different particles in the simulation and with a uniform cylindrical mesh, $Nr = N\theta = Nz = 10$ nodes along the radial, azimuthal, and axial directions. (b) Different noise levels for a simulation with 10^7 particles and two different uniform cylindrical meshes.

4.2.4 Poisson solver

In the case of Argon gas plasma discharge with a low level of axial confinement magnetostatic field (e.g. in the range of 0.01 T) along with small radius plasma sources (e.g $r_a \leq 0.05$ m), the ion gyroradius is much higher than the electron one leading to ion losses to the outer edge; the decrease in the ion density approaching the plasma edge builds up a radial electrostatic field that could influence the confinement of charged particles. In order to take into account an additional confinement effect due to a radial electrostatic field, arising from different particles gyroradius, Poisson equation has been solved along the radial direction, using the approach described in [54].
As said above, the weighting of the radial electrostatic field from the mesh to the particle position will be evaluated in the same way the charge density has been weighted to the mesh; this is neccessary in order to avoid nonphysical self-forces due to different weighting schemes used respectively for the accumulation of forcing terms in Poisson equation, and for the evaluation of the electrostatic field acting on the particles. Note that the radial electrostatic field evaluated by means of the approach described in [54] provides the field values halfway the grid points; in order to overcome this issue, a flux weighted average has been used:

$$E_{r,i} = \frac{r_{i-1/2}E_{r,i-1/2} + r_{i+1/2}E_{r,i+1/2}}{2r_i} \tag{4.16}$$

where i is the radial index of the node considered. We verified the algorithm against analytical solutions; we imposed a charge density in cylindrical shells, uniform in the azimuthal (θ) and axial (z) directions, and we evaluated the electrostatic radial field both analytically and numerically by means of PART code. Fig. 4.7 shows three differrent charge density profiles along the radial direction and the derived electrostatic fields that agree with a percent error less than $< 1\%$.

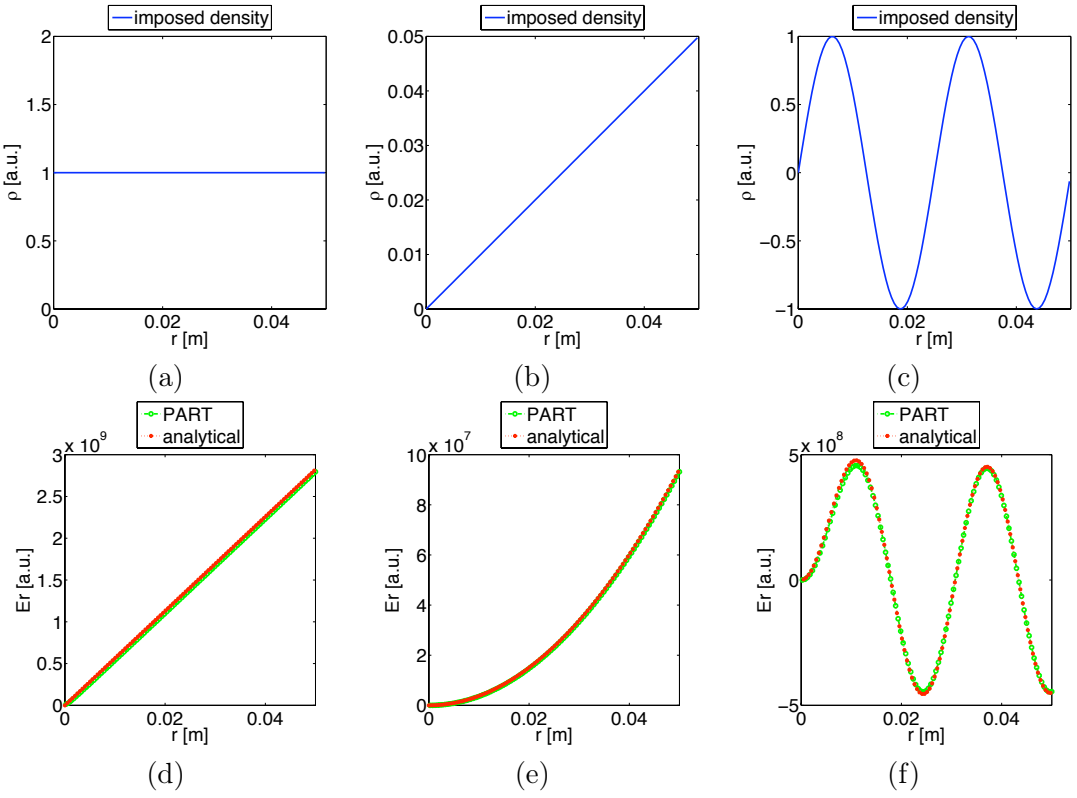

Figure 4.7: Electrostatic field along the radial direction for three charge density distribution along the radial direction. (a) constant, (b) linear and (c) sinusoidal charge density profiles along the radial direction. Electrostatic field along the radial direction for the (d) constant, (e) linear and (f) sinusoidal charge density profiles.

4.2.5 Current density

When particles have been advanced in time, their current density has been weighted on the surrounding grid nodes of the cell they are in, using the weighting scheme described above. At the end of the simulation, a time history of the current density will be available for each grid node and it will be Fourier transformed so that SPIREs can use it as a source term in Maxwell wave equations. Time evolution of particle motion is a multiple of the RF wave period simulated, while the time step depends on plasma frequencies [54]. The number of azimuthal (N_θ), and axial (N_z) nodes have to be chosen so that the simulation modes m

and k_z are correctly sampled according to the Nyquist-Shannon sampling theorem. For sake of clarity, SPIREs solves electromagnetic propagation in frequency domain, and it exploits a mode representation of wave quantities along the azimuthal (θ) and axial (z) directions; therefore, current density data will be processed by a 1D time Fourier transform augmented by a 2D spatial (azimuthal and axial) Fourier transform, giving:

$$\boldsymbol{J_p}\left(r,\theta,z,t\right) \rightarrow \boldsymbol{J_p}\left(r,m,k_z,\omega\right) \tag{4.17}$$

where m and k_z are the azimuthal and axial mode numbers, respectively; ω is the antenna working frequency.
The Fourier transform calculation has been validated in the cold plasma limit, where the plasma response can be represented by means of Stix dielectric tensor $\boldsymbol{\epsilon}$; specifically, a uniform noncollisional plasma with no thermal velocity, confined by a uniform magnetostatic field along the axial direction ($\boldsymbol{B_0} = B_0\hat{\boldsymbol{z}} = const$) has been considered, and testing RF electromagnetic fields are provided. The plasma response for the given testing fields, mode numbers (m, k_z), and for the antenna working frequency has been evaluated in two different ways: by means of the Stix plasma dielectric tensor ($\boldsymbol{J_p} = \boldsymbol{\epsilon E}$), and by the PART code Fourier transformed current density. Fig. 4.8 shows that the kinetic response of plasma follows correctly the radial component of the plasma current density evaluated by means of the Stix dielectric tensor, inside a plasma source of radius $r_a = 0.05$ m, with a percent error less than $< 5\%$ for the radial profile.
Note that there is a region where no plasma current density is flowing (0.05 m $< r < 0.1$ m), which corresponds to the vacuum region defined by $r_b < r < r_c$ in Fig. 2.1; as explained above, this is a necessary region for the SPIREs code to solve for the electromagnetic waves.

4.2.6 Numerical solution

PART code is a 3D PIC code in cylindrical coordinates written in C, because performance is a key concern. Memory management and execution speeds have been optimized by means of suitable data structures, pointers arithmetics, modular coding, and dynamic memory allocation. The current density has been sampled in time domain and on each node of the cylindrical mesh; afterwards, it has been Fourier transformed in the frequency domain, and along the azimuthal and axial directions. We used the Fastest Fourier Transform in the West (FFTW) [65] library because it is generally the fastest FFT implementation available, it is portable, it is based on plans that choose the best FFT algorithm for the given problem, and it is not limited to power-of-two transform sizes. Fig. 4.9 shows the workflow of the code, which is made up of the following sections:

1. **Input**: all input quantities related to the plasma species, geometry, modes, 3D structured cylindrical mesh, and simulation parameters are specified in the input file.

2. **Loading**: the input file is read by the parser, and memory is then allocated. Several parameters necessary to run the simulation are defined (e.g. plasma frequencies, timestep, simulation time, particle weight, thermal velocity). Particles state vector (i.e. position and velocity) is loaded in order to have a uniform density distribution and a Maxwellian speed distribution.

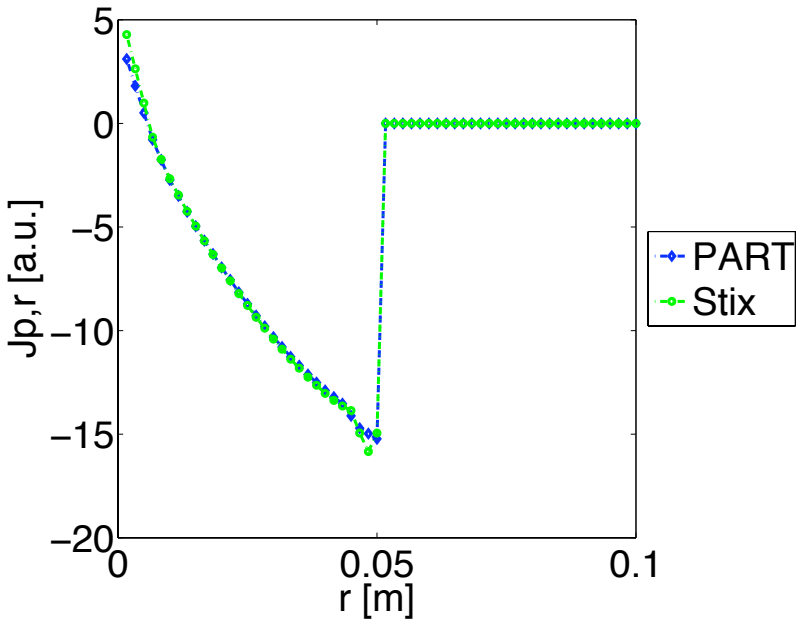

Figure 4.8: Radial component of the plasma current density ($J_{p,r}$) along the radial direction both in the plasma and in the vacuum regions. The numerical kinetic plasma response given by PART code and analytically by Stix dielectric plasma tensor are overlapped with a percent error less than $< 5\%$.

3. **Time Loop**: Simulation time is a multiple of the RF wave period. The duration of each time loop depends on plasma frequencies. In each time loop the code interpolates RF fields coming from an external solver to particle positions, it advances particle positions and velocities, it checks domain boundaries, and it stores current densities on the 3D grid. Eventually charge is weighted to the grid nodes if the electrostatic field is evaluated.

4. **Output**: current density samples in time and space are processed by FFTW; results are written in formatted output files.

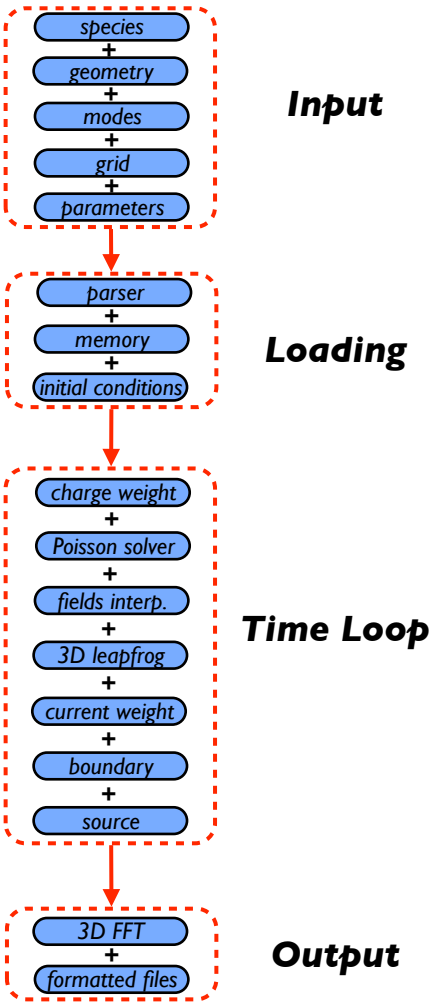

Figure 4.9: Numerical scheme implemented in PART.

4.3 PARTYWAVE

PARTYWAVE is made of two different codes, namely SPIREs and PART, coupled in a hybrid time-frequency loop. SPIREs solves Maxwell wave equations in vacuum for electromagnetic fields in frequency domain, forced by a given antenna current ($\boldsymbol{J_A}$) along with a plasma current ($\boldsymbol{J_p}$), if any. Fields ($\boldsymbol{E}, \boldsymbol{B}$) coming from SPIREs have been used to move charged particles in PART.
Recall that SPIREs features a spatial representation of wave quantities along the radial direction, and a Fourier representation along the azimuthal and axial directions; therefore, before moving particles, wave fields have to be restored in the spatial and time domain by anti-Fourier transforming. Plasma current densities, calculated by PART at each node of a 3D structured mesh of a cylindrical domain, need to be first Fourier transformed along the azimuthal and axial directions and in time; then the components related to the simulation modes (m, k_z) and frequency (ω) have to be extracted. PART provides plasma current density in SPIREs spectral domain and as function of the radial coordinate. It is worth noticing that in SPIREs and PART, the radial nodes are the same.
Unlike the full wave approach implemented in SPIREs, we want to directly calculate the plasma kinetic response by means of PART code in order to take into account kinetic effects such as: finite gyroradius effects, finite temperaure effects, non-Maxwellian particle distributions, resonant particle orbits and nonlocal conductivity.
In PARTYWAVE the output of one code is the input for the other one and viceversa, allowing us to state PARTYWAVE resolution as a nonlinear system of two coupled codes, solved by means of an iterative multidimensional Broyden scheme. The convergence scheme guarantees that the full wave solution has been reached.

4.3.1 Implicit coupling scheme

PARTYWAVE solves Maxwell wave equations and plasma kinetic response for full wave fields by means of an iterative approach, which assures convergence on electromagnetic fields through a multidimensional Broyden scheme applied to plasma current density vector. Specifically, the Broyden convergence scheme acts on the three cylindrical components (r, θ, z) of the plasma current density vector ($\boldsymbol{J_p}$) for each of the $\mathcal{N}$ radial nodes.
For sake of clarity, consider SPIREs and PART codes as two different functions named from now on as Σ and Φ, respectively. Code Σ takes input $\boldsymbol{J_p}$ and generates output $\boldsymbol{E}$ and $\boldsymbol{B}$, whereas code Φ takes input $\boldsymbol{E}$ and $\boldsymbol{B}$ and generates output $\boldsymbol{J_p}$. This problem can be stated as a system of nonlinear equations:

$$\begin{cases} (\boldsymbol{E}, \boldsymbol{B}) = \Sigma\left(\boldsymbol{J_p}\right) \\ \\ \boldsymbol{J_p} = \Phi\left(\boldsymbol{E}, \boldsymbol{B}\right) \end{cases} \tag{4.18}$$

The system is to be solved to get codes Σ and Φ in a self-consistent state, meaning that the full wave condition has been reached for electromagnetic fields. We iteratively solved

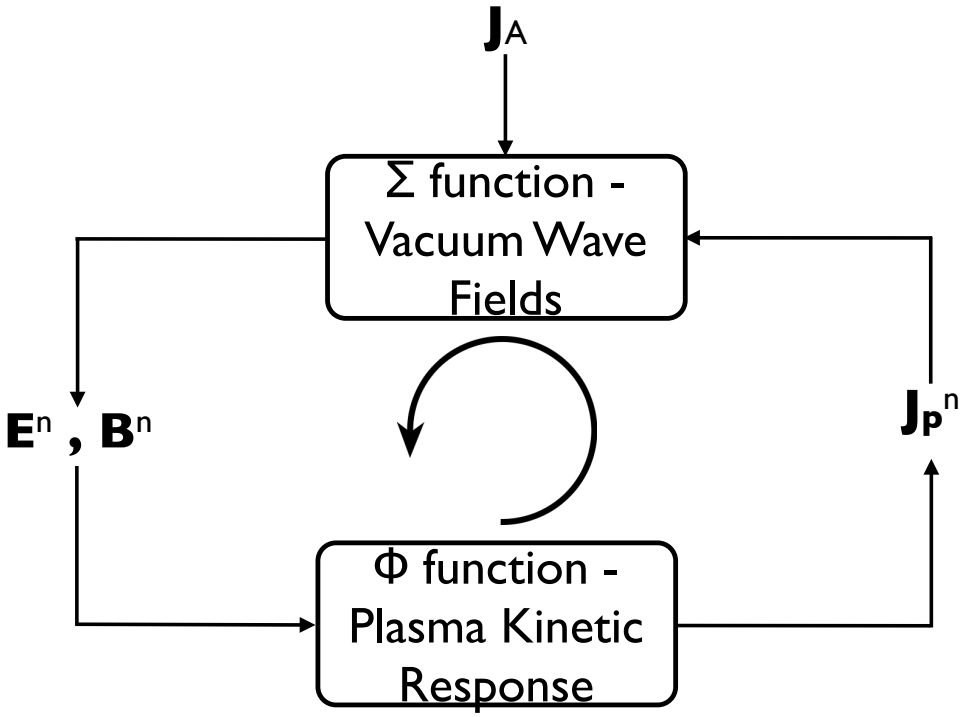

Figure 4.10: Coupling scheme implemented in PARTYWAVE.

the system by means of the Picard iteration:

$$\boldsymbol{\Psi}\left(\boldsymbol{J_p}^n\right) = \begin{cases} \left(\boldsymbol{E}^{n+1}, \boldsymbol{B}^{n+1}\right) = \Sigma\left(\boldsymbol{J_p}^n\right) \\ \\ \boldsymbol{J_p}^{n+1} = \Phi\left(\boldsymbol{E}^n, \boldsymbol{B}^n\right) \end{cases} \tag{4.19}$$

where $\boldsymbol{\Psi}$ is a vector function of the vector variable $\boldsymbol{J_p}$, and n is the iteration step with $n \in \mathbb{N}$ and $n \geq 1$. In order to force the convergence of the iterative method, we modified the Picard output $\boldsymbol{J_p}^{n+1}$ at the nth step (to be plugged in Eq. 4.19 at the next iteration) by minimizing the function

$$\boldsymbol{\Gamma}\left(\boldsymbol{J_p}\right) = \boldsymbol{J_p}^{n+1} - \boldsymbol{J_p} \tag{4.20}$$

thus obtaining the Picard modified $\boldsymbol{J_p}^{n+1*}$ to be used as input at the $(n+1)$th step. It is worth recalling that we deal with vector functions $\boldsymbol{J_p}$ of vector variables (r, θ, z) defined in $\mathbb{R}^3 \to \mathbb{R}^3$, and each variable has been defined for each of the $\mathcal{N}$ radial nodes the mesh is composed of. We adopted a $3\mathcal{N}$-dimensional Broyden method

$$\boldsymbol{J_p}^{n+1*} = \boldsymbol{J_p}^n - \boldsymbol{B}_n^{-1}\boldsymbol{\Gamma}\left(\boldsymbol{J_p}\right) \tag{4.21}$$

where $\boldsymbol{B}_n^{-1}$ is the inverse of the Broyden matrix at the nth iteration step. When $n = 1$ we use $\boldsymbol{B}_1^{-1} \equiv \boldsymbol{I}$ to bootstrap the method, where $\boldsymbol{I}$ is the identity matrix; when $n > 1$ we use the Sherman-Morrison formula:

$$\boldsymbol{B}_n^{-1} = \boldsymbol{B}_{n-1}^{-1} + \frac{(\boldsymbol{J_p}^n - \boldsymbol{J_p}^{n-1}) - \boldsymbol{B}_{n-1}^{-1}\left[\boldsymbol{\Gamma}(\boldsymbol{J_p}^n) - \boldsymbol{\Gamma}(\boldsymbol{J_p}^{n-1})\right]}{(\boldsymbol{J_p^n} - \boldsymbol{J_p}^{n-1})^T \boldsymbol{B}_{n-1}^{-1}\left[\boldsymbol{\Gamma}(\boldsymbol{J_p}^n) - \boldsymbol{\Gamma}(\boldsymbol{J_p}^{n-1})\right]} \left[(\boldsymbol{J_p}^n - \boldsymbol{J_p}^{n-1})^T \boldsymbol{B}_{n-1}^{-1}\right] \tag{4.22}$$

As far as the convergence criteria is concerned, we considered the Frobenius norm $\|\Gamma\left(\boldsymbol{J_p}\right)\|_F < \varepsilon$ at each node of the mesh, where ε is a prescribed tolerance.

4.3.2 Numerical accuracy of Picard iteration

In order to assess the numerical accuracy of the scheme proposed in Eq. 4.19 we considered a simplified version of PARTYWAVE, where the plasma response is provided by a Stix dielectric tensor; in this way, we can verify the numerical accuracy of the convergence method, and we can identify all the limitations affecting PARTYWAVE approach, avoiding all the numerical issues related to a PIC code simulating a plasma made of charged particles. Therefore, we can assess the stability and convergence capabilities of the numerical approach, avoiding the complexities related to a PIC code, and evaluating the plasma response by means of $\boldsymbol{J_p} = \boldsymbol{\sigma E}$, where electric vacuum fields $\boldsymbol{E}$ have been computed by SPIREs. Specifically, in PARTYWAVE Φ has been replaced by a cold Stix plasma conductivity tensor $\boldsymbol{\sigma}$, which evaluates the plasma current density when vacuum wave fields are provided by Σ-function. At the first iteration the antenna current $\boldsymbol{J_A}$ is given, Σ-function evaluates vacuum fields, used in turn to evaluate the plasma current density $\boldsymbol{J_p}$ through Φ-function; at next iterations, Σ-function evaluates vacuum fields using as input both $\boldsymbol{J_A}$ and $\boldsymbol{J_p}$. At each step of the iterative method the antenna current $\boldsymbol{J_A}$ is always the same.
The following non-collisional plasma has been considered: $r_a = 0.05$ m, $r_b = r_a$, and $r_c = 2 \times r_a$, Argon plasma discharge with uniform density $n_0 = 10^{18}$ m^{-3}; axial magnetostatic field $B_0 = 0.035$ T, and forced by $I_0 = 1.0$ A single loop antenna working at $f = 13.56$ MHz and exciting $m = 0$ and $k_z = 15$ m^{-1} azimuthal and axial modes. We considered a non-collisional plasma so that plasma current vector components have either a real or an imaginary part making the fulfilment of the convergence criteria easier to be satisfied.
The numerical solution calculated by PARTYWAVE (running in the aforementioned simplified configuration) has been validated against SPIREs full wave solution. The goal is to get the full wave solution by means of two completely different approach: the former is SPIREs code, which provides the full wave reference solution to be reached by the latter - PARTYWAVE - by means of an iterative approach. Both solutions are provided for a radial mesh of 30 nodes, and PARTYWAVE satisfied convergence criteria in 91 iterations as showed in Fig. 4.11.

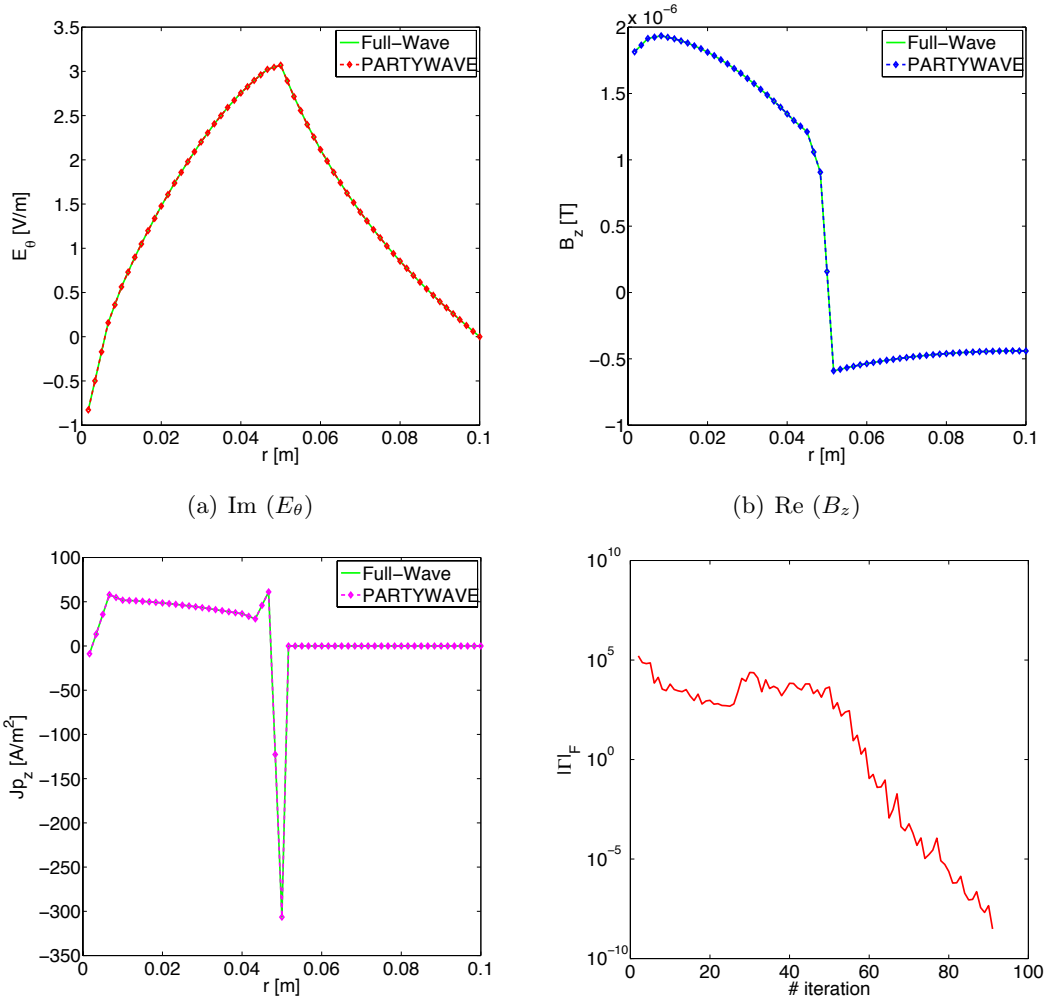

(a) Im (E_θ)

(b) Re (B_z)

(c) Re (Jp_z)

(d) Absolute value of Frobenius norm

Figure 4.11: Comparison between 30 radial nodes Full-Wave and PARTYWAVE solutions of field components (a) azimuthal Im(E_θ), (b) axial Re(B_z), (c) axial Re(Jp_z), and (d) absolute value of Frobenius norm, in a Argon plasma discharge with the following parameters: $r_a = r_b = 5.0 \cdot 10^{-2}$ m, $r_c = 1.0 \cdot 10^{-1}$ m, $f = 13.56 \cdot 10^6$ Hz, $n_0 = 10^{18}$ m^{-3}, $B_0 = 0.035$ T, $m = 0$, $k_z = 15.0$ m^{-1}, $I_0 = 1.0$ A. PARTYWAVE satisfied convergence criteria in 91 iterations.

In order to further verify convergence capabilities, we considered a stiffer test case, where Φ has been replaced by a cold Stix collisional plasma tensor. The plasma parameters and the radial mesh are the same as the previous case, but this time the plasma is collisional with a collisionality $\nu = 2\pi \cdot 10^7$ Hz. The key point is not the absolute value of collisionality, which is actually a typical value for an Argon plasma with the above parameters, but rather the real and imaginary components of the plasma current density introduced by the collisionality in the Stix plasma tensor. We expected PARTYWAVE to converge in more iterations.

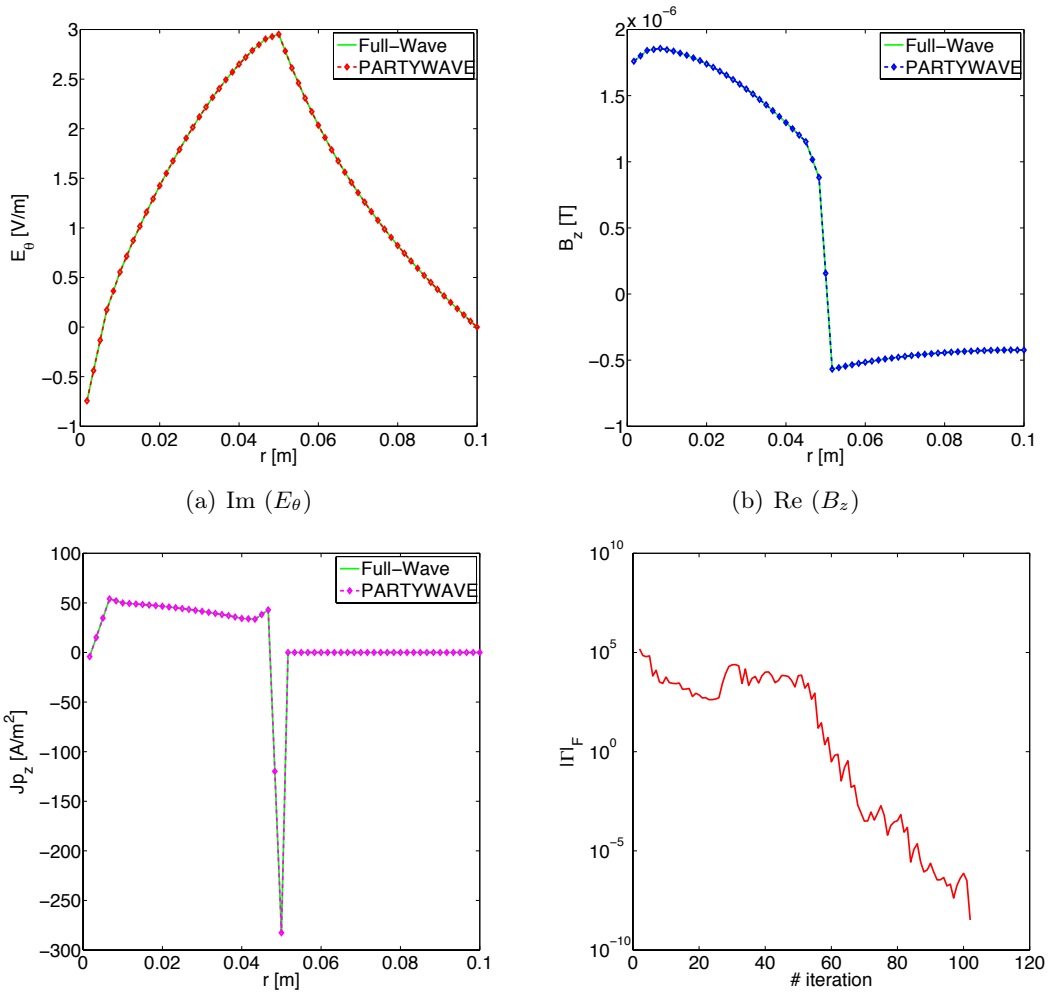

(a) Im (E_θ)

(b) Re (B_z)

(c) Re (Jp_z)

(d) Absolute value of Frobenius norm

Figure 4.12: Comparison between 30 radial nodes Full-Wave and PARTYWAVE solutions of field components (a) azimuthal Im(E_θ), (b) axial Re(B_z), (c) axial Re(Jp_z), and (d) absolute value of frobenius norm, in a Argon plasma discharge with the following parameters: $r_a = r_b = 5.0 \cdot 10^{-2}$ m, $r_c = 1.0 \cdot 10^{-1}$ m, $f = 13.56 \cdot 10^6$ Hz, $n_0 = 10^{18}$ m^{-3}, $B_0 = 0.035$ T, $\nu = 2\pi \cdot 10^7$ Hz, $m = 0$, $k_z = 15.0$ m^{-1}, $I_0 = 1.0$ A. PARTYWAVE satisfied convergence criteria in 102 iterations.

As showed in Figs. 4.11 and 4.12, the iterative solutions converge to the full wave reference solution; the good agreement between the two solutions is justified by a percent error less than $< 1\%$ for the electric field, magnetic field, and plasma current density radial profiles. Picard iteration converges linearly, as shown in Figs. 4.11(d) and 4.12(d).
We concluded the analysis considering the scalability of this numerical method for a higher number of radial nodes. The scaling with the radial nodes revealed to be particularly important in identifying limitations that could affect PARTYWAVE performance when PART takes care of the plasma kinetic response. As a matter of fact, in PARTYWAVE the solution provided by SPIREs is based upon a finite-difference scheme which requires a different number of discretization nodes depending on the wavelengths involved in the simulation considered. But the radial nodes in PART cannot increase in the same way they can do in SPIREs; otherwise too many particles would be necessary so that a statistical representability in each volume cell can be achieved, and to keep under control the noise related to particle simulation [54].
In Fig. 4.13 we considered both the simulation with a non-collisional and a collisional plasma for an increasing number of radial nodes ranging from 20 to 200 nodes. As expected, the simulations with a collisional plasma take more iterations to satisfy the convergence criteria, because plasma current densities have both a real and an imaginary part for each component unlike the non-collisional case.
Fig. 4.13 shows that the iterations at convergence increase as the radial nodes. This trend is due to the linear convergence of Picard iterations, and the utilization of the same number of radial nodes for Σ and Φ functions. Most notably, this behavior could destroy numerical accuracy, and could make PARTYWAVE computationally inefficient in a simulation where more than 10^3 nodes are necessary to sample correctly the electromagnetic wavelengths involved. These problems can be overcome (i) by employing a convergence scheme assuring a superlinear convergence, and (ii) by the use of two staggered radial grids; a finer one for SPIREs, and a coarser one for PART. These mitigation strategiesis out of the scope of this work.

4.3.3 Numerical accuracy on physical case

To benchmark PARTYWAVE we made it run with PART as the Φ-function, providing the plasma kinetic response, and compared its results against a full wave solution provided by SPIREs.
We considered a non-collisional cold plasma modeled by a Stix dielectric tensor, and that can be solved by SPIREs for the full wave fields and plasma current densities, and used as reference solutions. The same plasma can be simulated by PART once the Poisson solver is off. With reference to Fig. 2.1, we considered a cold ($Te = 3$ eV and $Ti = 0.01$ eV) non-collisional, cylindrically-shaped ($r_a = 0.05$ m, $r_b = r_a$ and $r_c = 2 \times r_a$) Argon plasma discharge with uniform density $n_0 = 10^{18}$ m^{-3}; charged particles are confined by an axial magneto-static field $B_0 = 0.035$ T, and forced by a single loop antenna working at $f = 13.56$ MHz, exciting $m = 0$ and $k_z = 50$ m^{-1} azimuthal and axial modes, respectively. After 57 iterations, PARTYWAVE solved for full wave fields and plasma current densities, as pictured in Fig. 4.14.
In PARTYWAVE the plasma response $\boldsymbol{J_p}$ has been provided by PART code, which does

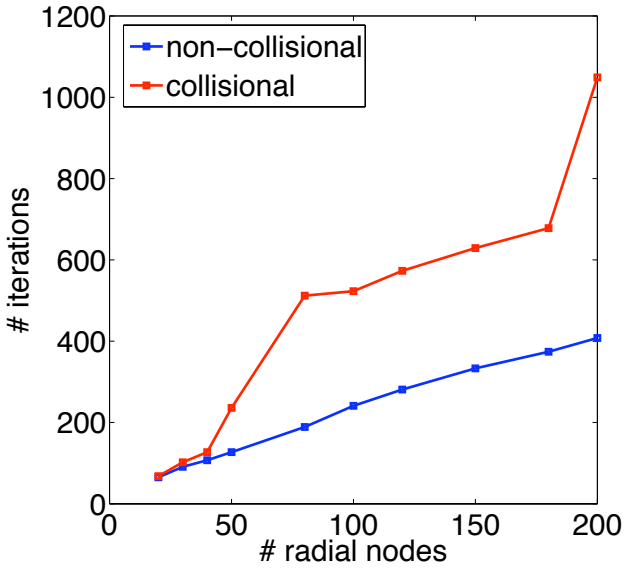

Figure 4.13: Scalability of PARTYWAVE convergence scheme for different radial nodes.

not include particle collisions at the moment. PART moves charged particles (i.e. electrons and ions), confined by a magneto-static field, and non interacting with each other (i.e. non-collisional plasma); therefore, we expected plasma current densities to have either real or imaginary components. However, plasma current density $\boldsymbol{J_p}$ comes from the 2D-space and 1D-time Fourier transform of the full kinetic particles response. The Fourier transform has been performed numerically by the FFTW library, which introduced numerical errors that leads to an unwanted real or imaginary nonphysical part in each plasma current component. If left unresolved, such issue could destroy the numerical accuracy of the method, making impossible to fulfill the convergence criteria. However, the unwanted part was at least one order of magnitude smaller than the other, so it was straightforward to rule it out by means of a direct comparison against the other one.
Results pictured in Fig. 4.14 show a good agreement between the reference and the iterative full wave solutions with a percent error less than $< 7\%$, where the highest error appears just in one radial node (see Fig. 4.14(d)) near an abrupt change in the radial profile of the axial component of the plasma current density.

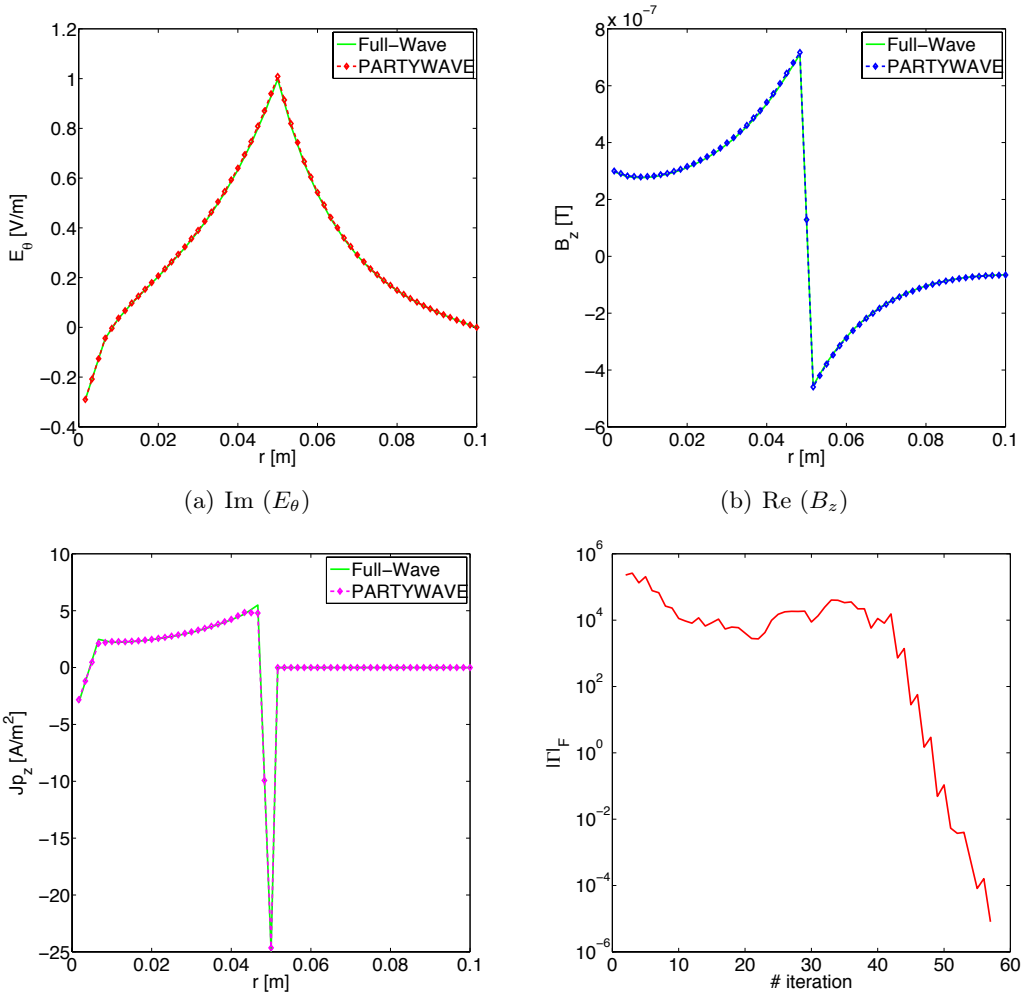

(a) Im (E_θ)

(b) Re (B_z)

(c) Re (Jp_z)

(d) Absolute value of Frobenius norm

Figure 4.14: Comparison between 30 radial nodes Full-Wave and PARTYWAVE solutions of field components (a) azimuthal Im(E_θ), (b) axial Re(B_z), (c) axial Re(Jp_z), and (d) absolute value of frobenius norm, in a plasma discharge with the following parameters: $r_a = r_b = 5.0 \cdot 10^{-2}$ m, $r_c = 1.0 \cdot 10^{-1}$ m, $f = 13.56 \cdot 10^6$ Hz, $n_0 = 10^{18}$ m^{-3}, $B_0 = 0.035$ T, $m = 0$, $k_z = 50.0$ m^{-1}, $I_0 = 1.0$ A. PARTYWAVE satisfied convergence criteria in 57 iterations.

4.4 Conclusions

PARTYWAVE, an iterative method based upon two codes working in a hybrid time-frequency loop, has been developed and validated to study the electromagnetic propagation and power deposition in cylindrically-shaped plasmas. PARTYWAVE is made of two different codes: SPIREs and PART. The former has already been presented and provides electromagnetic fields in frequency domain in a vacuum medium. The latter - PART - is a PIC code using vacuum fields to move charged particles, and collecting plasma current density ($\boldsymbol{J_p}$) on a stuctured 3D mesh as a function of time. Since SPIREs is in the frequency domain, and it makes use of a Fourier representation along the azimuthal and axial directions, vacuum fields have to be anti-Fourier transformed before moving particles, while the plasma kinetic response ($\boldsymbol{J_p}$) has to be Fourier transformed for the simulation frequency, azimuthal and axial modes.
PART features: (i) a AW-CIC model to gather charge and current density informations on the mesh nodes, (ii) a radial Poisson solver to take into account additional confinement effect due to different species gyroradii, and (iii) a syncopated-leapfrog [58] advancing scheme that preserves second order accuracy but being computationally cheap. Numerical accuracy of PART has been verified separately from PARTYWAVE. Specifically, initial particle loading has been verified in space and velocity for a uniform Argon plasma made up of two species (i.e. electrons, ions) with electron temperature $T_e = 3$ eV (see Figs. 4.1 and 4.3). The AW-CIC algorithm has been verified in the weighting of plasma current density, considering the effect of different mesh refinements, and different simulation particles (see Fig. 4.6). The Poisson solver has been validated against analytical solutions for imposed charged density profiles, with a percent error less than $< 1\%$ in the electrostatic fields (see Fig. 4.7). The Fourier transformation of the plasma current density has been validated against a reference test case, where RF testing fields are given and the plasma response has been modeled by Stix dielectric tensor, obtaining a good agreement between the two solutions with a percent error less than $< 5\%$ (see Fig. 4.8).
Once PART and SPIREs have been coupled, the problem has been stated as a nonlinear system (see Eq. 4.19), which we solved iteratively by means of a $3\mathcal{N}$-dimensional Broyden scheme on plasma current density components $(J_{pr}, J_{p\theta}, J_{pz})$ for each of the $\mathcal{N}$ radial nodes shared by SPIREs and PART. This approach solves for full wave fields and plasma current density, where the plasma kinetic response can be simulated in detail keeping into account finite gyroradius effects, finite temperature effects, and non-Maxwellian particle distributions.
PARTYWAVE has proved to converge linearly (see Figs. 4.11(d) and 4.12(d)). It has been validated against a full wave solution provided by SPIREs, where a good agreement has been found both for electromagnetic fields and for plasma current density curves, with a percent error less than $< 7\%$ (see Fig. 4.14). Results have been provided for 30 radial nodes.
The scalability of the method has been assessed for an increasing number of radial nodes ranging from 20 to 200 nodes, pointing out that (i) iterations at convergence increase as the number of radial nodes (see Fig. 4.13), and (ii) PARTYWAVE becomes computationally inefficient when more than 10^3 nodes are necessary to sample the electromagnetic wavelengths involved in the simulation.

Chapter 5

Method of Moments for Antenna design

5.1 Introduction

The interaction of electromagnetic waves with dielectric bodies have been extensively studied because of its importance to problems including propagation through rain or snow, scattering by and detection of airborne particulates, medical diagnostics and power absorption in biological bodies, coupling to missile with plasma plumes or dielectric-filled apertures, and performance of communication antennas in the presence of dielectric and magnetic inhomogeneities. In our case, we will consider a 3D arbitrarily-shaped Perfectly Electric Conductor (PEC) body surface - the antenna - facing an arbitrarily-shaped, inhomogeneous anisotropic body - the plasma - modeled by means of electrically-homogeneous tetrahedra. By using the equivalence principle, the 3D PEC antenna can be replaced by an equivalent surface current, and a Surface Electric Field Integral Equation (SEFIE) is derived by relating these surface currents to the total electric fields [66]. The plasma can be replaced by an equivalent volume polarization current, and a Volume Integral Equation (VIE) is derived by relating the plasma current to the total electric field. Then all the equivalent currents are assumed to radiate in free space, so that the free-space Green's function can be used. The system of equations made of the SEFIE and the VIE is coupled because the electric fields scattered by the plasma polarization currents influence the current distribution over the antenna, whereas the fields scattered by the antenna in turn influence the plasma polarization currents. This coupling will be taken into account by suited terms in the SEFIE and in the VIE, respectively: in the SEFIE there will be the electric field scattered by the plasma currents impinging on the antenna surface, while in the VIE there will be a current term due to the electric fields scattered by the antenna.
When solved numerically through the Method of Moments, the coupled system of equations reduces to a linear system, where the unkowns are the antenna surface and plasma volume currents; the forcing term is the voltage generator feeding the antenna. The system matrix $\boldsymbol{Z}$ can be decomposed into four rectangular matrix blocks which read:

$$\boldsymbol{Z} = \begin{bmatrix} \boldsymbol{Z}^{SS} & \boldsymbol{Z}^{SV} \\ \boldsymbol{Z}^{VS} & \boldsymbol{Z}^{VV} \end{bmatrix} \tag{5.1}$$

where the superscript S stands for SEFIE, while V for VIE contribution, respectively. Each matrix entries is related to a particular contribution of the SEFIE and VIE, namely:

1. the first matrix block - $\boldsymbol{Z}^{SS}$ - is related to the radiation problem of the PEC antenna in free space

2. the second matrix block - $\boldsymbol{Z}^{SV}$ - is one of the two coupling terms and it is related to the influence on the scattered electric fields by the plasma currents impinging on the antenna surface

3. the third matrix block - $\boldsymbol{Z}^{VS}$ - is the other coupling term and it is related to the influence of the electric fields scattered by the antenna on the volume plasma currents

4. the fourth matrix block - $\boldsymbol{Z}^{VV}$ - is related to the scattering problem of the volume plasma currents in free space

In this work the first matrix block $\boldsymbol{Z}^{SS}$ has been fully developed and validated; it can work as a standalone tool for a preliminary study and design of the antennas radiating electromagnetic fields in free space.

5.2 Electromagnetic scattering by surfaces of arbitrary shape

In all the codes considered so far, the antenna has been considered as a current distribution given a priori; however, in order to study, analyze and optimize antennas, we need to solve the actual scattering electromagnetic problem for the current distribution all over the antenna. This holds true whether we refer to the RF antenna that will be used to ionize and heat the plasma or to the antenna that will be used for communication.
As a matter of fact, we considered the antenna as a 3D conducting body radiating electromagnetic fields in a background homogeneous medium with ϵ and μ electric and magnetic properties, respectively; it is worth recalling that this is not true anymore, if the antenna is facing an ionized medium such as a plasma but this problem will not be addressed in the present model.
To solve radiation and scattering problems, it is often useful to formulate the problem in terms of an equivalent one that may be easier or more convenient to solve in the region of interest. These equivalents are often written in terms of surface currents that mathematically account for the presence of obstacles present in the original problem.
The surface equivalence theorem (or Huygen's Principle) states that every point on an advancing wavefront is itself a source of radiated waves; by this theorem, an actual radiating source can be replaced by a fictitious set of different but equivalent sources. These are currents, and are placed on an arbitrary closed surface enclosing the original sources [67]. By enforcing the appropriate boundary conditions, these currents will generate the same radiated field outside the closed surface as the original sources. This allows to formulate the antenna problem through a boundary Surface Electric Field Integral Equation (SEFIE) [68],[69],[70], where the natural outcome is the surface current density, say $\boldsymbol{J_A}$, induced over the antenna surface. The integral equation is then converted into a linear system by means of the Methods of Moment (MoM) [66]. After the current distribution

has been determined, the near field, the far field, and other antenna parameters can be obtained.
To model arbitrarily shaped surfaces and to represent the equivalent surface currents over them, planar triangular patch models are particularly appropriate. Some of the advantages of triangular patch surface modeling have been noted by Sankar and Tong [71], as well as by Wang [72]; triangular patches are capable of accurately conforming to any geometrical surface or boundary, and a varying patch density can be used according to the resolution required in the surface geometry. More importantly, triangular patches allow the definition of special basis function for the surface current representation, which are free of fictitious line or point charges.

5.3 Surface Electric Field Integral Equation (SEFIE) formulation

We model the antenna as an arbitrarily shaped perfectly electrically conducting object. The unit vector normal to the interface S is represented by $\hat{\boldsymbol{n}}$. The external medium has permittivity ϵ and permeability μ, which will be the quantities of free space, since we are interested in the electromagnetic scattering in vacuum. We assume that an electric field $\boldsymbol{E^i}$ due to an impressed source is present (in absence of the scatterer). This field is incident on the surface S, and it induces surface currents $\boldsymbol{J_A}$ which radiate a field $\boldsymbol{E^s}$ expressed by [73]

$$\boldsymbol{E^s} = -j\omega \boldsymbol{A} - \nabla \Phi \tag{5.2}$$

with the magnetic vector potential defined as

$$\boldsymbol{A}(\boldsymbol{r}) = \frac{\mu}{4\pi} \int_S \boldsymbol{J_A} \frac{e^{-jkR}}{R} dS' \tag{5.3}$$

and the scalar potential as

$$\Phi(\boldsymbol{r}) = \frac{1}{4\pi\epsilon} \int_S \sigma \frac{e^{-jkR}}{R} dS' \tag{5.4}$$

A harmonic time dependece $\exp(j\omega t)$ is assumed and suppressed, and $k = \omega\sqrt{\mu\epsilon} = 2\pi/\lambda$, where λ is the wavelength. $R = |\boldsymbol{r} - \boldsymbol{r'}|$ is the distance between an arbitrarily located observation point $\boldsymbol{r}$ and a source point $\boldsymbol{r'}$ on S. Both $\boldsymbol{r}$ and $\boldsymbol{r'}$ are defined with reference to a global coordinate system O. The surface charge density σ is related to the surface divergence of $\boldsymbol{J_A}$ through the continuity equation,

$$\nabla_S \cdot \boldsymbol{J_A} = -j\omega\sigma \tag{5.5}$$

We derive the SEFIE for $\boldsymbol{J_A}$ by enforcing the boundary condition $\hat{\boldsymbol{n}} \times \left(\boldsymbol{E^i} + \boldsymbol{E^s}\right) = 0$ on S, thus for $\boldsymbol{r}$ on S

$$\left[-j\omega\mu \int_{S'} G\left(\boldsymbol{r} - \boldsymbol{r'}\right) \boldsymbol{J_A}\left(\boldsymbol{r'}\right) dS' + \frac{1}{j\omega\epsilon} \nabla \left(\nabla \cdot \int_{S'} G\left(\boldsymbol{r} - \boldsymbol{r'}\right) \boldsymbol{J_A}\left(\boldsymbol{r'}\right) dS' \right) \right]_{tan} = -\boldsymbol{E^i}_{tan} \tag{5.6}$$

where the Green's function of the Helmholtz operator in free space is

$$G\left(\boldsymbol{r}-\boldsymbol{r'}\right)=\frac{\exp\left(-jk|\boldsymbol{r}-\boldsymbol{r'}|\right)}{4\pi|\boldsymbol{r}-\boldsymbol{r'}|} \tag{5.7}$$

Consider now the divergence in the LHS of Eq. 5.6 applied along the surface with respect to $\boldsymbol{r}$

$$\begin{aligned}\nabla\cdot\int_{S'}G\left(\boldsymbol{r}-\boldsymbol{r'}\right)\boldsymbol{J_A}\left(\boldsymbol{r'}\right)dS'&=\int_{S'}\left(\nabla G\left(\boldsymbol{r}-\boldsymbol{r'}\right)\right)\cdot\boldsymbol{J_A}\left(\boldsymbol{r'}\right)dS'=\\&=-\int_{S'}\left(\nabla_{S'}G\left(\boldsymbol{r}-\boldsymbol{r'}\right)\right)\cdot\boldsymbol{J_A}\left(\boldsymbol{r'}\right)dS'\end{aligned} \tag{5.8}$$

where $\nabla_{S'}$ indicates that the gradient operator is applied along the surface S' with respect to the variable $\boldsymbol{r'}$. Consider now

$$\begin{aligned}&\int_{S'}\nabla_{S'}\cdot\left(G\left(\boldsymbol{r}-\boldsymbol{r'}\right)\boldsymbol{J_A}\left(\boldsymbol{r'}\right)\right)dS'=\\&=\int_{S'}\left(\nabla_{S'}G\left(\boldsymbol{r}-\boldsymbol{r'}\right)\right)\cdot\boldsymbol{J_A}\left(\boldsymbol{r'}\right)dS'+\int_{S'}G\left(\boldsymbol{r}-\boldsymbol{r'}\right)\left(\nabla_{S'}\cdot\boldsymbol{J_A}\left(\boldsymbol{r'}\right)\right)dS'\end{aligned} \tag{5.9}$$

Since the normal component of $\boldsymbol{J_A}$ is zero at the surface boundaries, applying Gauss's theorem, we have

$$\int_{S'}\nabla_{S'}\cdot\left(G\left(\boldsymbol{r}-\boldsymbol{r'}\right)\boldsymbol{J_A}\left(\boldsymbol{r'}\right)\right)dS'=\oint_{C'}\hat{\boldsymbol{n_b}}\cdot\left(G\left(\boldsymbol{r}-\boldsymbol{r'}\right)\boldsymbol{J_A}\left(\boldsymbol{r'}\right)\right)dC'=0 \tag{5.10}$$

where C' is the contour around the surface S', and $\hat{\boldsymbol{n_b}}$ is the unit vector normal to the contour and pointing outward of the contour C'. Substituting this result in Eq. 5.9 yields

$$\int_{S'}\left(\nabla_{S'}G\left(\boldsymbol{r}-\boldsymbol{r'}\right)\right)\cdot\boldsymbol{J_A}\left(\boldsymbol{r'}\right)dS'=-\int_{S'}G\left(\boldsymbol{r}-\boldsymbol{r'}\right)\left(\nabla_{S'}\cdot\boldsymbol{J_A}\left(\boldsymbol{r'}\right)\right)dS' \tag{5.11}$$

We can simplify Eq. 5.8

$$\nabla\cdot\int_{S'}G\left(\boldsymbol{r}-\boldsymbol{r'}\right)\boldsymbol{J_A}\left(\boldsymbol{r'}\right)dS'=\int_{S'}G\left(\boldsymbol{r}-\boldsymbol{r'}\right)\left(\nabla_{S'}\cdot\boldsymbol{J_A}\left(\boldsymbol{r'}\right)\right)dS' \tag{5.12}$$

so that Eq. 5.6 now reads

$$\begin{aligned}&\Bigg[-j\omega\mu\int_{S'}G\left(\boldsymbol{r}-\boldsymbol{r'}\right)\boldsymbol{J_A}\left(\boldsymbol{r'}\right)dS'+\\&+\frac{1}{j\omega\epsilon}\nabla_S\int_{S'}G\left(\boldsymbol{r}-\boldsymbol{r'}\right)\left(\nabla_{S'}\cdot\boldsymbol{J_A}\left(\boldsymbol{r'}\right)\right)dS'\Bigg]_{tan}=-\boldsymbol{E^i}_{tan}\,,\,\boldsymbol{r}\in S\end{aligned} \tag{5.13}$$

It is worth noticing that the Green function in Eq. 5.7 has a singular behavior for $\boldsymbol{r}$ approaching $\boldsymbol{r'}$; moreover, because of derivatives applied to the argument that can become singular, it is necessary to solve SEFIE equation with special carefulness. The set of basis functions necessary to represent the surface current on the antenna and the testing procedure in the MoM will be addressed in the following paragraphs.

5.4 The Rao-Wilton-Glisson (RWG) function

We assume that a suitable triangulation has been found to approximate the antenna surface S [74], and we discuss a set of basis functions introduced by Glisson [75], particularly useful for the current representation over the antenna surface, for the use with the SEFIE and triangular patch modeling. The required set of basis functions has to be chosen so as their linear combination can approximate the surface current with an acceptable accuracy. Since surface triangulation is used in discretizing the object under study, local basis functions having triangular patches as support are then chosen.
The Rao-Wilton-Glisson (RWG) functions [73] have the aforementioned characteristics and they are adopted as expansion functions in the Method of Moments. With reference to Fig. 5.1, each basis function $\boldsymbol{f_n}$ is defined on two adjoining triangles T_n^+ and T_n^- connected through the nth common edge of length l_n. The plus or minus designation of the triangles is determined by choosing the positive surface current direction (associated with the nth common edge) to be from T_n^+ to T_n^-.
All points on the RWG function can be designated either by the vector $\boldsymbol{r_n}^{\pm}$ with respect to the global coordinate system, or by the vector $\boldsymbol{\rho_n}^{\pm}$ in $T_n^{\pm}$ with respect to a coordinate system local to the triangle. The nth RWG basis function is defined by

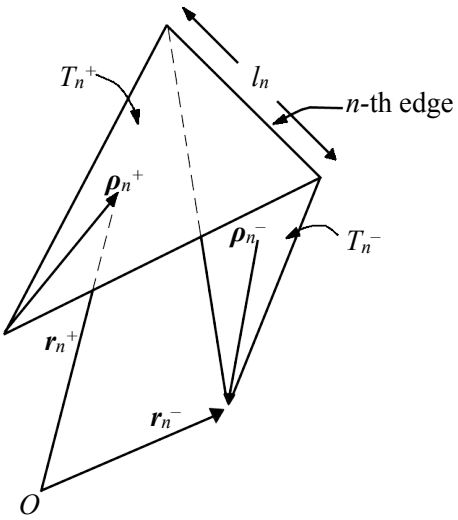

Figure 5.1: Triangle pair and geometrical parameters associated with interior edge.

$$\boldsymbol{f}_n(\boldsymbol{r}) = \begin{cases} \frac{l_n}{2A_n^+}\boldsymbol{\rho}_n^+ & , \boldsymbol{r} \in T_n^+ \\ \\ \frac{l_n}{2A_n^-}\boldsymbol{\rho}_n^- & , \boldsymbol{r} \in T_n^- \end{cases} \tag{5.14}$$

where $A_n^{\pm}$ is the area of triangle $T_n^{\pm}$. The current distribution has a component normal to the common edge l_n, as shown in Fig. 5.2. There is no line charge along the considered edge. Besides, the current has no component normal to the boundary of the surface made up by

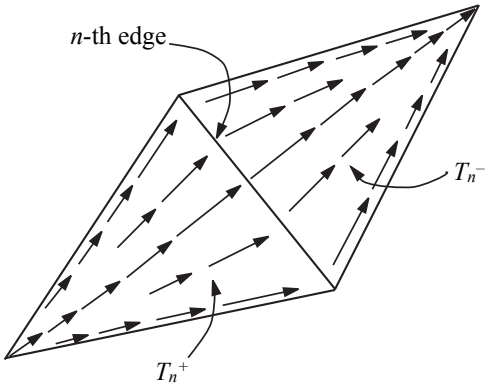

Figure 5.2: Current flow over the n-th RWG basis function from T_n^+ to T_n^-.

the couple of triangles T_n^+ and T_n^-, neither are there any line charges. (See Appendix C for more details on the properties of RWG basis function.)

5.5 Matrix equation

From Eq. 5.13 we apply the Galerkin Method of Moments by expanding the surface current density $\boldsymbol{J_A}(\boldsymbol{r'})$ in terms of RWG basis functions as

$$\boldsymbol{J_A}(\boldsymbol{r'}) \cong \sum_{n=1}^{N} I_n \boldsymbol{f}_n(\boldsymbol{r'}) \tag{5.15}$$

where N is the number of nonboundary edges associated with the triangular patch mesh. Substituting Eq. 5.15 in 5.13 leads to the equation

$$\begin{aligned} &- j\omega\mu \sum_{n=1}^{N} I_n \int_{T_n^+ \cup T_n^-} G(\boldsymbol{r}-\boldsymbol{r'})\, \boldsymbol{f}_n(\boldsymbol{r'})\, dS' + \\ &+ \frac{1}{j\omega\epsilon} \sum_{n=1}^{N} I_n \nabla_S \int_{T_n^+ \cup T_n^-} G(\boldsymbol{r}-\boldsymbol{r'}) \left(\nabla_{S'} \cdot \boldsymbol{f}_n(\boldsymbol{r'})\right) dS' = -\boldsymbol{E^i}_{tan}(\boldsymbol{r}) \ , \ \boldsymbol{r} \in S \end{aligned} \tag{5.16}$$

The next step in the Method of Moments consists of selecting a suitable test function $\boldsymbol{g}$. The testing procedure is accomplished by using a symmetric product defined as

$$\langle \boldsymbol{f}_n, \boldsymbol{g} \rangle = \int_S \boldsymbol{f}_n \cdot \boldsymbol{g}\, dS \tag{5.17}$$

In principle, we are free to use any test functions we wish; however, for many problems the choice of testing function is crucial to obtain a good solution. One of the most common approach is the method of Galerkin, according to which the basis functions themselves are used as the testing functions. This has the advantage of enforcing the boundary conditions

throughout the solution domain. By testing Eq. 5.16 with the Galerkin MoM approach, we get

$$
\begin{aligned}
&- j\omega\mu \sum_{n=1}^{N} I_n \int_{T_m^+ \cup T_m^-} \boldsymbol{f}_m(\boldsymbol{r}) \cdot \left(\int_{T_n^+ \cup T_n^-} G(\boldsymbol{r}-\boldsymbol{r'})\, \boldsymbol{f}_n(\boldsymbol{r'})\, dS' \right) dS + \\
&+ \frac{1}{j\omega\epsilon} \sum_{n=1}^{N} I_n \int_{T_m^+ \cup T_m^-} \boldsymbol{f}_m(\boldsymbol{r}) \cdot \left(\nabla_S \int_{T_n^+ \cup T_n^-} G(\boldsymbol{r}-\boldsymbol{r'}) \left(\nabla_{S'} \cdot \boldsymbol{f}_n(\boldsymbol{r'}) \right) dS' \right) dS = \\
&= - \int_{T_m^+ \cup T_m^-} \boldsymbol{f}_m(\boldsymbol{r}) \cdot \boldsymbol{E^i}_{tan}(\boldsymbol{r})\, dS\,,\ \boldsymbol{r} \in S
\end{aligned}
\tag{5.18}
$$

with $m = 1, \ldots, N$ and where $\boldsymbol{f}_n$ and $\boldsymbol{f}_m$ represent the nth basis and the mth testing RWG functions, respectively. In Fig. 5.3 the nth RWG basis function and the mth RWG testing function are shown. By substituting Eq. C.9 in Eq. 5.18, we have

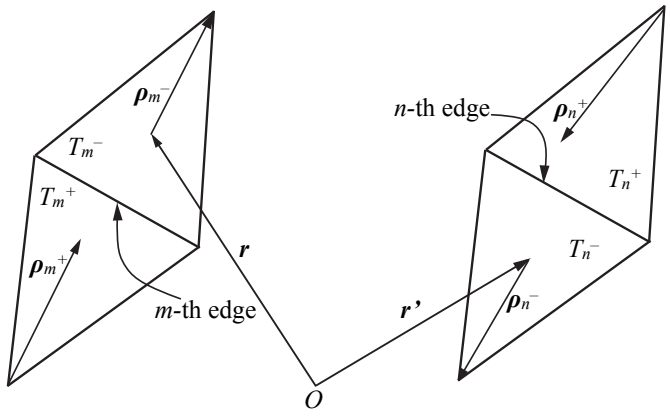

Figure 5.3: Graphical representation of RWG functions used as basis and testing functions.

$$
\begin{aligned}
&- j\omega\mu \sum_{n=1}^{N} I_n \int_{T_m^+ \cup T_m^-} \boldsymbol{f}_m(\boldsymbol{r}) \cdot \left(\int_{T_n^+ \cup T_n^-} G(\boldsymbol{r}-\boldsymbol{r'})\, \boldsymbol{f}_n(\boldsymbol{r'})\, dS' \right) dS + \\
&+ \frac{1}{j\omega\epsilon} \sum_{n=1}^{N} I_n \int_{T_m^+ \cup T_m^-} \left(\nabla_S \cdot \boldsymbol{f}_m(\boldsymbol{r}) \right) \int_{T_n^+ \cup T_n^-} G(\boldsymbol{r}-\boldsymbol{r'}) \left(\nabla_{S'} \cdot \boldsymbol{f}_n(\boldsymbol{r'}) \right) dS' dS = \\
&= - \int_{T_m^+ \cup T_m^-} \boldsymbol{f}_m(\boldsymbol{r}) \cdot \boldsymbol{E^i}_{tan}(\boldsymbol{r})\, dS\,,\ \boldsymbol{r} \in S
\end{aligned}
\tag{5.19}
$$

with $m = 1, \ldots, N$. Finally, Eq. 5.19 can be expressed succinctly as

$$
\boldsymbol{Z}\boldsymbol{I} = \boldsymbol{F} \tag{5.20}
$$

where $\boldsymbol{Z} = [Z_{m,n}]$ is the $N \times N$ system matrix, $\boldsymbol{I}$ is the unknown vector of current density coefficients, and $\boldsymbol{F}$ is the excitation vector. Substituting in Eq. 5.19 the expression for the

RWG function, and employing the properties summarized in Appendix C, we can write each matrix element as

$$
\begin{aligned}
Z_{m,n} = -j\omega\mu\frac{l_m l_n}{4}\Bigg[&\frac{1}{A_m^+ A_n^+}\int_{T_m^+}\int_{T_n^+}\boldsymbol{\rho}_m^+\cdot\boldsymbol{\rho}_n^+ G\left(\boldsymbol{r}-\boldsymbol{r'}\right)dS'dS+\\
&+\frac{1}{A_m^+ A_n^-}\int_{T_m^+}\int_{T_n^-}\boldsymbol{\rho}_m^+\cdot\boldsymbol{\rho}_n^- G\left(\boldsymbol{r}-\boldsymbol{r'}\right)dS'dS+\frac{1}{A_m^- A_n^+}\int_{T_m^-}\int_{T_n^+}\boldsymbol{\rho}_m^-\cdot\boldsymbol{\rho}_n^+ G\left(\boldsymbol{r}-\boldsymbol{r'}\right)dS'dS+\\
&\frac{1}{A_m^- A_n^-}\int_{T_m^-}\int_{T_n^-}\boldsymbol{\rho}_m^-\cdot\boldsymbol{\rho}_n^- G\left(\boldsymbol{r}-\boldsymbol{r'}\right)dS'dS\Bigg]+\\
&+\frac{1}{j\omega\epsilon}l_m l_n\Bigg[\frac{1}{A_m^+ A_n^+}\int_{T_m^+}\int_{T_n^+}G\left(\boldsymbol{r}-\boldsymbol{r'}\right)dS'dS-\frac{1}{A_m^+ A_n^-}\int_{T_m^+}\int_{T_n^-}G\left(\boldsymbol{r}-\boldsymbol{r'}\right)dS'dS\\
&-\frac{1}{A_m^- A_n^+}\int_{T_m^-}\int_{T_n^+}G\left(\boldsymbol{r}-\boldsymbol{r'}\right)dS'dS+\frac{1}{A_m^- A_n^-}\int_{T_m^-}\int_{T_n^-}G\left(\boldsymbol{r}-\boldsymbol{r'}\right)dS'dS\Bigg]
\end{aligned}
\tag{5.21}
$$

5.6 Voltage Source Model

The antenna excitation is provided by means of a voltage-generator model for a RWG basis function. Consider the PEC conductor surface in Fig. 5.4, where the uniformly distributed electric field $\boldsymbol{E^i} = \left(V^{ant}/d\right)\hat{\boldsymbol{x}}$ is assumed to exist for $0 \leq x \leq d$, and resides on the conductor surface only. When the antenna is excited by an incident field $\boldsymbol{E^i}$, the current will distribute itself in such a way that the scattered field $\boldsymbol{E^s}_{tan}$ cancels $\boldsymbol{E^i}_{tan}$ in the support region of $\boldsymbol{E^i}$, also known as *port region*. Outside the port region, $\boldsymbol{E^s}_{tan}$

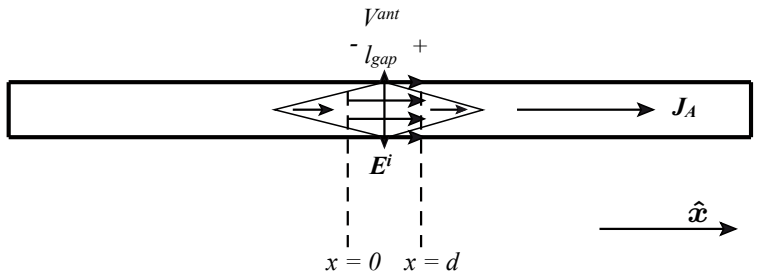

Figure 5.4: Voltage-current and field definitions for a RWG voltage generator.

must vanish across the remaining part of the PEC conductor, because outside the source region $\boldsymbol{E^i} = 0$, hence, we have that the total field $\boldsymbol{E} = \boldsymbol{E^s}\left(\boldsymbol{J_A}\right)$. The total electric field $\boldsymbol{E}$ is directed from the plus to minus terminal of the voltage source so that V^{ant} can be expressed as

$$
V^{ant} = -\int_0^d \boldsymbol{E}\cdot\hat{\boldsymbol{x}}dx = -\int_0^d \boldsymbol{E^s}\left(\boldsymbol{J_A}\right)\cdot\hat{\boldsymbol{x}}dx = \int_0^d \boldsymbol{E^i}\cdot\hat{\boldsymbol{x}}dx \tag{5.22}
$$

In order to ease the numerical computations, it is convenient to reduce the support of $\boldsymbol{E^i}$ to an infinitely small region as d approaches zero $d \to 0$, while maintaining its voltage

$$\boldsymbol{E^i} = V^{ant}\delta\left(\boldsymbol{r} - \boldsymbol{r}_{gap}\right)\hat{\boldsymbol{x}} \tag{5.23}$$

where the field has been concentrated along a line of length l_{gap} crossing the conductor. If the delta-field-distribution coincides with a single common edge of a RWG basis function (say $\boldsymbol{f}_p$, where the subscript p stands for "port"), the excitation vector $\boldsymbol{F}$ has only one non-zero element. In particular, the RHS of Eq. 5.19 becomes

$$\begin{aligned} &-\int_{T_m^+ \cup T_m^-} \boldsymbol{f}_m\left(\boldsymbol{r}\right) \cdot \boldsymbol{E^i}\left(\boldsymbol{r}\right) dS = -\int_{T_p^+ \cup T_p^-} \boldsymbol{f}_p\left(\boldsymbol{r}\right) \cdot \boldsymbol{E^i}\left(\boldsymbol{r}\right) dS = \\ &= -V^{ant}\int_{T_p^+ \cup T_p^-} \left(\boldsymbol{f}_p \cdot \hat{\boldsymbol{x}}\right)\delta\left(\boldsymbol{r} - \boldsymbol{r}_{gap}\right) dS = -V^{ant} l_{gap} \end{aligned} \tag{5.24}$$

5.7 Numerical implementation

The integrals in Eq. 5.21 have two different forms, scalar

$$I_s = \int_T \int_{T'} G\left(\boldsymbol{r} - \boldsymbol{r'}\right) dS' dS \tag{5.25}$$

and vector

$$I_v = \int_T \int_{T'} \boldsymbol{\rho}_o \cdot \boldsymbol{\rho}_s G\left(\boldsymbol{r} - \boldsymbol{r'}\right) dS' dS \tag{5.26}$$

where $\boldsymbol{\rho}_o\left(\boldsymbol{r}\right)$ and $\boldsymbol{\rho}_s\left(\boldsymbol{r'}\right)$ are the position vectors for the observation and source triangles, as shown in Fig. 5.5. The Green function $G\left(\boldsymbol{r} - \boldsymbol{r'}\right)$ which appears in Eqs. 5.25, 5.26 contains

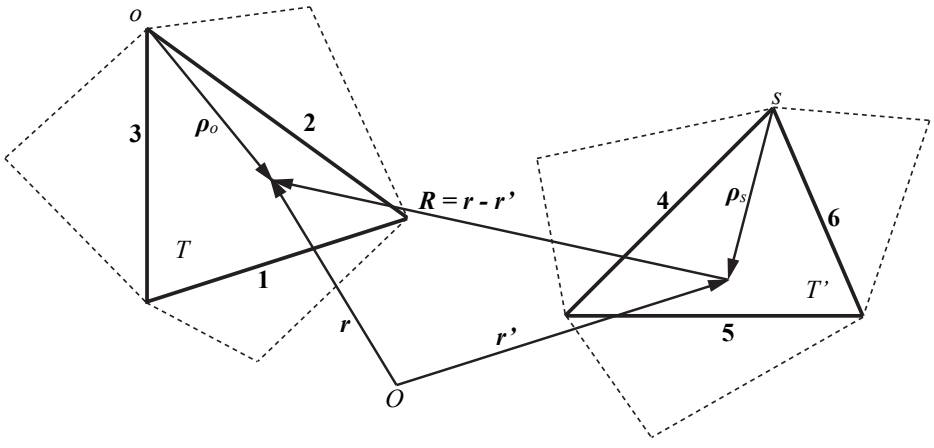

Figure 5.5: Observation and source triangular patches.

an integrable singularity when the observation point $\boldsymbol{r}$ is approaching the source point $\boldsymbol{r'}$, namely, $R \to 0$. This means that different approaches should be considered depending on the relative positions of the triangles T and T'. As far as the triangular-patched mesh is concerned, we can identify three situations (see Appendix D):

1. T and T' coincide so that the integration is performed over a single patch and the distance R may become zero.
2. T and T' share either an edge or a vertex, and R may become zero.
3. T and T' are disjoint triangles, thus the distance R is never zero and the integrals can be computed numerically by means of Gaussian quadrature rules over the triangular surfaces.

In such situations when $R \to 0$, we need to extract the singularity from the Green function

$$G = [G - G_{sing}] + G_{sing} \tag{5.27}$$

where now the first term in square brackets on the RHS of Eq. 5.27 is regular and can be evaluated numerically, while G_{sing} reads

$$G_{sing} = \frac{1}{4\pi R} - \frac{k^2 R}{8\pi} \tag{5.28}$$

Substituting Eq. 5.28 in Eqs. 5.25, 5.26, we have the following integrals

$$I_s = \underbrace{\frac{1}{4\pi}\int_T\int_{T'} \frac{1}{R} dS' dS}_{I_1} - \underbrace{\frac{k^2}{8\pi}\int_T\int_{T'} R dS' dS}_{I_3} \tag{5.29}$$

$$I_v = \underbrace{\frac{1}{4\pi}\int_T \boldsymbol{\rho}_o \cdot \int_{T'} \boldsymbol{\rho}_s \frac{1}{R} dS' dS}_{I_2} - \underbrace{\frac{k^2}{8\pi}\int_T \boldsymbol{\rho}_o \cdot \int_{T'} \boldsymbol{\rho}_s R dS' dS}_{I_4} \tag{5.30}$$

In the above case 1., the integrals I_1 and I_2 are carried out analytically [76]. The surface integrals over T and T' are modified in contour integrals along the triangle boundaries C and C', respectively, by means of the Stokes' theorem. Analytical expression have been reported in Appendix D for sake of completeness. The evaluation of I_3 and I_4 is performed in two different steps: the integral over T' is expressed in a closed form by means of formulas in [77] and reported in Appendix D. Then, the integration over the triangle T is evaluated numerically by means of Gaussian quadrature formulas (see Appendix D).
When we have to deal with case 2., I_1, I_2, I_3 and I_4 will be calculated in closed form for the integration over the triangle T', as suggested in [77], whereas Gaussian formulas will be employed for the integration over the triangle T.
In case 3., no such issues as $R \to 0$ are considered, so that numerical quadrature formulas can be invoked.

5.8 Electric and Magnetic Fields radiated by a surface current distribution flowing on a PEC object

Once the problem has been solved for the current density on the antenna, we can determine the electric and magnetic fields radiated by the antenna. By means of Eq. 5.2 - 5.5, we

evaluate the electric field radiated by the antenna

$$\begin{aligned}\boldsymbol{E}(\boldsymbol{r}) = &- jkZ_0 \left\{ \int_{S'} G\left(|\boldsymbol{r}-\boldsymbol{r'}|\right) \boldsymbol{J_A}\left(\boldsymbol{r'}\right) dS' + \right. \\ &\left. + \frac{1}{k^2} \nabla \left[\int_{S'} G\left(|\boldsymbol{r}-\boldsymbol{r'}|\right) \left(\nabla' \cdot \boldsymbol{J_A}\left(\boldsymbol{r'}\right)\right) dS' \right] \right\}\end{aligned} \tag{5.31}$$

where Z_0 is the impedance of free space. Now, considering Eq. 5.15 and the properties of RWG functions in Appendix C, we have

$$\begin{aligned}\boldsymbol{E}(\boldsymbol{r}) = &- jkZ_0 \sum_{n=1}^{N} I_n l_n \\ &\left\{ \left[\frac{1}{2A_n^+} \int_{T_n^+} G\left(|\boldsymbol{r}-\boldsymbol{r'}|\right) \boldsymbol{\rho}_n^+\left(\boldsymbol{r'}\right) dS' + \frac{1}{2A_n^-} \int_{T_n^-} G\left(|\boldsymbol{r}-\boldsymbol{r'}|\right) \boldsymbol{\rho}_n^-\left(\boldsymbol{r'}\right) dS' \right] \right. \\ &\left. + \frac{1}{k^2} \left[\frac{1}{A_n^+} \int_{T_n^+} \nabla G\left(|\boldsymbol{r}-\boldsymbol{r'}|\right) dS' - \frac{1}{A_n^-} \int_{T_n^-} \nabla G\left(|\boldsymbol{r}-\boldsymbol{r'}|\right) dS' \right] \right\}\end{aligned} \tag{5.32}$$

where

$$\nabla G = - \left[jkG\left(|\boldsymbol{r}-\boldsymbol{r'}|\right) + \frac{G\left(|\boldsymbol{r}-\boldsymbol{r'}|\right)}{|\boldsymbol{r}-\boldsymbol{r'}|} \right] \frac{\boldsymbol{r}-\boldsymbol{r'}}{|\boldsymbol{r}-\boldsymbol{r'}|} \tag{5.33}$$

The magnetic field can be evaluated from the magnetic vector potential $\boldsymbol{A}$ taking the curl $\nabla\times$

$$\boldsymbol{B}(\boldsymbol{r}) = \nabla \times \left\{ \mu \int_{S'} G\left(|\boldsymbol{r}-\boldsymbol{r'}|\right) \boldsymbol{J_A}\left(\boldsymbol{r'}\right) dS' \right\} \tag{5.34}$$

which becomes

$$\begin{aligned}\boldsymbol{B}(\boldsymbol{r}) = &\mu \sum_{n=1}^{N} I_n l_n \\ &\left\{ \frac{1}{2A_n^+} \int_{T_n^+} - \left[jk \frac{G\left(|\boldsymbol{r}-\boldsymbol{r'}|\right)}{|\boldsymbol{r}-\boldsymbol{r'}|} + \frac{G\left(|\boldsymbol{r}-\boldsymbol{r'}|\right)}{|\boldsymbol{r}-\boldsymbol{r'}|^2} \right] \left(\boldsymbol{r}-\boldsymbol{r'}\right) \times \boldsymbol{\rho}_n^+ dS' + \right. \\ &\left. + \frac{1}{2A_n^-} \int_{T_n^-} - \left[jk \frac{G\left(|\boldsymbol{r}-\boldsymbol{r'}|\right)}{|\boldsymbol{r}-\boldsymbol{r'}|} + \frac{G\left(|\boldsymbol{r}-\boldsymbol{r'}|\right)}{|\boldsymbol{r}-\boldsymbol{r'}|^2} \right] \left(\boldsymbol{r}-\boldsymbol{r'}\right) \times \boldsymbol{\rho}_n^- dS' \right\}\end{aligned} \tag{5.35}$$

if we cosider Eqs. 5.15, 5.33 and the properties of RWG functions in Appendix C.

5.9 Numerical accuracy

In order to provide evidence that the code can produce results in agreement with experimental data, we benchmarked the code firstly against analytical solutions for the current distribution of a $\lambda/2$ dipole, and for the self inductance of a small circle of thin strip, thus assessing at the same time the code accuracy with different working frequency, and with different mesh refinements. Finally, the code accuracy for different meshes has been analyzed for a Nagoya Type III antenna, as the one showed in Fig. 2.2(b), which is commonly used in helicon plasma source experiments.

5.9.1 Dipole current distribution

A dipole antenna consists of two metal wires, in line with each other, with a small space between them providing a center-fed driven element. The voltage is applied to the antenna at the center, between the two conductors. This kind of antenna is the simplest practical antenna from a theoretical point of view. We considered the particular case of a half-wave dipole, formed by two quarter-wavelength conductors or elements placed back-to-back for a total length of $L_d = \lambda/2$; the current distribution is maximal at the center, and it is approximately cosinusoidal along the length of the dipole, with a node at each end and an antinode in the center [78]. We simulated a half-wave dipole excited by means of a time-harmonic voltage function $V(t) = V_0 e^{j(\omega t)}$, and simulation parameters: voltage amplitude $V_0 = 1.0$ V, excitation frequency $f = 50.0$ MHz, dipole length $L_d = \frac{\lambda}{2} = 3.0$ m, dipole width $w = 0.03$ m.
In Fig. 5.6 the geometry is shown with the associated excitation provided by the voltage gap across the *Ground* and *Port* regions; the rest of the antenna surface is made of PEC. It is worth noticing that the dipole extension along the x direction is much greater than along the y direction, as we wanted the dipole to be monodimensional. The triangular-patched

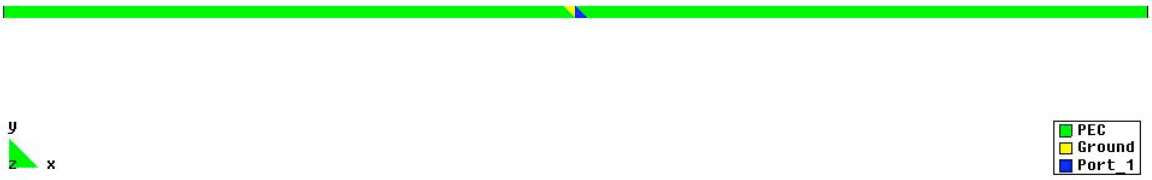

Figure 5.6: Dipole geometry, with length $L_d = 3.0$ m, and width $w = 0.03$ m. The dipole is excited in the middle by a voltage gap providing $V_0 = 1.0$ V.

mesh has been plotted in Fig. 5.7. The current distribution shown in Fig. 5.8 is in good

Figure 5.7: Dipole mesh for a dipole with length $L_d = 3.0$ m, and with $w = 0.03$ m.

agreement with the analytical current distribution for the current along a half-wave dipole; as expected, the current approaches zero as soon as we get closer to the left and right ends of the dipole itself, while the current over the dipole tends to a theoretical cosinusoidal distribution. However, a complete agreement is missing at the center, due to a non-perfect matching of the dipole length and the working frequency; as a matter of fact, a half-wave dipole working at 50.0 MHz should have a total length $L_d \approx 2.997925$ m against the $L_d = 3.0$ m used in this simulation.

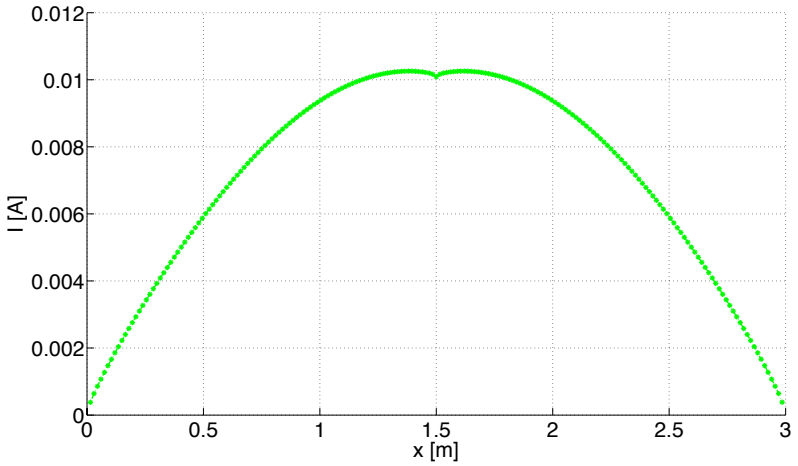

Figure 5.8: Current distribution for a dipole with length $L_d = 3.0$ m, and with $w = 0.03$ m, working at frequency $f = 50.0$ MHz.

5.9.2 Self inductance of a small loop

We considered a small circle of thin strip excited in the low frequency regime. The excitation is provided by means of a voltage gap as in the previous case. We solved for the current distribution, we evaluated the impedance, and, finally, compared it against the self-inductance provided by analytical formulas. In the limit of a small circle of thin strip fed at low frequency , so that it is not necessary to take into account of the finite velocity of propagation, the law of Biot and Savart can be used for the analytical derivation of the self inductance. Under these hypotheses, a circular band of radius a and with width b has a self inductance given by the Rayleigh's formula [79]

$$L = \mu_0 a \left[\log\left(\frac{8a}{b}\right) - \frac{1}{2} + \frac{b^2}{32a^2}\left(\log\left(\frac{8a}{b}\right) + \frac{1}{4}\right)\right] \tag{5.36}$$

We simulated a circle of thin strip with radius $a = 0.02$ m, and width $b = a/10$ in the frequency range from 1.0 MHz to 30 MHz. For these simulation parameters, the Rayleighs formula still holds, and it gives a self-inductance $L = 9.74 \times 10^{-8}$ H. In Figs. 5.9(a) and 5.9(b) the geometry and the mesh of the considered loop are shown; once again the excitation is provided by means of voltage gap across the *Ground* and *Port* regions, as pictured in Fig. 5.9(a). In Fig. 5.9(b) a mesh with 96 RWG basis functions is shown; however, in the present simulation a different number of RWG basis functions, i.e. 60, 96 and 160, have been used in order to assess the code accuracy as a function of the mesh refinement level. As shown in Fig. 5.10, the self inductance of the circle of thin strip has been reported as a function of the excitation frequency, and for different mesh refinements. The agreement between the analytical and numerical solutions is excellent, considering that the analytical formula in Eq. 5.36 is exact in the DC regime, and it provides a good approximation if the circuit is small, and it works at a low frequency. Specifically, the code gives an impedance with a percent error less than $< 1\%$ when the mesh is coarse, with 60 RWG functions. When the mesh is refined and 160 RWG functions used, the percent error decreases below

(a) PEC loop (green), with *Ground* (yellow), and *Port* (blue).

(b) Mesh with 96 RWG functions.

Figure 5.9: Loop with radius $a = 0.02$ m, and width $b = 0.002$ m.

$< 0.1\%$.

The trend of the numerical accuracy as a function of the number of RWG functions is upper bounded by the analytical solution; as far as the MoM method is concerned, when the number of RWG basis functions becomes higher (higher than 200 in the case considered here), numerical instabilities arise that destroy results accuracy. In fact, for a given geometry, as the number of basis functions increases, triangular patches associated with each basis function become smaller and smaller. For this reason, the condition number of the system matrix may grow really large thus making the solution less accurate. The problem may be overcome by using specialized set of basis functions [80], but this is out of the scope of this work.

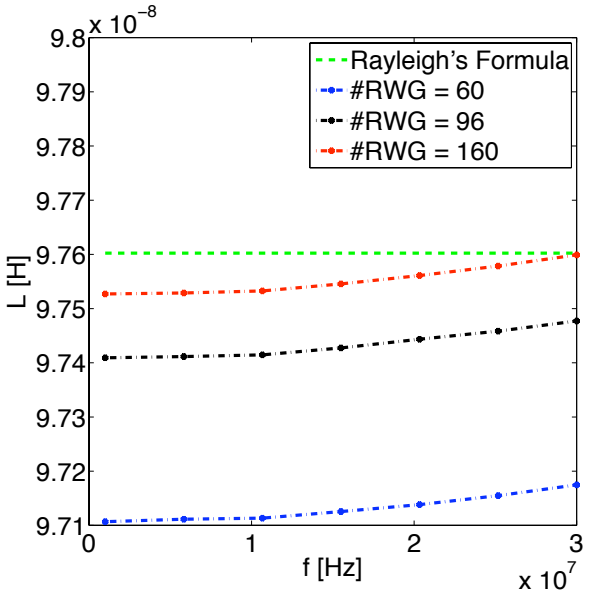

Figure 5.10: Inductance of a circle of thin strip as a function of the frequency and for different mesh refinements (specified by the number of RWG basis functions used). The circle of thin strip has radius $a = 0.02$ m, and width $b = 0.002$ m.

5.9.3 Mesh analysis for a Nagoya Type III antenna

With reference to Fig. 2.2(b), we considered an actual antenna commonly used in helicon plasma sources. The Nagoya Type III is made of two loops at both ends and two legs connecting the loops; in particular, the loops have radius $a = 0.01$ m, and the antenna has an axial extension $L_l = 0.1$ m, while it is infinitesimally thin along the radial direction, and having a width $w = 0.001$ m, both for the loops and for the legs.
The antenna has been simulated in the frequency range of interest for helicon plasma sources, namely from $f = 1.0$ MHz to $f = 30$ MHz. Two different meshes have been considered in order to assess the mesh accuracy; each mesh has been identified by the number of basis functions used to represent the current distribution on the antenna surface. As can be seen in Figs. 5.11 and 5.12, both the coarse and the fine mesh has one voltage gap to simulate the harmonic voltage excitation of $V = 1.0$ V applied in the middle of one of the legs. As far as the current distribution is concerned, both meshes give current

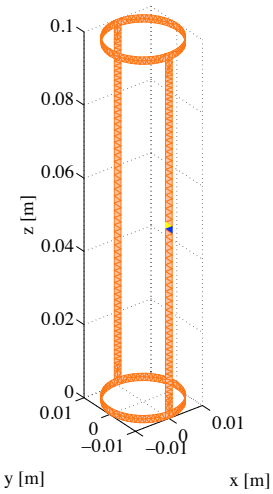

Figure 5.11: Coarse mesh - 806 RWGs.

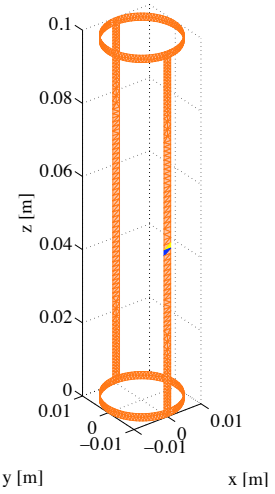

Figure 5.12: Fine mesh - 1400 RWGs.

patterns in good agreement, as shown in Figs. 5.13 and 5.14, where the current distribution has been plotted for the coarse and fine mesh at $f = 1.0$ MHz. It is worth noticing that for a higher number of basis functions (say above > 2000 RWG basis functions) numerical instabilities destroy accuracy of current distribution over the antenna surface.
In order to provide evidence that both meshes describe correctly the solution of the electromagnetic problem over the antenna considered, in Fig. 5.15 we plot the real and imaginary part of the electrical impedance of the antenna; Figs. 5.15(a) and 5.15(b) show that both meshes yield results for the antenna impedance with a difference less than $< 0.01\%$ in the frequency range of interest. Moreover, with reference to Fig. 5.11, we considered the current distribution over the antenna as a function of the excitation frequency simulated with a coarse mesh. In Figs. 5.16(a) - 5.16(d), the current distribution over the Nagoya Type III has been reported for different excitation frequencies.

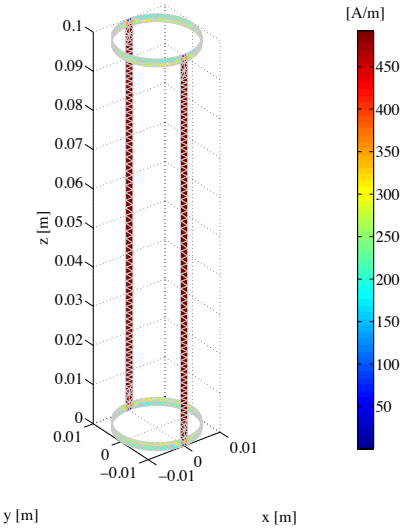

Figure 5.13: Current distribution over the Nagoya Type III antenna at 1.0 MHz for the coarse mesh (806 RWG functions).

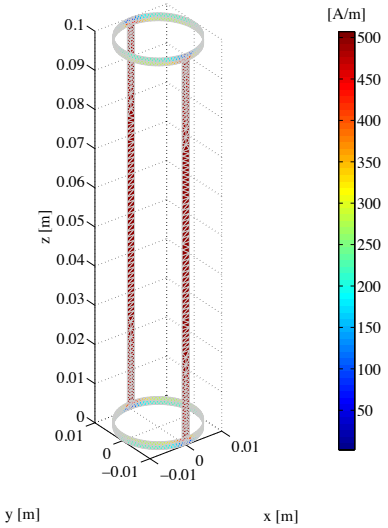

Figure 5.14: Current distribution over the Nagoya Type III antenna at 1.0 MHz for the fine mesh (1400 RWG functions).

Although the current distributions have different intensities depending on the excitation frequency, we recognize the same current pattern; this is due to the vacuum wavelength (associated with each excitation frequency) that is much larger than the geometrical dimensions of the antenna under consideration. From the results gathered so far we can say that the coarse mesh (with 806 RWG basis functions) is detailed enough to correctly represent the current distribution over the antenna surface, and to evaluate the electrical parameters of the antenna itself in the range of frequencies of interest. However, the fine mesh can be helpful in the determination of current distribution detail in the junctions, where the legs are connected to the loops; this has been shown in Figs. 5.17(a) - 5.17(d).

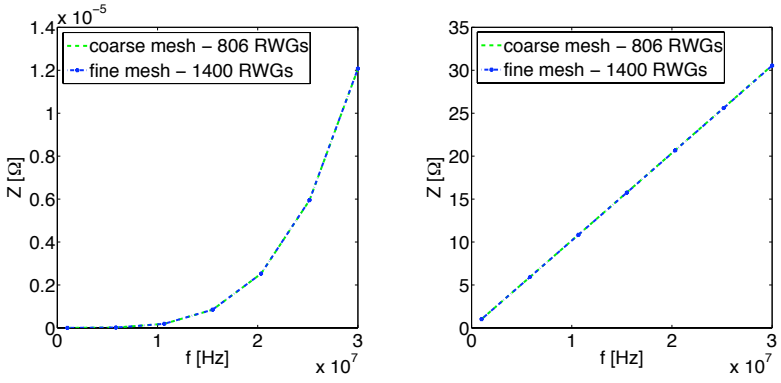

(a) Real part.

(b) Imaginary part.

Figure 5.15: Electrical impedance of the antenna as a function of the excitation frequency for both meshes.

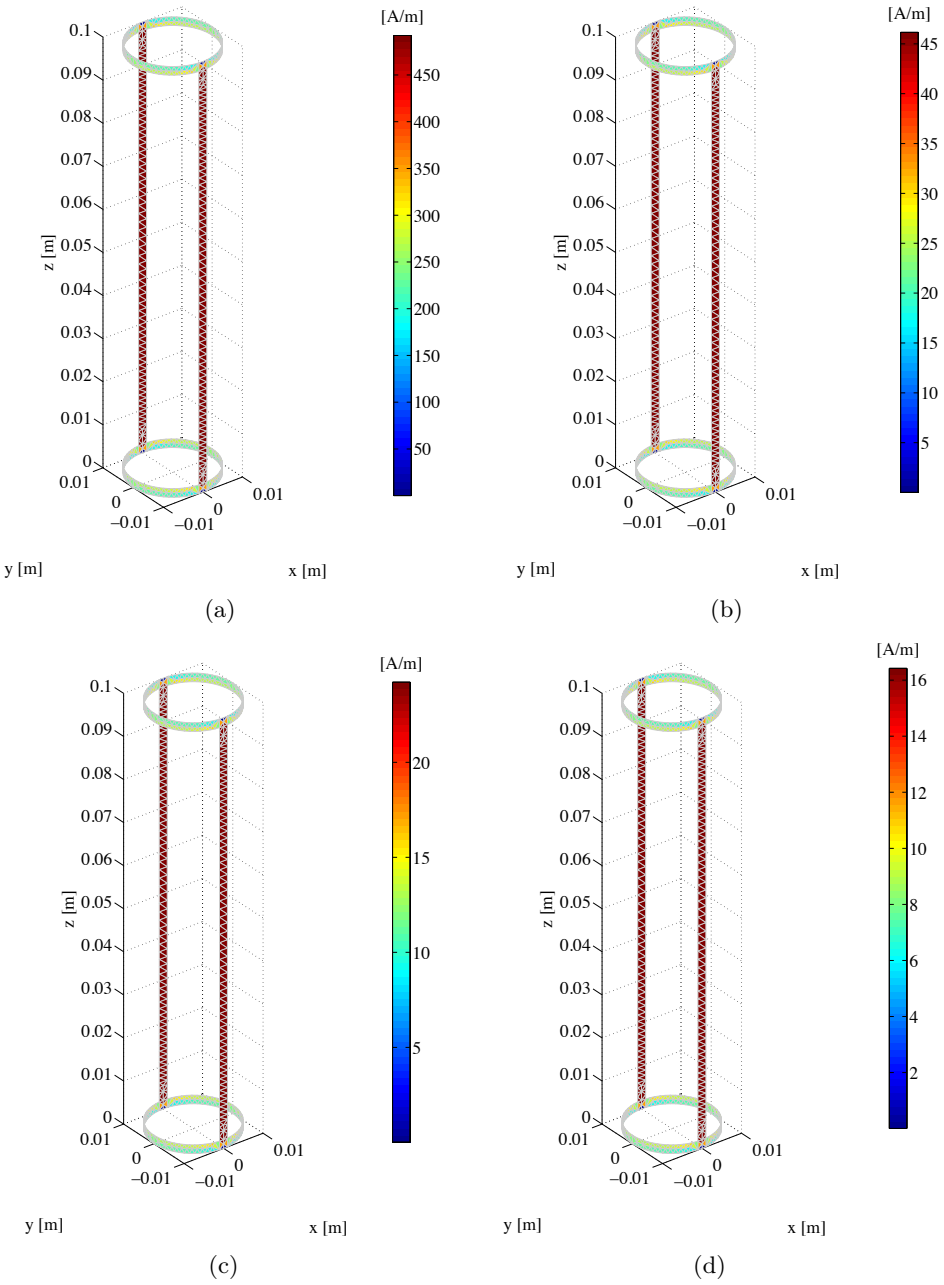

Figure 5.16: Current distribution with a coarse mesh of 806 RWG basis functions represented at different excitation frequency: (a) at $f = 1.0$ MHz, (b) at $f = 10.667$ MHz, (c) at $f = 20.333$ MHz, (d) at $f = 30.0$ MHz.

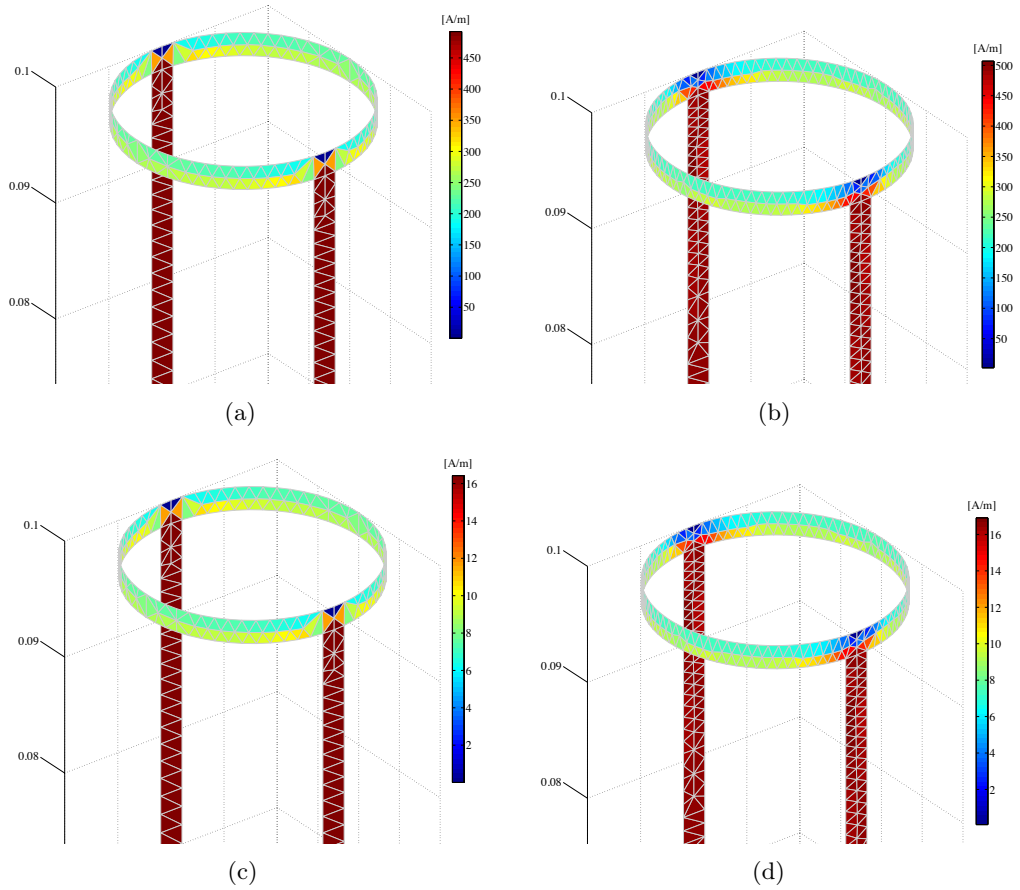

Figure 5.17: Current distribution detail at the leg-loop junction at different excitation frequency, and with different mesh refinements: (a) at $f = 1.0$ MHz with coarse mesh, (b) at $f = 1.0$ MHz with fine mesh, (c) at $f = 30.0$ MHz with coarse mesh, (d) at $f = 30.0$ MHz with fine mesh.

5.10 Conclusions

A tool for the evaluation of radiating electromagnetic fields scattered by PEC antennas in free space has been developed and validated. It can be considered as a part for the treatment of the general problem concerning the interaction of electromagnetic waves with anisotropic bodies (e.g. plasmas), but it can work as a standalone tool as well for the preliminary study and design of antennas.
The Surface Electric Field Integral Equation (SEFIE) has been discretized by means of a Galerkin MoM method, thus obtaining a system matrix equation. RWG basis functions over a triangular domain have been introduced to expand the surface antenna currents. Moreover, the evaluation of matrix elements required the calculation of integrals over triangular patches, where the integrands exhibited an integrable singularity when the distance between the source and the observation points vanishes. In order to cope with this particular aspect, different integration approaches have been used, depending on the

distance between source and observation triangles. All singularities have been extracted and evaluated in closed form, while numerical integration has been applied only for regular functions.
The code has been validated against the current distribution over a dipole (see Fig. 5.8), and the self inductance of a circle of thin strip (see Fig. 5.10), for which analytical expressions are available. A mesh sensitivity analysis has been performed in order to assess the code accuracy with different mesh refinements; specifically, the Nagoya Type III (commonly used in helicon plasma sources) has been considered, and it has been solved in the range of frequency from 1.0 MHz to 30.0 MHz, of particular interest for helicon plasma sources (see Figs. 5.16 and 5.17). Two different meshes have been taken into account, one finer (806 RWGs) than the other (1400 RWGs). A lower number of RWGs than < 806 would result in a non accurate representation of the current distribution over the loops, while an higher number (> 2000) of RWGs would generate numerical instabilities destroying the accuracy of current distribution over the antenna surface. Most notable, the finer mesh can help in a more detailed description of the current distribution over the loops, in particular in the nearby of the leg-loop junctions.

Conclusions

In this research work, several electromagnetic codes have been developed to analyze, design and optimize the helicon plasma thruster, and the antenna for an enhanced communication system. In the present work, firstly we have defined the requisites, and secondly we have described the governing equations and the numerical implementation of: (i) the SPIREs finite-difference frequency-domain electromagnetic solver for magnetized plasma cylinders, (ii) the WAVEQM equilibrium condition solver for radiofrequency heated plasma, (iii) the PARTYWAVE particle in cell code for cylindrical geometries, and (iv) the Moment Method for antenna design. The implemented numerical methods addressed the following requirements: (i) the electromagnetic wave propagation, (ii) the antenna-plasma coupling mechanism, (iii) the power deposition phenomena inside the plasma source, and (iv) the scattering of electromagnetic fields by a PEC antenna. The aforementioned codes are innovative and computationally efficient; in addition, their numerical accuracy has been verified, and they have been benchmarked against relevant physical cases.
In SPIREs, Maxwell wave equations have been discretized along the radius of the plasma cylinder, and Fourier transformed along the other two dimensions and in time; the plasma can be multi-species, and it has been represented by a dielectric tensor, allowing the treatment of inhomogeneous plasma profiles, with variations on plasma density, magnetic field, temperature, and collisional factor. Governing equations have been reduced to the solution of a linear system, solved by means of MUMPS library. The sensitivity analysis on the step size of the grid proved a second order accuracy on the solution, and a convergent asymptotic behavior. The code has been validated in vacuum and in plasma against analytical solutions; it has been benchmarked in inhomogeneous plasma against existing results produced by well established method such as HELIC [26] with percent errors for the radial power deposition and plasma resistance less than 1%.
Differently than either the fields expansion into waveguide modes approach by Mouzouris and Scharer [20], or the finite-element discretization approach by Kamenski and Borg [16], or the fourth-order singularity-flawed ordinary differential equation (ODE) approach by Chen and Arnush [24] [25] [26], SPIREs uses a finite-difference approach in the frequency domain with a Yee mesh along the radius. The fields expansion into waveguide modes by Mouzouris and Scharer [20] is based on spectral domain solutions coming from the dispersion relation. This approach leads to singularity issues in the evaluation of the fast-slow wave resonant mode conversion. The finite-element discretization approach by Kamenski and Borg [16], implemented in the UFEM code, uses a curl-curl second-order equation obtained from the two first-order Maxwell wave equation. In their second-order approach spurious solutions are generated, and a dedicated formulation is needed. The solution adopted by Chen and

Arnush [24], [25] is based on the numerical integration of a fourth-order ODE by means of a numerical Boundary-Value Problem (BVP). Their HELIC code is able to evaluate separately the fields associated to the slow and the fast branch, called Trivelpiece-Gould mode and Helicon mode respectively. Singularity issues related to the small electron mass appear on the slow branch at high magnetic fields, a problem mitigated by means of a series expansion with a parameter depending on the electron mass [26]. Differently than previous methods, SPIREs solves the two first-order curl equations for the direct evaluation of the electromagnetic fields by means of a Yee radial mesh. This finite-difference method does not generate spurious solutions and is intrinsically divergence-free. Singularity problems are not encountered, and fast-slow mode conversion can be calculated exactly with an accuracy depending only on the mesh step size.
Thanks to SPIREs it has been possible to clarify the role played by plasma discharge parameters when aiming at an enhancement in the RF power deposition inside an helicon plasma source. Specifically, the power deposited into the plasma becomes higher increasing the discharge radius and the confinement magnetic fields; besides, the plasma-antenna power coupling can be optimized when the antenna excites $m = 0$ mode number and works in the high range of frequencies considered ($f = 27.12$ MHz). These results are beyond the scope of the present work, but they highlight the capabilities of this newly developed numerical tool in investigating the electromagnetic coupling in a large variety of plasma systems, like ICPs and helicon radiofrequency reactors, or its use as a fast tool for the design of new-concept antennas.
In WAVEQM, the equilibrium conditions of a magnetized plasma cylinder have been calculated by solving the two coupled problems of the electromagnetic power deposition and the macroscopic transport of charged and neutral species. The two codes SPIREs and EQM [26] have been iterated together until convergence, which assures that equilibrium conditions have been achieved. This approach allowed the evaluation of all the relevant quantities proper to a plasma discharge, namely: (i) electric and magnetic fields, (ii) plasma density, (iii) deposited power, (iv) electron temperature, and (v) neutral density. Results from simulations at different RF power inputs (250 W, 500 W, 750 W) have been found in agreement with experimental observations, where power deposition and electron temperature increase at the edge of the discharge, while neutral gas is depleted at the center as much as the plasma density is peaked. This is a remarkable result that allows the use of WAVEQM tool for the evaluation of equilibrium conditions in magnetized plasma systems like helicon plasma sources for industrial or space applications. Starting from the actual equilibrium conditions identified by WAVEQM, it is possible to evaluate the actual power deposition; this is a key factor both in a space plasma thruster, where the deposited power is related to the propulsive figures of merit (i.e. specific impulse, and thrust efficiency), and in plasma antennas, where the deposited power is related to the plasma conductivity and in turn to the radiation patterns.
Satisfaction of converge criteria is fulfilled in less than < 10 iterations for the typical plasma parameters in helicon discharges; therefore, numerical strategy to increase the convergence speed are not necessary, making WAVEQM an efficient numerical tool for preliminary design and optimization. Not to mention that since WAVEQM recovers profiles of all the relevant quantities proper to an actual plasma discharge, it can be fruitfully employed as a valuable investigation tool for the analysis of coupled electromagnetic/fluid phenomena in

magnetized plasma sources.
In PARTYWAVE, SPIREs solver has been coupled to a 3D PIC code called PART by means of an hybrid time-frequency loop; in particular, SPIREs solves for electromagnetic fields in vacuum, which are then used by PART to move charged particles in a uniform and structured cylindrical mesh and in time. The time history of plasma current density at each node of the mesh is Fourier transformed to provide plasma response ($\boldsymbol{J_p}$) in SPIRE spectral domain and as a function of the radial coordinate. The method solves for full wave fields and plasma current density by means of an iterative approach assuring convergence of plasma current density components at each radial node through a multidimensional Broyden scheme.
PART features: (i) a AW-CIC model to deposit charge and current density on the mesh, (ii) a radial Poisson solver, and (iii) a syncopated-leapfrog advancing scheme [58]. Numerical accuracy of PART has been verified separately from PARTYWAVE in the initial particle loading in space and velocity, in the charge and current weighting scheme, and in the electrostatic fields compared against analytical solutions for imposed charged density profiles. The Fourier transformation of the plasma current density has been validated against a reference test case with a percent error less than $< 5\%$ (see Fig. 4.8). As a matter of fact, the reference solution has been provided in the cold plasma limit, where the plasma has been modeled by means of a dielectric medium [46]; making PART to work in the same conditions, we calculated the same currents by moving numerical particles in an electromagnetic field, and then Fourier transforming their time response. This is a remarkable result indeed.
Then PART and SPIREs have been coupled, the problem has been stated as a nonlinear system (see Eq. 4.19), and it has been solved iteratively by means of a $3\mathcal{N}$-dimensional Broyden scheme on plasma current density components ($J_{pr}, J_{p\theta}, J_{pz}$) for each of the $\mathcal{N}$ radial nodes shared by SPIREs and PART.
PARTYWAVE has proved to converge linearly (see Figs. 4.11(d) and 4.12(d)). It has been validated against a full wave solution provided by SPIREs, where a good agreement has been found both for electromagnetic fields and for plasma current density radial profiles, with a percent error less than $< 7\%$ (see Fig. 4.14). Results have been provided for 30 radial nodes.
These results proved that PARTYWAVE can evaluate full wave fields considering the actual plasma kinetic response, unlike in the standalone SPIREs code where plasma has been modeled in a simplified way as a dielectric medium. This newly developed code is now ready to simulate wave propagation in an actual plasma made of charged particles, where finite gyroradius effects, finite temperature effects, along with non-Maxwellian particle distributions can be readily taken into account; however, the implementation of particle collisions is necessary to calculate the power deposition, and it can be considered for a future work. For the first time, plasma kinetic response can be simulated in a detailed way with a hybrid time-frequency domain scheme, unlike a full time simulation as the one employed in common electromagnetic PIC code [54]. In this way, PARTYWAVE can be considered an innovative numerical tool.
The scalability of the method has been assessed for an increasing number of radial nodes ranging from 20 to 200 nodes, pointing out that (i) iterations at convergence increase as the number of radial nodes (see Fig. 4.13), and (ii) PARTYWAVE becomes computationally

inefficient when more than $> 10^3$ nodes are necessary to sample the electromagnetic wavelengths involved in the simulation. These numerical issues can be overcome (i) by employing a convergence scheme assuring a superlinear convergence, and (ii) by the use of two staggered radial grids, specifically, a finer one for SPIREs that allows the correct sampling of the wavelengths involved in the electromagnetic problem, and a coarser one for PART that allows a reasonable number of computational particles in the simulation wtihout loosing the statistical representability and keeping under control the particle noise. These suggested mitigation strategies are out of the scope, but they have been considered for a future work.

The last tool is a Moment Method code for the evaluation of radiating electromagnetic fields scattered by PEC antennas in free space. In this code, the antenna surface has been meshed with triangular patches, where RWG basis functions have been introduced to represent the surface antenna currents. The antenna problem has been formulated in terms of a BVP by relating the surface currents to the total electric fields [66], and then it has been converted into a linear system by means of the Galerkin MoM method. The evaluation of matrix elements required the calculation of integrals, which can exhibit integrable singularity; all singularities have been extracted and evaluated in closed form, while numerical integration has been applied only for regular functions.

The code has been validated against analytical expressions for the current distribution over a dipole, and for the self inductance of a small loop. A mesh sensitivity analysis has been performed for the Nagoya Type III antenna, in the range of frequency from 1.0 MHz to 30.0 MHz (of particular interest for helicon plasma sources). Two different meshes have been taken into account, one finer (806 RWGs) than the other (1400 RWGs), and both of them correctly represent the current distribution (see Figs. 5.16 and 5.17) and electrical parameters (see Fig. 5.15). However, the finer mesh is helpful in the determination of current distribution details in narrow region of the antenna. A lower number of RWGs than < 806 results in a inaccurate representation of the current distribution, while an higher number (> 2000) of RWGs generates numerical instabilities related to the growth of matrix condition number, and destroys the accuracy.

This newly developed code is a standalone tool for the preliminary study and design of PEC antennas, and for the optimization of state-of-the-art communication antennas.

On the other hand, it can be considered as a part for the treatment of the general problem concerning the interaction of electromagnetic waves with anisotropic bodies (e.g. plasmas). When the other matrix blocks dealing with the scattering of the volume currents, and its coupling with the surface PEC antenna current will be ready, the full code will be able to simulate into detail both the plasma an the antenna, and how they reciprocally influence themselves from and electromagnetic point of view. This future step represent the innovative contribution of the described Moment Method approach, and it could lead to two main outcomes, such as: (i) an optimization of the RF antenna in ionizing and heating the plasma inside different kind of sources (for a space thruster or a cummunication plasma antennas) beacuse in the other codes (e.g. SPIREs, WAVEQM, and PARTYWAVE) the antenna has been considered as a current distribution given a priori, (ii) a detailed study and analysis of electromagnetic signal propagation in plasmas. Additionally, we expect the former outcome to be exploited in different scientific areas like RF heating in fusion Tokamaks, and industrial plasma sources, where the electromagnetic power deposition by

means of antennas is of key concern, while we expect the latter to provide valuable insights for plasma communication antennas and signal propagation for communication in general. Finally, recall that the numerical tools developed in this research work are capable of providing informations related to: (i) the electromagnetic propagation and power deposition phenomena in a magnetized plasma, (ii) the antenna-plasma coupling mechanism, (iii) the current distribution over an arbitrarely-shaped PEC antenna radiating in free space, (iv) a detailed plasma response, considering it either as a dielectric or a charged-species fluid or an ensemble of charged particles. They are computationally efficient to be used as tool for preliminary design, and optimization of plasma sources, PEC and plasma antennas. Most notably, in these codes the antenna and the plasma problems have been treated in such a detailed way that these numerical tools can play a fundamental role in the understanding of physical processes occuring in electromagnetic propagation in the presence of a plasma, and they can pave the way for the optimization of electric propulsion and enhanced communication systems.

Bibliography

[1] E. Ahedo, "Plasmas for space propulsion," *Plasma Phys. Control. Fusion*, vol. 53, p. 124037, 2011.

[2] M. Martinez-Sanchez and J. Pollard, "Spacecraft electric propulsion—an overview," *J. Propuls. Power*, vol. 14, p. 688, 1998.

[3] F. C. Diaz, "The VASIMR rocket," *Scientific American*, vol. 283, pp. 90–97, 2000.

[4] A. Arefiev and B. Breizman, "Theoretical components of the VASIMR plasma propulsion concept," *Phys. Plasmas*, vol. 11, p. 2942, 2004.

[5] D. Pavarin, F. Ferri, M. Manente, D. Rondini, D. Curreli, Y. Guclu, D. Melazzi, and et al., "Helicon plasma hydrazine . combined micro project overview and development status," in *Proceedings of Space Propulsion Conference*, San Sebastian, Spain, 2010.

[6] D. Pavarin, F. Ferri, M. Manente, D. Curreli, D. Melazzi, and et al., "Development of plasma codes for the design of mini-helicon thrusters," in *Proceedings of the 32th International Electric Propulsion Conference*, Wiesbaden, Germany, 2011.

[7] ——, "Plasma codes for the design and simulation of advanced plasma sources," in *Proceedings of XX Congresso Nazionale AIV*, Padova, Italy, 2011.

[8] R. W. Boswell, "Plasma production using a standing helicon wave," *Physics Letters*, vol. 33A, no. 7, pp. 457–458, 1970.

[9] ——, "Very efficient plasma generation by whistler waves near the lower hybrid frequency," *Plasma Physics Controlled Fusion*, vol. 26, no. 10, pp. 1147–1162, 1984.

[10] A. Komori, T. Shoii., K. Mivamoto, J. Kawai, and K. Kawai, "Helicon waves and efficient plasma production," *Physics Fluids B*, vol. 3, no. 1, pp. 893–898, 1991.

[11] F. F. Chen, "Plasma ionization by helicon waves," *Plasma Physics Controlled Fusion*, vol. 33, no. 11, pp. 339–364, 1991.

[12] R. M. Winglee, J. Slough, T. Ziemba, and A. Goodson, "Mini-magnetospheric plasma propulsion: Tapping the energy of the solar wind for spacecraft propulsion," *Journal of Geophysical Research*, vol. 105, no. A9, pp. 21 067–21 077, September 2000.

[13] J. P. Klozenberg, B. McNamara, and P. C. Thonemann, "The dispersion and attenuation of helicon waves in a uniform cylindrical plasma," *J. Fluid Mech.*, vol. 21, no. 3, pp. 545–563, 1965.

[14] R. W. Boswell, "Effect of boundary conditions on radial mode structure of whistlers," *Journal of Plasma Physics*, vol. 31, pp. 197–208, April 1984.

[15] B. Fischer, M. Kramer, and T. Enk, "Helicon wave coupling to a finite plasma column," *Plasma Physics Controlled Fusion*, vol. 36, pp. 2003–2020, 1994.

[16] I. V. Kamenski and G. G. Borg, "A 1d cylindrical kinetic wave code for helicon plasma sources," *Computer Physics Communication*, no. 113, pp. 10–32, 1998.

[17] B. Davies and P. J. Christiansen, "Helicon waves in a gaseous plasma," *Physics of Plasmas*, vol. 11, no. 12, p. 987, 1969.

[18] F. F. Chen, M. J. Hsieh, and M. Light, "Helicon waves in a nonuniform plasma," *Plasma Source Science and Technology*, vol. 3, no. 49, 1994.

[19] M. Kramer, "Propagation and damping of m=+1 and m=-1 helicon modes in an inhomogeneous plasma column," *Physics of Plasmas*, vol. 6, no. 4, pp. 1052–1058, April 1999.

[20] Y. Mouzouris and J. E. Scharer, "Modeling of profile effects for inductive helicon plasma sources," *IEEE Transactions on Plasma Science*, vol. 24, no. 1, pp. 152–160, February 1996.

[21] B. D. McVey, "ICRF antenna coupling theory for a cylindrical stratified plasma," Plasma Fusion Center, MIT, Tech. Rep., July 1984.

[22] S. Cho and J. G. Kwak, "The effects of the density profile on the power absorption and the equilibrium density in helicon plasmas," *Physics of Plasmas*, vol. 4, no. 11, pp. 4167–4172, November 1997.

[23] F. F. Chen, I. D. Sudit, and M. Light, "Downstream physics of the helicon discharge," *Plasma Source Science and Technology*, vol. 5, pp. 173–180, 1996.

[24] F. F. Chen and D. Arnush, "Generalized theory of helicon waves. i. normal modes," *Physics of Plasmas*, vol. 4, no. 9, pp. 3411–3421, September 1997.

[25] D. Arnush and F. F. Chen, "Generalized theory of helicon waves. ii. excitation and absorption," *Physics of Plasmas*, vol. 5, no. 5, pp. 1239–1254, May 1998.

[26] D. Arnush, "The role of Trivelpiece - Gould waves in antenna coupling to helicon waves," *Physics of Plasmas*, vol. 7, no. 7, pp. 3042–3050, July 2000.

[27] K. P. Shamrai and V. B. Taranov, "Resonances and anti-resonances of a plasma column in a helicon plasma source," *Physics Letters A*, vol. 204, pp. 139–145, August 1995.

[28] ——, "Volume and surface rf power absorption in a helicon plasma source," *Plasma Source Science and Technology*, vol. 5, pp. 474–491, 1996.

[29] K. P. Shamrai, V. B. Taranov, and V. P. Pavlenko, "Excitation, conversion and damping of waves in a helicon plasma source driven by an m=0 antenna," *Plasma Physics Controlled Fusion*, vol. 39, pp. 505–529, 1997.

[30] B. Breizman and A. Arefiev, "Radially localized helicon modes in nonuniform plasma," *Phys. Rev. Lett.*, vol. 84, p. 3863, 2000.

[31] G. Chen, A. Arefiev, R. Bengtson, B. Breizman, C. Lee, and et al., "Resonant power absorption in helicon plasma sources," *Phys. Plasmas*, vol. 13, p. 123507, 2006.

[32] C. Lee, G. Chen, A. Arefiev, R. Bengtson, and B. Breizman, "Measurements and modeling of radio frequency field structures in a helicon plasma," *Phys. Plasmas*, vol. 18, p. 013501, 2011.

[33] A. Arefiev and B. Breizman, "Propagation of radially localized helicon waves in longitudinally nonuniform plasmas," *Phys. Plasmas*, vol. 13, p. 062107, 2006.

[34] M. Panecsky and R. Bengtson, "Characterization of the resonant electromagnetic mode in helicon discharges," *Phys. Plasmas*, vol. 11, p. 4196, 2004.

[35] T. Anderson, *Plasma Antennas*. Artech House, Boston London, 2011.

[36] M. Moisan, A. Schivarova, and W. Trivelpiece, *Phys. Plasmas*, vol. 20, p. 1331, 1982.

[37] T. Dwyer, J. R. Greig, D. Murphy, J. Perin, R. Pechecek, and M. Raleigh, *IEEE Trans. Antenna Propagat.*, vol. AP-32, p. 141, 1984.

[38] W. Kang, M. Rader, and I. Alexeff, in *23rd IEEE International Conference on Plasma Science*, no. 4IP07, Boston, MA, June 1996.

[39] G. Borg, J. Harris, D. Miljak, and N. Martin, "Application of plasma columns to radiofrequency antennas," *Appl. Phys. Lett.*, vol. 74, p. 3272, 1999.

[40] G. Borg, J. Harris, N. Martin, , D. Thorncraft, R. Milliken, D. Miljak, B. Kwan, T. Ng, and J. Kircher, "Plasma as antennas: Theory, experiment and applications," *Phys. Plasmas*, vol. 7, no. 5, p. 2198, 2000.

[41] M. Moisan and Z. Zakrzewski, "Plasma sources based on the propagation of electromagnetic surface waves," *J. Phys. D, Appl. Phys.*, vol. 24, pp. 1025–1048, 1991.

[42] M. Lieberman and A. Lichtenberg, *Pronciples of Plasma Discharges and Material Processing*. New York, J.Wiley, 1994.

[43] J. Rayner, A. Whichello, and A. Cheetham, "Physical characteristics of plasma antennas," *IEEE Transactions on Plasma Science*, vol. 32, no. 1, p. 269, 2004.

[44] P. Russo, G. Cerri, and E. Vecchioni, "Self-consistent analysis of cylindrical plasma antennas," *IEEE Trans. Antennas and Propagation*, vol. 59, no. 5, p. 1503, May 2011.

[45] J. D. Jackson, *Classical Electrodynamics*. John Wileyt and Sons, Inc., 1999.

[46] T. H. Stix, *Plasma Waves.* Springer-Verlag, NewYork, Inc., 1992.

[47] B. D. Fried and S. D. Conte, *The Plasma Dispersion Function.* New York: Academic, 1961.

[48] A. Taflove and S. C. Hagness, *Computational Electrodynamics: the finite-difference time-domain method*, third edition ed. ARTECH HOUSE, INC., 2005.

[49] *MUltifrontal Massively Parallel Solver (MUMPS Version 4.7) User's Guide*, 12 Apr. 2007, information on how to obtain updated copies of MUMPS can be obtained from the Web pages http://www.enseeiht.fro/apo/MUMPS/ and http://graal.ens-lyon.fr/MUMPS/ or by sending email to mumps@cerfacs.fr.

[50] M. Abramovitz and I. A. Stegun, *Handbook of Mathematical Functions.* New York: Dover Publications, Inc., 1972.

[51] D. Curreli and F. Chen, "Equilibrium theory of cylindrical discharges with special application to helicons," *Physics of Plasmas*, vol. 18, 2011.

[52] A. Simon, "Ambipolar diffusion in a magnetic field," *Phys. Rev.*, vol. 98, no. 2, pp. 317–318, 1955.

[53] T. Lafleur and R. Boswell, "Particle-in-cell simulations of ambipolar and nonambipolar diffusion in magnetized plasmas," *Physics of Plasmas*, vol. 19, 2012.

[54] C. K. Birdsall and A. B. Langdon, *Plasma Physics Via Computer Simulation.* Taylor & Francis, 2005.

[55] T. T. Wong, W. S. Luk, and P. A. Heng, "Sampling with Hammersley and Halton Points," *Journal of Graphics Tools*, vol. 2, no. 2, pp. 9–24, 1997.

[56] B. Vandewoestyne and R. Cools, "Good permutations for deterministic scrambled Halton sequences in terms of L2-discrepancy," *Journal of Computational and Applied Mathematics*, vol. 189, pp. 341–361, 2006.

[57] J. P. Verboncoeur, "Particle simulation of plasmas: review and advances," *Plasma Phys. Control. Fusion*, vol. 47, pp. A231–A260, 2005.

[58] J. Cobb and J. Leboeuf, "A syncopated leap-frog algorithm for orbit consistent plasma simulation of material processing reactors," September 1994, research sponsored by U.S. Department of Energy, under contract DE-AC05-84OR21400.

[59] J. Boris, "Relativistic plasma simulation - optimization of a hybrid code," *Proc. 4th Conf. on Numerical Simulation of Plasmas*, pp. 3–67, 1970.

[60] C. Birdsall and D. Fuss, "Clouds-in-clouds, clouds-in-cells physics for many-body plasma simualtion," *Journal of Computational Physics*, vol. 135, pp. 141–148, 1997.

[61] W. Ruyten, "Density-conserving shape factors for particle simulation in cylindrical and sperical coordinates," *Journal of Computational Physics*, vol. 105, 1993.

[62] D. Larson, D. Hewett, and A. Langdon, "Correction factors for PIC simulation on radial grids," *Computer Physics Communications*, vol. 90, 1995.

[63] J. Verboncoeur, "Symmetric spline weighting for charge and current density in particle simulation," *Journal of Computational Physics*, vol. 174, pp. 421–427, 2001.

[64] C. Cornet and D. Kwok, "A new algorithm for charge deposition for multiple-grid method for PIC simulations in r-z cylindrical coordinates," *Journal of Computational Physics*, vol. 225, pp. 808–828, 2007.

[65] *Fastest Fourier Transform in the West (FFTW Version 3.2.2) User's Guide*, 19 Jul. 2009, information on how to obtain updated copies of FFTW can be obtained from the Web page http://www.fftw.org/.

[66] A. Peterson, S. Ray, and R. Mittra, *Computational Methods for Electromagnetics*. Oxford University Press, 1998.

[67] J. V. Bladel, *Electromagnetic Fields*. New York McGraw-Hill, 1964.

[68] R. F. Harrington, *Time harmonic Electromagnetic fields*. McGraw-Hill Book Company, 1961.

[69] R. Bancroft, *Understanding Electromagnetic Scattering Using the Moment Method - A Practical Approach*. Artech House, Boston London, 1996.

[70] N. Morita, N. Kumagai, and J. Mautz, *Integral Equation Methods for Electromagnetic*. Artech House, Boston London, 1990.

[71] A. Sankar and T. Tong, "Current computation on complex structures by finite element method," *Electron. Lett.*, vol. 11, no. 20, pp. 481–482, Oct. 1975 1975.

[72] J. Wang, "Numerical analysis of three-dimensional arbitrarily-shaped conducting scatterers by trilateral surface cell modelling," *Radio Sci.*, vol. 13, no. 4, pp. 947–952, Nov.Dec. 1978.

[73] S. Rao, D. Wilton, and A. Glisson, "Electromagnetic scattering by surface of arbitrary shape," *IEEE Trans. Antennas and Propagation*, vol. 30, no. 3, pp. 409–418, May 1982.

[74] D. Wilton, S. Rao, and A. Glisson, "Electromagnetic scattering by arbitrary surfaces," Rome Air Development Center, Tech. Rep. RADC-TR-79-325, Mar. 1980.

[75] A. Glisson, "On the development of numerical techniques for treating arbitrarily-shaped surfaces," Ph.D. dissertation, Univ. Mississippi, 1978.

[76] P. Arcioni, M. Bressan, and L. Perregrini, "On the evaluation of double surface integrals arising in the application of the boundary integral method to 3D problems," *IEEE Trans. Microwave Theory and techniques*, vol. 45, no. 3, pp. 436–439, Marc. 1997.

[77] P. Yla-Oijla and M. Taskinen, "Calculation of CFIE impedance matrix elements with RWG and n x RWG functions," *IEEE Trans. Antennas and Propagation*, vol. 51, no. 8, pp. 1837–1846, Aug. 2003.

[78] S. Silver, *Microwave Antenna Theory and Design.* Peter Peregrinus Ltd., 1984.

[79] E. Rosa, "The self and mutual inductances of linear conductors," *Bulletin of the Bureau of Standards*, vol. 3, 1907.

[80] G. Vecchi, "Loop-star decomposition of basis functions in the discretization of the EFIE," *IEEE Trans. Antenna Propagat.*, vol. 47, no. 2, p. 339, February 1999.

[81] Francis F. Chen, *Introduction to Plasma Physics and Controlled Fusion*, second edition ed. New York: Plenum Press, 1984, vol. 1.

[82] M. Bonnet, *Boundary Integral Equation Methods for Solids and Fluids.* New York, J.Wiley and Sons, 1995.

Appendix A

Representation of Waves

In cold plasmas the plasma-wave interaction can be simplified by making the hypothesis that electromagnetic fields can be considered "weak" (i.e. the wave-particles interaction only causes a perturbation of the particle orbits), so that a linearization of the kinetic equations is justified [46]. These "weak" fields can be considered as waves of small oscillation amplitude; the waveform is generally sinusoidal. Any sinusoidally oscillating quantity $\boldsymbol{w}$, can be represented as:

$$\boldsymbol{w} = \tilde{\boldsymbol{w}}\, e^{i(\boldsymbol{k}\cdot\boldsymbol{r}-\omega t+\delta)} \tag{A.1}$$

where $\tilde{\boldsymbol{w}}$ is a real costant vector defining the amplitude of the wave and δ is the phase. In cartesian coordinates (x, y, z), $\boldsymbol{r}$ is the position vector, and $\boldsymbol{k}$ is the propagation vector:

$$\boldsymbol{k}\cdot\boldsymbol{r} = k_x x + k_y y + k_z z \tag{A.2}$$

By convention, the exponential notation means that the real part of the expression is to be taken as the measurable quantity. It is customary to incorporate the phase information into $\tilde{\boldsymbol{w}}$ by allowing $\tilde{\boldsymbol{w}}$ to be complex. We can write Eq. (A.1) as:

$$\boldsymbol{w} = \tilde{\boldsymbol{w}}\, e^{i\delta}\, e^{i(\boldsymbol{k}\cdot\boldsymbol{r}-\omega t)} = \tilde{\boldsymbol{w}}_{\boldsymbol{c}}\, e^{i(\boldsymbol{k}\cdot\boldsymbol{r}-\omega t)} \tag{A.3}$$

where $\tilde{\boldsymbol{w}}_{\boldsymbol{c}}$ is a complex amplitude. The phase δ can be recovered from $\tilde{\boldsymbol{w}}_{\boldsymbol{c}}$, since $\Re(\tilde{\boldsymbol{w}}_{\boldsymbol{c}}) = \tilde{\boldsymbol{w}}\cos\delta$ and $\Im(\tilde{\boldsymbol{w}}_{\boldsymbol{c}}) = \tilde{\boldsymbol{w}}\sin\delta$, so that

$$\tan\delta = \frac{\Im(\tilde{\boldsymbol{w}}_{\boldsymbol{c}})}{\Re(\tilde{\boldsymbol{w}}_{\boldsymbol{c}})} \tag{A.4}$$

The *phase velocity*, commonly used in plasma physics to identify different branches of plasma wave dispersion relations [81], is defined by

$$v_\phi = \frac{d\boldsymbol{r}}{dt} = \frac{\omega}{|\boldsymbol{k}|\cos\theta} \tag{A.5}$$

and θ is the angle between the propagation vector and the observation direction.

Appendix B

Fourier Representation of Antenna Currents

If the antenna is removed from the current sheet in Fig. 2.1, the plasma and the conducting cylinder surrounding it can be assumed to be uniform in the azimuthal (θ) and axial (z) directions. We can use Fourier transforms in these directions. We assume that the system is sufficiently long, and the k_z spectrum sufficiently dense to use a Fourier integral of the antenna current density $\boldsymbol{J}(r,\theta,z)$ in the z direction, as follows:

$$\boldsymbol{J}(r,m,k_z) = \frac{1}{2\pi}\int_{-\infty}^{+\infty} dz \int_0^{2\pi} \boldsymbol{J}(r,\theta,z)\, e^{-i(m\theta+k_z z)} \tag{B.1}$$

The antenna current density in the physical space has the form $\boldsymbol{J}(r,\theta,z) = \delta(r-r_b)\,\boldsymbol{K}(\theta,z)$ and the Fourier transform of $\boldsymbol{K}(\theta,z)$ is $\boldsymbol{K}(m,k_z)$, with m and k_z the azimuthal and axial wave numbers, respectively. We assume that the electrostatic fields are shielded by the plasma so that

$$\nabla\cdot\boldsymbol{J} = 0 \tag{B.2}$$

and

$$K_z(m,k_z,\omega) = -\frac{m}{r_b k_z} K_\theta(m,k_z,\omega) \tag{B.3}$$

B.1 Antenna spectra

Though the formalism is general, we confine our attention to the antennas in Fig. 2.2. For I_0 amperes the transform of the single loop antenna (Fig. 2.2(a)) is $K_\theta = I_0$ for $m = 0$, and zero otherwise. For helices the transforms are zero for m even, and for m odd they are respectively:

$$K_\theta = -\frac{2}{m\pi} I_0 \sin\left(\frac{k_z L}{2}\right) \tag{B.4}$$

for Nagoya Type III antenna in Fig. 2.2(b),

$$K_\theta = -\frac{2}{\pi} I_0 \frac{k_z L}{2m} \frac{\sin\left(\frac{k_z L}{2} - m\frac{\pi}{2}\right)}{\frac{k_z L}{2} - m\frac{\pi}{2}} \tag{B.5}$$

for the fractional helix antenna in Fig. 2.2(c),

$$K_\theta = 2I_0 \left[\frac{\sin\left(\frac{k_z L}{2} - m\pi\right)}{\frac{k_z L}{2} - m\pi} - \frac{\sin\left(\frac{k_z L}{2}\right)}{m\pi} \right] \tag{B.6}$$

for the integral t-turn helix antenna in Fig. 2.2(d). The antenna length is L.

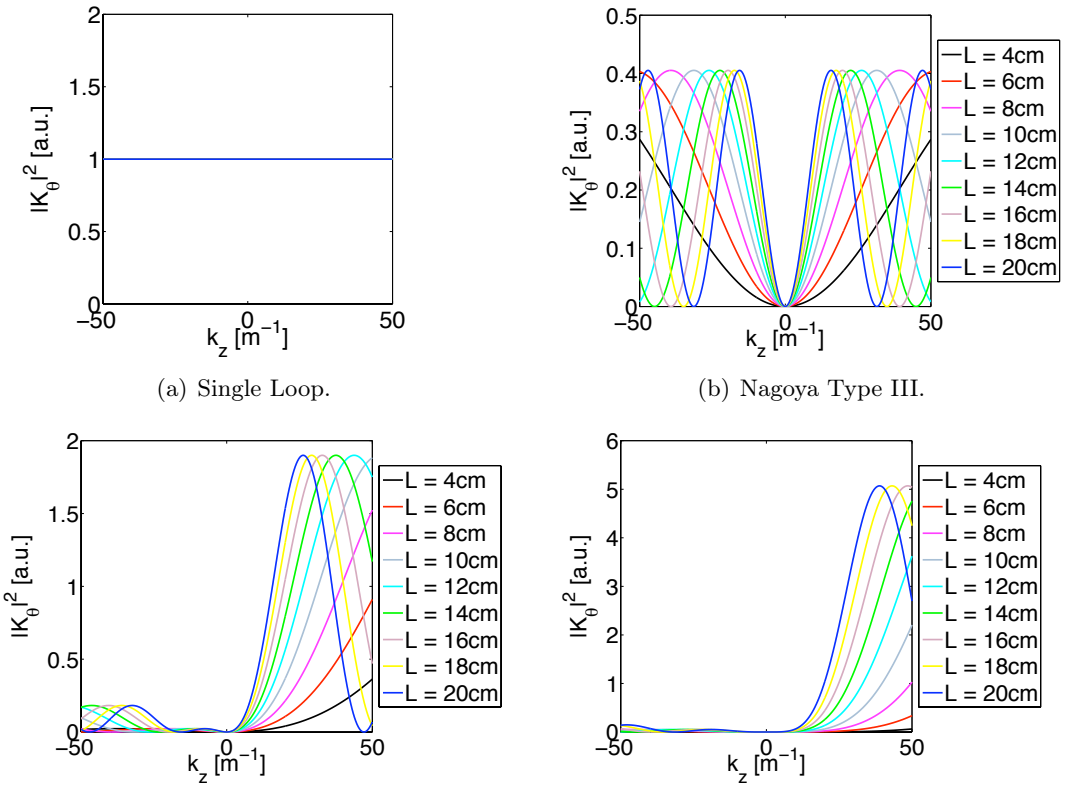

(a) Single Loop.

(b) Nagoya Type III.

(c) Fractional helix.

(d) Integral 1-turn helix.

Figure B.1: Power spectrum (arbitrary units) for the most common antennas used in helicon plasma sources.

B.2 Fourier transform of a Single Loop antenna

When a particular antenna is considered, its current distribution in the physical space is expressed in terms of delta and heaviside functions; the Dirac delta function is used to radially constrain the flow of the current, while the heaviside function is used to take into account an axial finite width.

The spatial representation of current density can be quite involved for some antennas so that the analytical evaluation of its Fourier transform can become cumbersome. In order to give an example on how to express the spatial representation, and how to compute its Furier transform, we consider the single loop antenna showed in Fig. 2.2(a). First consider the filamentary single loop antenna with radius $r = b$ and placed at $z = 0$ showed in Fig. B.2, for I amperes. The antenna is infinitesimally thin both in radial and axial directions, and

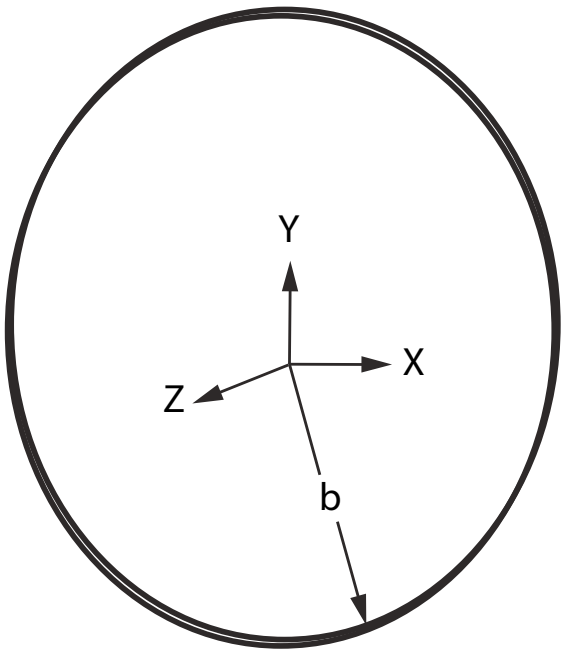

Figure B.2: Filamentary single loop antenna.

the spatial representation of the current flowing in the antenna is given by

$$\boldsymbol{J}(r,\theta,z) = I\delta(r-b)\,\delta(z) \tag{B.7}$$

Substituting Eq. B.7 in Eq. B.1, we have

$$\boldsymbol{J}(r,m,k_z) = \frac{I}{2\pi}\delta(r-b)\int_{-\infty}^{+\infty}\delta(z)\,e^{-ik_z z}dz\int_0^{2\pi}e^{-im\theta}d\theta = \frac{I}{2\pi}\delta(r-b)\int_0^{2\pi}e^{-im\theta}d\theta \tag{B.8}$$

Depending on the integer number used for the azimuthal mode number m, the integral assumes different values. We have for $m = 0$

$$\boldsymbol{J}(r,m,k_z) = \frac{I}{2\pi}\delta(r-b)\int_0^{2\pi}d\theta = I\delta(r-b) \tag{B.9}$$

whereas for $m \neq 0$ we have

$$\boldsymbol{J}(r,m,k_z) = \frac{I}{2\pi}\delta(r-b)\int_0^{2\pi}e^{-im\theta}d\theta = 0 \tag{B.10}$$

which is the reason why a single loop antenna is capable of exciting just one azimuthal mode number $m = 0$. Consider now a single loop antenna which is infinitesimally thin just along the radial direction, and having a width w along the axial direction, as the one pictured in Fig. B.3. In order to represent the spatial extent of the current distribution for

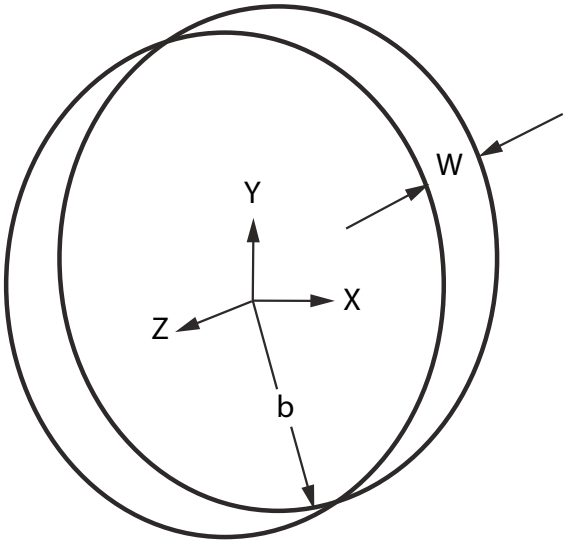

Figure B.3: Finite width single loop antenna.

the finite width antenna, it is convenient to define the following notation for the heaviside function

$$u_z\left(\pm\frac{w}{2}\right) = \begin{cases} 1 & \text{for } -\frac{w}{2} \leq z \leq +\frac{w}{2} \\ 0 & \text{otherwise} \end{cases} \tag{B.11}$$

The current representation now reads

$$\boldsymbol{J}\left(r,\theta,z\right) = \frac{I}{w}\delta\left(r-b\right)u_z\left(\pm\frac{w}{2}\right) \tag{B.12}$$

Substituting Eq. B.12 in Eq. B.1, we have

$$\begin{aligned} \boldsymbol{J}\left(r,m,k_z\right) &= \frac{I}{2\pi w}\delta\left(r-b\right)\int_{-\infty}^{+\infty} u_z\left(\pm\frac{w}{2}\right)e^{-ik_z z}dz\int_0^{2\pi} e^{-im\theta}d\theta \\ &= \frac{I}{2\pi w}\delta\left(r-b\right)\int_{-\frac{w}{2}}^{+\frac{w}{2}} e^{-ik_z z}dz\int_0^{2\pi} e^{-im\theta}d\theta \\ &= \frac{I}{2\pi}\frac{\delta\left(r-b\right)}{\left(\frac{k_z w}{2}\right)}\sin\left(\frac{k_z w}{2}\right)\int_0^{2\pi} e^{-im\theta}d\theta \end{aligned} \tag{B.13}$$

As said above, the only azimuthal wave number allowed by the single loop antenna is $m = 0$ so the Fourier trasformed current for a finite width single loop antenna is

$$\boldsymbol{J}\left(r,m,k_z\right) = I\frac{\delta\left(r-b\right)}{\frac{k_z w}{2}}\sin\left(\frac{k_z w}{2}\right) \tag{B.14}$$

Appendix C

The Rao-Wilton-Glisson basis function

Recall the expression of the nth RWG basis function

$$\boldsymbol{f}_n(\boldsymbol{r}) = \begin{cases} \frac{l_n}{2A_n^+}\boldsymbol{\rho}_n^+ & , \boldsymbol{r} \in T_n^+ \\ \\ \frac{l_n}{2A_n^-}\boldsymbol{\rho}_n^- & , \boldsymbol{r} \in T_n^- \end{cases} \tag{C.1}$$

defined on two adjoining triangles T_n^+ and T_n^- connected through the nth common edge as pictured in Fig. C.1(a). Each point on the RWG function can be designated either by the position vectors $\boldsymbol{r}_n^\pm$ with respect to the global origin O, or with the position vectors $\boldsymbol{\rho}_n^\pm$ in $T_n^\pm$ with respect to triangular vertices $O_n^\pm$. Note that $A_n^\pm$ is the area of triangle $T_n^\pm$, and l_n is the length of the common edge. The basis function $\boldsymbol{f}_n$ is used to approximately

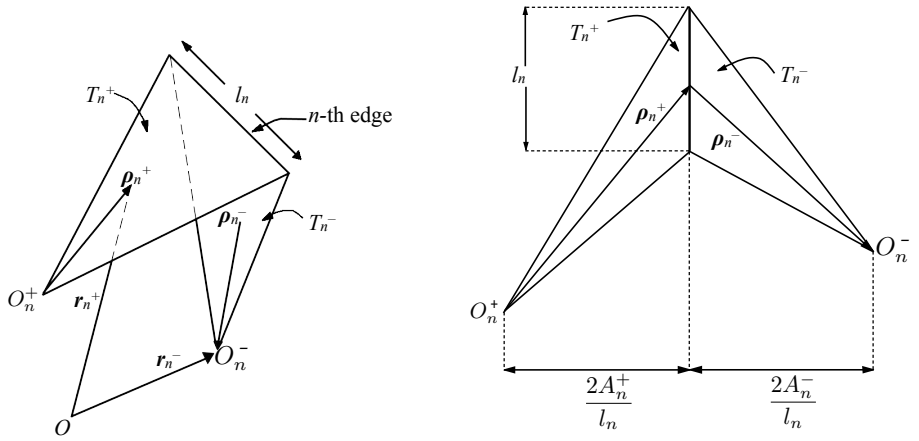

(a) Triangle pair and geometrical parameters associated with interior edge.

(b) Geometry for construction of component of basis function normal to the edge.

Figure C.1: Geometrical parameters associated with the nth RWG basis function.

represent the surface current, and we list below some properties:

1. The normal component of the current is continuous across the common edge, and the currents have no component normal to the boundary of the surface formed by $T_n^+ \cup T_n^-$. Consequently, no line charges are present along the common (interior) edge and along the outer boundary of the RWG function. Moreover the surface divergence in $T_n^\pm$ of $\boldsymbol{f}_n$, which is proportional to the surface charge density associated with the triangular patch, is

$$\nabla_S \cdot \boldsymbol{f}_n(\boldsymbol{r}) = \begin{cases} \frac{l_n}{A_n^+} & , \boldsymbol{r} \in T_n^+ \\ -\frac{l_n}{A_n^-} & , \boldsymbol{r} \in T_n^- \\ 0 & , \text{otherwise} \end{cases} \tag{C.2}$$

   We can conclude that the surface charge density is constant within a single triangle, and the total charge associated with the triangle pair $T_n^\pm$ is zero.

2. The normal component on the boundary of $T_n^+ \cup T_n^-$ is zero.

3. With reference to Fig. C.2, the moment of $\boldsymbol{f}_n(\boldsymbol{r})$ is

$$\left(A_n^+ + A_n^+\right) \boldsymbol{f}_n^{avg}(\boldsymbol{r}) \equiv \int_{T_n^+ \cup T_n^-} \boldsymbol{f}_n(\boldsymbol{r})\, dS = \frac{l_n}{2}\left(\boldsymbol{\rho}_n^{c+} + \boldsymbol{\rho}_n^{c-}\right) = l_n\left(\boldsymbol{r}_n^{c+} + \boldsymbol{r}_n^{c-}\right) \tag{C.3}$$

   where $\boldsymbol{\rho}_n^{c\pm}$ is the vector between the free vertex and the centroid of $T_n^\pm$, with $\boldsymbol{\rho}_n^{c+}$ directed toward and $\boldsymbol{\rho}_n^{c-}$ directed away from the common edge l_n. The vector from the global origin O to the centroid of $T_n^\pm$ is represented by $\boldsymbol{r}_n^{c\pm}$.

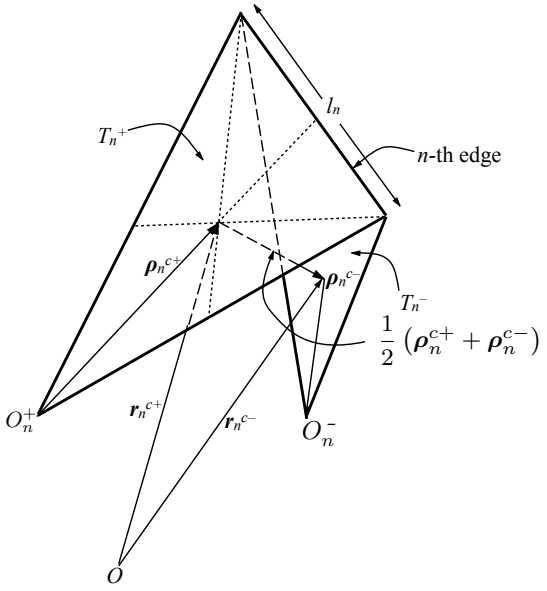

Figure C.2: Global and local coordinates.

The current on the antenna surface S may be approximated in terms of the $\boldsymbol{f}_n$ as

$$\boldsymbol{J_A} \cong \sum_{n=1}^{N} I_n \boldsymbol{f}_n (\boldsymbol{r}) \tag{C.4}$$

where N is the number of interior (nonboundary) edges. Since a basis function is associated with each nonboundary edge of the mesh, up to three basis functions may have nonzero values within each triangular patch. Moreover, at a given edge only the basis function associated with that edge has a current component normal to the edge, since all other basis functions in adjacent patches are parallel to the edge.

C.1 Properties

With reference to the second integral appearing on the LHS of Eq. 5.18, we can exploit some properties of RWG basis functions to simplify that expression. Now consider

$$\begin{aligned} &\int_{T_m^+ \cup T_m^-} \boldsymbol{f}_m (\boldsymbol{r}) \cdot \left(\nabla_S \int_{T_n^+ \cup T_n^-} G (\boldsymbol{r} - \boldsymbol{r'}) \left(\nabla_{S'} \cdot \boldsymbol{f}_n (\boldsymbol{r'}) \right) dS' \right) dS = \\ &= \int_{T_m^+ \cup T_m^-} \boldsymbol{f}_m (\boldsymbol{r}) \cdot \left(\nabla_S \tau (\boldsymbol{r}) \right) dS \end{aligned} \tag{C.5}$$

where

$$\tau (\boldsymbol{r}) = \int_{T_n^+ \cup T_n^-} G (\boldsymbol{r} - \boldsymbol{r'}) \left(\nabla_{S'} \cdot \boldsymbol{f}_n (\boldsymbol{r'}) \right) dS' \tag{C.6}$$

With the aid of vector identity, we have

$$\begin{aligned} &\int_{T_m^+ \cup T_m^-} \boldsymbol{f}_m (\boldsymbol{r}) \cdot \left(\nabla_S \tau (\boldsymbol{r}) \right) dS = \int_{T_m^+ \cup T_m^-} \nabla_S \cdot \left(\tau (\boldsymbol{r}) \boldsymbol{f}_m (\boldsymbol{r}) \right) dS + \\ &- \int_{T_m^+ \cup T_m^-} \tau (\boldsymbol{r}) \nabla_S \cdot \boldsymbol{f}_m (\boldsymbol{r}) \, dS \end{aligned} \tag{C.7}$$

Applying Gauss' theorem, and recalling that the RWG function has no component normal to the contour, we have

$$\int_{T_m^+ \cup T_m^-} \nabla_S \cdot \left(\tau (\boldsymbol{r}) \boldsymbol{f}_m (\boldsymbol{r}) \right) dS = \oint_C \left(\tau (\boldsymbol{r}) \boldsymbol{f}_m (\boldsymbol{r}) \right) \cdot \hat{\boldsymbol{n}}_{\boldsymbol{b}} dC = 0 \tag{C.8}$$

where C is the contour around the surface $T_m^+ \cup T_m^-$, and $\hat{\boldsymbol{n}}_{\boldsymbol{b}}$ is the unit vector normal to the contour, pointing outward of the contour iteself. Thus we have

$$\begin{aligned} &\int_{T_m^+ \cup T_m^-} \boldsymbol{f}_m (\boldsymbol{r}) \cdot \left(\nabla_S \int_{T_n^+ \cup T_n^-} G (\boldsymbol{r} - \boldsymbol{r'}) \left(\nabla_{S'} \cdot \boldsymbol{f}_n (\boldsymbol{r'}) \right) dS' \right) dS = \\ &= - \int_{T_m^+ \cup T_m^-} \nabla_S \cdot \boldsymbol{f}_m (\boldsymbol{r}) \int_{T_n^+ \cup T_n^-} G (\boldsymbol{r} - \boldsymbol{r'}) \left(\nabla_{S'} \cdot \boldsymbol{f}_n (\boldsymbol{r'}) \right) dS' dS \end{aligned} \tag{C.9}$$

Appendix D

Integration over Triangular Surfaces

D.1 Normalized area local coordinates

In order to determine the surface integrals, it is convenient to use a local coordinate system for each triangle. Consider now the triangle T_n of area A_n, and divide it into three sub-triangles of areas A_1, A_2 and A_3, respectively, as pictured in Fig. D.1. The normalized

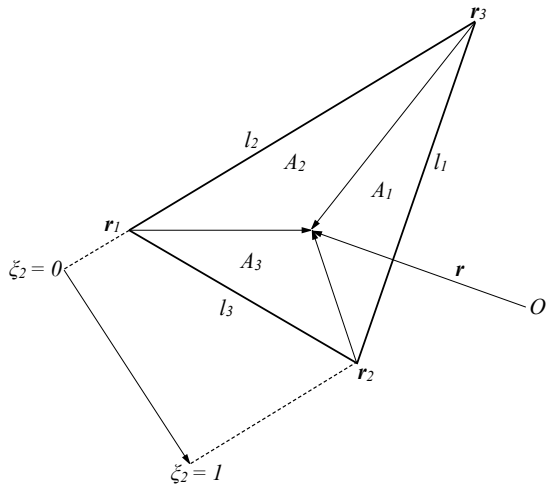

Figure D.1: Definition of normalized area coordinates for triangle T_n.

area coordinates are defined as

$$\xi_1 = \frac{A_1}{A_n}, \quad \xi_2 = \frac{A_2}{A_n}, \quad \xi_3 = \frac{A_3}{A_n} \tag{D.1}$$

where A_1, A_2 and A_3 satisfy the relation

$$A_1 + A_2 + A_3 = A_n \tag{D.2}$$

and $\xi_1 + \xi_2 + \xi_3 = 1$. The position of a point in the considered triangle T_n is given by

$$\boldsymbol{r} = \xi_1 \boldsymbol{r}_1 + \xi_2 \boldsymbol{r}_2 + \xi_3 \boldsymbol{r}_3 = \xi_1 \boldsymbol{r}_1 + \xi_2 \boldsymbol{r}_2 + (1 - \xi_1 - \xi_2)\, \boldsymbol{r}_3 \tag{D.3}$$

In the triangle T_n, all three coordinates vary between zero and one; specifically, at the three corners $\boldsymbol{r}_1$, $\boldsymbol{r}_2$ and $\boldsymbol{r}_3$, the area coordinates take the values, $\xi_1 = (1,0,0)$, $\xi_2 = (0,1,0)$ and $\xi_3 = (0,0,1)$, respectively.
Therefore, the surface integral of a generic function $g(\boldsymbol{r})$ over the triangle T_n becomes

$$\int_{T_n} g(\boldsymbol{r})\, dS = 2A_n \int_{\xi_1=0}^{\xi_1=1} \int_{\xi_2=0}^{\xi_2=1-\xi_1} g\left(\xi_1 \boldsymbol{r}_1 + \xi_2 \boldsymbol{r}_2 + (1-\xi_1-\xi_2)\,\boldsymbol{r}_3\right) d\xi_1 d\xi_2 \tag{D.4}$$

where the factor $2A_n$ is the Jacobian of the coordinate transformation.

D.2 Gaussian quadrature formulas

The integration of a function $g(\xi_1, \xi_2)$ over the triangle is performed numerically using the Gaussian quadrature formula

$$2A_n \int_{\xi_1=0}^{\xi_1=1} \int_{\xi_2=0}^{\xi_2=1-\xi_1} g(\xi_1, \xi_2)\, d\xi_1 d\xi_2 \approx A_n \sum_{n=1}^{N_G} \omega_n g(\xi_{1n}, \xi_{2n}) \tag{D.5}$$

where A_n is the triangle area, N_G is the number of quadrature points, and ω_n is the weighting coefficient. Coordinates of the sample points $(\xi_{1n}, \xi_{2n}, \xi_{3n})$, and the weighting functions ω_n can be found in [82].

D.3 Closed form for the integral over the self patch

With reference to Eqs. 5.29, 5.30, the analytical expression for integrals I_1 and I_2 are

$$I_1 = \frac{1}{4\pi} \int_T \int_{T'} \frac{1}{R} dS' dS \tag{D.6}$$

$$I_2 = \frac{1}{4\pi} \int_T \boldsymbol{\rho}_o \cdot \int_{T'} \boldsymbol{\rho}_s \frac{1}{R} dS' dS \tag{D.7}$$

and they are explicited for coincident triangles, namely $T \equiv T'$ (see Fig. D.2). In this case, the vectors $\boldsymbol{R} = \boldsymbol{r} - \boldsymbol{r'}$, $\boldsymbol{\rho}_o$ and $\boldsymbol{\rho}_s$ lie in the same plane and the following identity holds

$$\frac{1}{R} = -\nabla_S \cdot \nabla_{S'} R \tag{D.8}$$

Applying Stokes' theorem, double surface integrals I_1 and I_2 become double contour integrals. In the case of coincident triangles, they read

$$I_1 = -\frac{1}{3\pi} A^2 \left(\frac{1}{a} \ln\left(1 - \frac{a}{p}\right) + \frac{1}{b} \ln\left(1 - \frac{b}{p}\right) + \frac{1}{c} \ln\left(1 - \frac{c}{p}\right) \right) \tag{D.9}$$

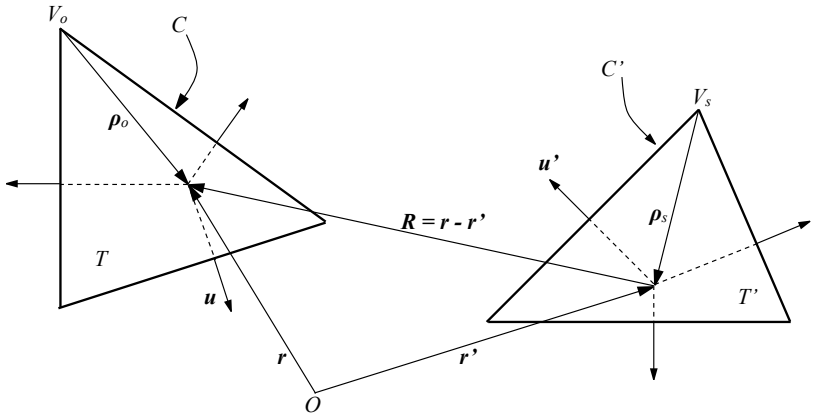

Figure D.2: Geometrical parameters associated with triangle T and T'.

When $V_o = V_s$, and with a the length of the edge opposite to vertex V_o, we have:

$$\begin{aligned} I_2 =& \frac{A^2}{120\pi}\left[\left(10+3\frac{c^2-a^2}{b^2}-3\frac{a^2-b^2}{c^2}\right)a-\left(5-3\frac{a^2-b^2}{c^2}-2\frac{b^2-c^2}{a^2}\right)b\right. \\ & \left(5+3\frac{c^2-a^2}{b^2}+2\frac{b^2-c^2}{a^2}\right)c+\left(a^2-3b^2-3c^2-8\frac{A^2}{a^2}\right)\frac{2}{a}\ln\left(1-\frac{a}{p}\right) \\ & +\left(a^2-2b^2-4c^2+6\frac{A^2}{b^2}\right)\frac{4}{b}\ln\left(1-\frac{b}{p}\right) \\ & \left.+\left(a^2-4b^2-2c^2+6\frac{A^2}{c^2}\right)\frac{4}{c}\ln\left(1-\frac{c}{p}\right)\right] \end{aligned} \tag{D.10}$$

When $V_o \neq V_s$, and with a the length of the edge between vertices V_o and V_s, we have:

$$\begin{aligned} I_2 =& \frac{A^2}{240\pi}\left[\left(-10+\frac{c^2-a^2}{b^2}-\frac{a^2-b^2}{c^2}\right)a+\left(5+\frac{a^2-b^2}{c^2}-6\frac{b^2-c^2}{a^2}\right)b\right. \\ & \left(5-\frac{c^2-a^2}{b^2}+6\frac{b^2-c^2}{a^2}\right)c+\left(2a^2-b^2-c^2-4\frac{A^2}{a^2}\right)\frac{12}{a}\ln\left(1-\frac{a}{p}\right) \\ & +\left(9a^2-3b^2-c^2+4\frac{A^2}{b^2}\right)\frac{2}{b}\ln\left(1-\frac{b}{p}\right) \\ & \left.+\left(9a^2-b^2-3c^2+4\frac{A^2}{c^2}\right)\frac{2}{c}\ln\left(1-\frac{c}{p}\right)\right] \end{aligned} \tag{D.11}$$

In all these expressions T denotes a generic triangular patch, a, b and c denote the lengths of the edges of the considered triangle, A is its area, and $p = (a+b+c)/2$ is the half-perimeter of the triangle.

D.4 Integration over patches sharing an edge or a vertex

When the integration triangles share either an edge or a vertex, the integrals over T' of the singular terms in Eqs. 5.29, 5.30 have a closed form, while the integration over T

can be performed numerically. We report here the formulas proposed in [77] for sake of completeness

$$K_1^{-1} = \int_{T'} \frac{1}{R} dS' \quad , \quad \boldsymbol{K}_2^{-1} = \int_{T'} \boldsymbol{\rho}_s \frac{1}{R} dS' \tag{D.12}$$

$$K_1^{1} = \int_{T'} R dS' \quad , \quad \boldsymbol{K}_2^{1} = \int_{T'} \boldsymbol{\rho}_s R dS' \tag{D.13}$$

With reference to Fig. D.3, we assume that the vertex V_s of the triangle T' is identified by the position vector $\boldsymbol{q}_3$, so that we have:

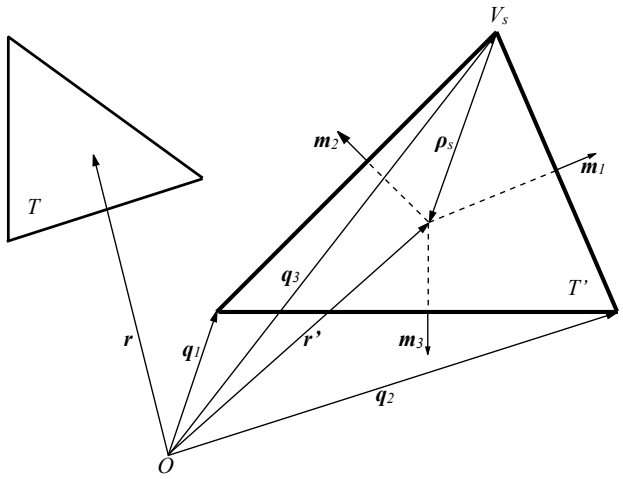

Figure D.3: Notation for analytical formulas.

$$I_i^{-1} = \int_{\partial T'} \frac{1}{R} dl' = \ln\left(\frac{R_i^+ + s_i^+}{R_i^- + s_i^-}\right) \tag{D.14}$$

$$K_i^{-3} = \int_{T'} \frac{1}{R^3} dS' = \begin{cases} 0, & \text{if } \omega_0 = 0 \\ \frac{1}{|\omega_0|} \sum_{i=1}^{3} \beta_i, & \text{otherwise} \end{cases} \tag{D.15}$$

where $\partial T'$, $i = 1, 2, 3$ are the edges of T' and where

$$\beta_i = \arctan\left(\frac{t_i^0 s_i^+}{\left(R_i^0\right)^2 + |\omega_0| R_i^+}\right) - \arctan\left(\frac{t_i^0 s_i^-}{\left(R_i^0\right)^2 + |\omega_0| R_i^-}\right) \tag{D.16}$$

The other variables are defined

$$
\begin{aligned}
&\boldsymbol{u} = \tfrac{\boldsymbol{q}_2-\boldsymbol{q}_1}{l_3} && \omega_0 = (\boldsymbol{r}-\boldsymbol{q}_1)\cdot\hat{\boldsymbol{n}} \\
&\boldsymbol{v} = \hat{\boldsymbol{n}}\times\boldsymbol{u} && v_0 = (\boldsymbol{r}-\boldsymbol{q}_1)\cdot\boldsymbol{v} \\
&u_3 = (\boldsymbol{q}_3-\boldsymbol{q}_1)\cdot\boldsymbol{u} && u_0 = (\boldsymbol{r}-\boldsymbol{q}_1)\cdot\boldsymbol{u} \\
&v_3 = \tfrac{2A}{l_3} && \\
&s_1^- = -\tfrac{(l_3-u_0)(l_3-u_3)+v_0v_3}{l_1} && s_1^+ = s_1^- + l_1 \\
&s_2^- = -\tfrac{u_3(u_3-u_0)+v_3(v_3-v_3)}{l_2} && s_2^+ = s_2^- + l_2 \\
&s_3^- = -u_0 && s_3^+ = s_3^- + l_3 \\
&t_1^0 = \tfrac{v_0(u_3-l_3)+v_3(l_3-u_0)}{l_1} && R_1^+ = R_2^- = |\boldsymbol{r}-\boldsymbol{q}_3| \\
&t_2^0 = \tfrac{u_0v_3-v_0u_3}{l_2} && R_2^+ = R_3^- = |\boldsymbol{r}-\boldsymbol{q}_1| \\
&t_3^0 = v_0 && R_3^+ = R_1^- = |\boldsymbol{r}-\boldsymbol{q}_2| \\
&R_i^0 = \sqrt{\left(t_i^0\right)^2+\omega_0^2} &&
\end{aligned}
\tag{D.17}
$$

Here l_i with $i = 1, 2, 3$ are the lengths of the edges $\partial_i T'$, and $\boldsymbol{q}_i$ with $i = 1, 2, 3$ are the vertices of T', where A is the area of T'.
By using the above notation we can write Eq. D.12 and Eq. D.13 in closed form

$$
K_1^{-1} = \begin{cases} \sum_{i=1}^3 t_i^0 I_i^{-1}\,, & \omega_0 = 0 \\ -\omega_0^2 K_1^{-3} + \sum_{i=1}^3 t_i^0 I_i^{-1}\,, & \omega_0 \neq 0 \end{cases} \tag{D.18}
$$

$$
K_1^{1} = \begin{cases} \frac{1}{3}\sum_{i=1}^3 t_i^0 I_i^{1}\,, & \omega_0 = 0 \\ \frac{1}{3}\left(-\omega_0^2 K_1^{-1} + \sum_{i=1}^3 t_i^0 I_i^{1}\right)\,, & \omega_0 \neq 0 \end{cases} \tag{D.19}
$$

$$
\boldsymbol{K}_2^{-1} = \boldsymbol{I}_m^1 + (\boldsymbol{r}-\boldsymbol{q}_3)\,K_1^{-1} \tag{D.20}
$$

$$
\boldsymbol{K}_2^{1} = \frac{1}{3}\boldsymbol{I}_m^3 + (\boldsymbol{r}-\boldsymbol{q}_3)\,K_1^{1} \tag{D.21}
$$

where

$$
\boldsymbol{I}_m^1 = \boldsymbol{m}_1 I_1^1 + \boldsymbol{m}_2 I_2^1 + \boldsymbol{m}_3 I_1^1 \tag{D.22}
$$

$$
\boldsymbol{I}_m^3 = \boldsymbol{m}_1 I_1^3 + \boldsymbol{m}_2 I_2^3 + \boldsymbol{m}_3 I_1^3 \tag{D.23}
$$

with $\boldsymbol{r}$ the observation point on triangle T, $\hat{\boldsymbol{n}}$ is the unit vector normal to triangle T', and $\boldsymbol{m}_i$ is the outer unit vector of the edge $\partial_i T'$ with $i = 1, 2, 3$. In addition, we need the recursive formulas

$$I_i^1 = \int_{\partial_i T'} R dl' = \frac{1}{2}\left(s_i^+ R_i^+ - s_i^- R_i^- + \left(R_i^0\right)^2 I_i^{-1}\right) \tag{D.24}$$

$$I_i^3 = \int_{\partial_i T'} R^3 dl' = \frac{1}{4}\left(s_i^+ \left(R_i^+\right)^3 - s_i^- \left(R_i^-\right)^3 + 3\left(R_i^0\right)^2 I_i^1\right) \tag{D.25}$$